Blade-Mounted Actuation for Helicopter Rotor Control

by

Matthew Edward Fox

S.B. Massachusetts Institute of Technology (1990)

Submitted to the Department of Aeronautics and Astronautics
in partial fulfillment of the requirements
for the degree of

Master of Science

at the

Massachusetts Institute of Technology

June, 1993

Author ______________________________
Department of Aeronautics and Astronautics
February 26, 1993

Certified by ______________________________
Professor Steven R. Hall
Department of Aeronautics and Astronautics
Thesis Supervisor

Accepted by ______________________________
Professor Harold Y. Wachman
Chairman, Department Graduate Committee

Blade-Mounted Actuation for Helicopter Rotor Control

by

Matthew Edward Fox

Submitted to the Department of Aeronautics and Astronautics
on February 26, 1993, in partial fulfillment of the
requirements for the degree of
Master of Science

Abstract

The feasibility of using blade-mounted actuators for helicopter rotor control is investigated. A state space model of a helicopter rotor is developed by making several simplifying assumptions that yield time-invariant dynamics. This is convenient for control design, because transfer functions from control inputs to hub loads may be obtained. The transfer functions allow conventional and blade-mounted actuation methods to be compared for steady and multicyclic inputs. Furthermore, the model relates blade lift and pitch to control inputs by general aerodynamic coefficients, so that any blade-mounted actuator may be incorporated into the model.

The rotor model is semi-articulated with rigid blade flapping, but it is derived so that flapwise bending can be included, if desired. The model incorporates elastic blade torsion as well as rigid blade pitch, so that both controllable twist and full blade feathering can be investigated. Simple linear aerodynamics are assumed with a dynamic inflow model that can be used for both hover and forward flight.

Piezoelectric servoflap actuation is investigated for the H-34 research rotor, with emphasis on higher harmonic vibration control. The servoflap is capable of suppressing higher harmonic vibrations, and can be used to augment full blade feathering for collective and cyclic control. The servoflap is able to provide 0.25 g of higher harmonic vibration control with deflections on the order of ±5 deg. Piezoelectric actuation is potentially feasible within this range.

Acknowledgments

This research was funded by Boeing Helicopters under Contract Nos. ABQ024 and ACP853, with Mr. Jim Keller serving as technical monitor. We appreciate the assistance of Mr. Keller who provided the wind tunnel data used in this research, and Mr. Rich Teal, also of Boeing Helicopters, who provided technical consultation. We would also like to thank Mr. Frank Tarzanin and Ms. Joyce Peranteau of Boeing Helicopters for supporting the C-60 program used in this research. Finally, we would like to thank Mr. James Garcia of M.I.T. for providing the C-60 data that is presented in this report.

Contents

List of Figures

List of Tables

Notation

An attempt was made to use notation as consistent as possible with that of Johnson [34]. Dimensionless quantities are normalized by the rotor radius R, the rotation rate Ω, and/or the air density ρ, where possible.

a	blade section lift-curve slope c_{l_α}
A	rotor area, πR^2; state matrix
A^n	rotor integral, see Appendix A
B	state control matrix
B^n	rotor integral, see Appendix A
c	blade chord; elastic matrix
c_d	section drag coefficient, $D/\frac{1}{2}\rho U^2(\Omega R)^2 c$
c_l	section lift coefficient, $L/\frac{1}{2}\rho U^2(\Omega R)^2 c$
c_{l_α}	section lift coefficient per angle of attack
c_{l_η}	section lift coefficient per servoflap deflection
c_m	section pitch moment coefficient, $N/\frac{1}{2}\rho U^2(\Omega R)^2 c^2$
c_{m_η}	section pitch moment per servoflap deflection
C	output matrix
C_L	roll moment coefficient, $M_x/\rho A R(\Omega R)^2$
C_M	pitch moment coefficient, $M_y/\rho A R(\Omega R)^2$
C_T	thrust coefficient, $T/\rho A(\Omega R)^2$
C_T/σ	blade loading
C_k^n	rotor integral, see Appendix A
d	disturbance; piezoelectric coupling matrix; length of moment arm for piezo-servoflap
d_{15}	shear piezoelectric coupling coefficient
d_{31}	transverse piezoelectric coupling coefficient
d_{33}	longitudinal piezoelectric coupling coefficient
D	electrical displacement tensor; section aerodynamic drag; output control matrix
D^n	rotor integral, see Appendix A
e	flap hinge offset
E	electric field tensor
$E\{\cdot\}$	expected value
E_c	coercive field

E^n	rotor integral, see Appendix A
f	frequency [Hz]
F_r	section radial aerodynamic force
F_x	section aerodynamic force parallel to disk plane
F_z	section aerodynamic force normal to disk plane
F^n	rotor integral, see Appendix A
$g_{\max}$	maximum vibration level
G	blade shear modulus; feedback gain matrix
$G(s)$	plant transfer function
GJ	torsional stiffness
G_k^n	rotor integral, see Appendix A
H	rotor drag force, positive rearward
$H(s)$	compensator transfer function
H_k^n	rotor integral, see Appendix A
I_{b}	characteristic inertia of the rotor blade, $\int_e^R mr^2dr$
I_z	blade rotational inertia
I_β	blade moment of inertia about the flapping hinge, $\int_e^R m\xi_\beta^2(r)dr$
I_β^*	normalized flapping inertia, I_β/I_{b}
I_θ	sectional pitch inertia of blade
I_{θ_k}	pitch inertia of kth torsion mode
$I_{\theta_k}^*$	normalized pitch inertia of kth torsion mode, $I_{\theta_k}/I_{\mathrm{b}}$
j	imaginary number, $\sqrt{-1}$
J	geometric moment of inertia; cost functional
J^*	optimal cost
J^n	rotor integral, see Appendix A
K_β	flapping hinge spring constant
K_{θ_k}	generalized stiffness of kth torsion mode
K^n	rotor integral, see Appendix A
L	section aerodynamic lift; Lagrangian
L^n	rotor integral, see Appendix A
m	blade sectional mass
M_{F}	flapping moment of blade, positive upward
M_x	rotor hub roll moment, positive toward retreating blade
M_y	rotor hub pitch moment, positive rearward

M_k^n	rotor integral, see Appendix A
n	discrete time index; lift coefficient of servoflap c_{l_η}
$\overline{n}$	normalized lift coefficient of servoflap, c_{l_η}/a
N	number of blades
N	blade torsion
N_{aero}	blade torsion due to aerodynamics
N_k	blade torsion of the kth mode
p	moment coefficient of servoflap, c_{m_η}
$\overline{p}$	normalized moment coefficient of servoflap, c_{m_η}/a
$\uparrow P$	poling direction
q	blade index
Q	state weighting matrix
r	rotor disk radial coordinate
$\overline{r}$	normalized radial coordinate, r/R
r_1	inboard servoflap location
r_2	outboard servoflap location
R	rotor radius; control weighting matrix
s	Laplace variable; compliance matrix
S	strain tensor; vertical shear force at blade root
$S(s)$	sensitivity transfer function
t	time
$\bar{t}$	nondimensional time, $\bar{t} = \Omega t$
T	rotor period; stress tensor; rotor thrust, positive upward
T^*	kinetic coenergy of the rotor blade
$\mathbf{T}$	control response matrix
u	control input
u_P	velocity ratio of blade section, normal to disk plane
u_R	velocity ratio of blade section, in radial direction
u_T	velocity ratio of blade section, parallel to disk plane
U	section resultant velocity ratio, $\sqrt{u_T^2 + u_P^2}$
v	rotor induced velocity, positive downward through rotor disk
V	helicopter velocity with respect to the air; potential energy of the rotor blade; voltage across the piezoelectric
V_∞	velocity of the oncoming wind with respect to the helicopter, $V_\infty \approx -V$

W	matrix of white gaussian process noise
x	non-rotating coordinate positive aft; blade chordwise coordinate
$\underline{x}$	state vector
y	non-rotating coordinate positive to the right
$\underline{y}$	output vector
$\frac{1}{z}$	discrete time delay operator
z	vibration output; rotor coordinate, positive upward
$\underline{z}$	vector of vibration amplitudes
$\underline{z}_0$	vector of baseline vibration amplitudes
α	blade section angle of attack
α_d	rotor disk angle with respect to helicopter velocity
α_s	rotor shaft angle
β	flapping angle, positive upward; impermittivity matrix
γ	Lock number, $\rho acR^4/I_\mathrm{b}$
Γ_j	hub reaction matrices, see Appendix B
$\delta_{n,\mathrm{N}}$	blade summation operator
Δ_j	dynamic matrices, see Appendix B
ε	permittivity matrix
η	servoflap angle
θ	blade sectional pitch angle
θ_r	blade root pitch angle
θ_t	blade tip pitch angle
θ_tw	blade twist
θ_k	modal coordinate for the k th torsion mode
Θ_j	generalized force of blade
λ	rotor inflow ratio, $\lambda_f + \lambda_i$
λ_c	vertical climb inflow ratio
λ_f	free stream inflow ratio, $(V \sin \alpha_\mathrm{d} + v)/\Omega R$
λ_i	induced inflow ratio, $v/\Omega R$
Λ_j	aerodynamic matrices, see Appendix B
μ	rotor advance ratio, $V \cos \alpha_\mathrm{d}/\Omega R$
ν_β	blade flapping frequency
$\overline{\nu}_\beta$	normalized blade flapping frequency, ν_β/Ω
$\xi_\beta(r)$	blade flapping fundamental mode shape, $(r - e)$

$\xi_{\theta_k}(r)$	shape of the kth torsion mode
Ξ_j	generalized coordinate of blade
ρ	air density
σ	stress function; rotor solidity $Nc/\pi R$
σ_{d}	standard deviation of disturbance
σ_{z}	standard deviation of vibration
ϕ	section inflow angle, $\tan^{-1}(u_P/u_T)$
Φ_j	matrices to describe propeller moment, see Appendix B
ψ	azimuth angle of rotor blade
ψ_q	azimuth angle of qth rotor blade
Ψ_j	matrices to describe root pitch actuation, see Appendix B
ω_β	free-flapping frequency, $\sqrt{K_\beta/I_\beta}$
$\overline{\omega}_\beta$	normalized free-flapping frequency, ω_β/Ω
ω	frequency [rad/s]
$\overline{\omega}$	nondimensional frequency ω/Ω
ω_k	natural frequency of kth torsion mode
$\overline{\omega}_k$	normalized natural frequency of kth torsion mode, ω_k/Ω
Ω	rotor speed [rad/s]

Subscripts

0	collective
c	longitudinal cyclic
f	free stream
i	induced flow
k	torsional mode number
r	blade root
t	blade tip
tw	elastic blade twist
s	lateral cyclic

Superscripts

n	exponent on r, see Appendix A
*	normalized by I_{b}

Chapter 1

Introduction

Helicopters may be subject to a significant amount of vibration due to self-induced airloads resulting from blade vortex interaction. Vibration can reduce pilot and passenger comfort, fatigue helicopter components, increase maintenance and operating costs, and limit the effectiveness of sensitive electronics and instrumentation. Higher harmonic control can reduce these vibrations by oscillating the blade lift several times per rotor revolution to compensate for the periodic disturbances.

Although higher harmonic control can be achieved in the fixed frame through the swashplate, blade-mounted actuation in the rotating frame can provide more control degrees of freedom. As helicopter performance and vibration requirements tighten, blade-mounted actuation may be desirable, or even essential.

Piezoelectric materials appear promising as blade-mounted actuators, because they are electrically powered, solid state devices. Power can be delivered to the rotating frame through an electrical slipring, which is much simpler than a hydraulic slipring. Piezoelectric actuators may also be distributed, so that the sectional lift along the blade can be tailored, and complex lift distributions may be obtained. In addition, they have a high bandwidth, so that higher harmonic control can be achieved.

In this research effort, the feasibility of a piezoelectric servoflap to perform higher harmonic vibration control will be addressed. Conventional and higher harmonic control will be reviewed, and an overview of strain actuation materials, including piezoelectric ceramics, and some recent experiments involving the application of piezoceramic materials to rotor blades will be presented. In addition, wind tunnel data will be analyzed in order to identify typical helicopter vibration spectra, and to determine the achievable degree of vibration reduction. Finally, a linear time-invariant (LTI) state space rotor model will be derived in order to obtain transfer functions from control inputs to hub loads.

The state space rotor model can be used as a design tool to size and position the servoflap, and it will maintain a general form so that any actuation method may be incorporated. The model will be used to determine the feasibility of the servoflap to provide higher harmonic control, and the results will be compared with full blade feathering for the same purpose. Finally, the servoflap deflection amplitudes required for HHC should imply whether piezoelectric actuation is feasible for this purpose.

1.1 Helicopter Rotor Control

In a conventional helicopter thrust, pitch, and roll are provided by the main rotor. Yaw moments, including those for torque balance, are provided by the tail rotor. Many helicopters have systems which augment the conventional forces and moments. Some helicopter designs include horizontal tail stabilizers, lifting surfaces, and even turbojet thrusters in order to augment the forces and moments provided by the main rotor. In this research effort only the loads, motions, and control of the main rotor will be examined.

Rotor thrust can be controlled by either changing the rotational speed of the rotor or changing the pitch of the blades. It takes a long time to change the rotational speed of a rotor because it has considerable inertia. Generally, the rotational speed of the rotor is kept constant by the engine controls, and only the pitch of the blades is changed.

The collective pitch control provides a means of commanding the same pitch angle to each rotor blade simultaneously. As collective pitch is increased, the lift on the blades is increased, and therefore the thrust. Thrust is the primary force which governs the motion of the helicopter. It is directed upward, normal to the rotor hub.

In order for the hovering helicopter to move longitudinally or laterally the thrust vector must be tilted in that direction. This is achieved by the cyclic control. The cyclic control produces a sinusoidal blade pitch at the rate of one cycle per rotor revolution. The resulting sinusoidal variation in lift precesses the rotor, effectively tilting the rotor disk. The corresponding tilt of the thrust vector creates a pitch or roll moment, which rotates the aircraft. A large net change in thrust direction accompanies the rotation of the aircraft, and produces horizontal motion.

During forward flight, a blade on the advancing side of the rotor (toward the oncoming wind) will have a larger apparent airspeed than a blade on the retreating side. This will produce more lift on one side of the rotor than the other. The asymmetry produces an undesirable roll moment about the rotor hub. The condition is trimmed by use of the lateral cyclic control. The pitch of the advancing blade is reduced while the pitch of the retreating blade is increased, and the roll moment is reduced.

Individual blade control can be used to automatically track the rotor blades. Rotor blades are *in track* when the tip paths of all the blades coincide. Generally blade tracking is done open-loop, prior to flight. The relative positions of the blades are checked by flag, stroboscopic, or electronic methods [15, pg. 68]. If a blade is riding high or low the corrective action (usually changing the blade pitch at the root, or deflecting a trim tab on the blade) may be taken. If the rotor utilizes individual blade control methods, the blades may be automatically tracked in flight, which may lead to significant benefits. The Kaman Corporation performs automatic blade tracking on some of their controllable twist rotors [45].

A distributed actuation system may prove to be very valuable in improving the performance of helicopter rotors. By tailoring the lift distribution along each blade, both radial and azimuthal variations in rotor thrust may be achieved. Optimal pressure and inflow distributions about the rotor disk may lead to improved performance and aerodynamic efficiency of the rotor.

The rotor blades are subject to cyclic loads, as well as higher harmonic vibration.

These loads may fatigue the blades as well as transmit vibration to the helicopter. A closed-loop controller can be used to reduce, and in some instances eliminate, undue blade stresses and hub vibration. Higher harmonic control will specifically be covered in Section 1.3.

1.2 Rotor Control Methods

Collective and cyclic control of the main rotor is generally achieved by altering the pitch angles of the rotor blades appropriately. Rotor control, however, may be achieved by any method that significantly changes the lift characteristics of the blades. Full blade feathering, by far the most common, is only one such method. Other methods of rotor control include controllable twist and circulation control.

The most common method of rotor control is by the use of a swashplate, where the full blade is feathered according to pilot commands. There are many different mechanisms that operate like the swashplate. The importance is not in the mechanics of the system, but in the method of control. The motion of the system of blades is commanded in the helicopter fixed frame through collective, longitudinal, and lateral cyclic controls. The physical rotation of the rotor modulates the longitudinal and lateral commands to produce cyclic, sinusoidally varying blade pitch angles.

Some experiments have employed individual blade control (IBC) in order to perform full blade feathering [27]. The blades are independently controlled, unlike swashplate systems, where the motion of the system of blades is controlled. Individual blade control not only implies that commands are sent to each blade individually, but that a feedback loop exists for each blade in the rotating frame. A complication arises with IBC, because the actuators must now rotate with the blades. The actuators can be subjected to large centrifugal forces, and the command signals must pass from the fixed to the rotating frame. Individual blade control is possible through the swashplate for a three-bladed rotor [26].

Some helicopters use servoflap mechanisms for rotor control, where trailing edge flaps are used to change the lift characteristics of the rotor blades. A servoflap mechanism can be used for controlling the twist of a rotor blade, as well as for full blade feathering. Although each blade has its own flap, servoflap systems do not necessarily fall in the category of individual blade control. Servoflaps are often driven through pitch links to a swashplate.

Servoflap systems usually operate in aileron reversal. The downward deflection of a trailing edge flap will produce a moment about the airfoil, as well as some increment in lift. The moment twists the airfoil so that the angle of attack is decreased. In aileron reversal, the flap deflection will produce enough twist that the lift decrement of the entire airfoil overcomes any increment in lift that flap alone would have added. In a servoflap controllable twist rotor, aileron reversal is used to advantage. A low power actuator can be used to produce a large variation in total blade lift.

A servoflap mechanism can also be used for full blade feathering. The Kaman Seasprite helicopter uses such a system. The rotor blades are free to pitch but have soft torsional springs at the blade root. The servoflap, rather than controlling the twist of the blade, controls the pitch of the entire blade as a rigid body.

Circulation control rotors make use of the Coanda effect to vary the lift distribution of the blades. The Coanda effect is the phenomenon whereby a fluid jet will follow a boundary even though the boundary curves away from the fluid stream. Circulation control rotors utilize this phenomenon by using tangential blowing to delay separation from the rounded trailing edge of an airfoil. Circulation control airfoils can often achieve high section lift coefficients, with relatively little increase in drag.

1.3 Higher Harmonic Rotor Control

1.3.1 Sources of Higher Harmonic Vibration

The lift developed on each rotor blade produces a strong vortex at the blade tip, as well as weaker trailing and shed vorticity in the wake. In forward flight, an advancing blade will encounter the vortices of the blade that preceded it. In a survey of all the major wind tunnel and full scale flight tests from 1964 to 1983, Hooper [31] determined that the vibratory airloading of helicopter rotors is almost entirely due to blade vortex interaction. These effects create a significant amount of periodic aerodynamic loading at the blade passage frequency (N/rev). The vibration that the rotor blades encounter is transmitted to the helicopter through the rotor hub and pitch links. These self-induced loads can be responsible for fatiguing the rotor blades and airframe, acoustic noise, power losses, pilot and passenger discomfort, and unacceptable vibration levels for sensitive electronics and instrumentation.

1.3.2 Helicopter Vibration Requirements

In the late 1970's, the Army completed two of its largest helicopter development programs ever, the Utility Tactical Transport Aircraft System (UTTAS), and the Advanced Attack Helicopter (AAH) Programs. These programs helped to identify the problems and define the requirements for helicopter vibration. Three distinct areas in which helicopter requirements are usually divided are human factors, structural integrity, and the functional adequacy of equipment installed in the helicopter. Human factor considerations, however, represent the major concern of the contractor during development because of the instantaneous feedback from pilots and passengers, and the procurement activity in general [61].

The human body tends to attenuate vibration over 10 Hz, and acceptable vibration levels increase continuously with increasing frequency. The critical frequency range is usually between 4 and 8 Hz, where the human body's natural frequencies lie. Generally, human factor specifications are in terms of "Fatigue After 8 Hours," which means that working efficiency will be preserved up to 8 hours while operating at that particular vibration level. For simplicity, most studies use a four-bladed helicopter rotating at 300 RPM, so that the N/rev frequency is 4/rev at 20 Hz.

During the 1960's the requirements for helicopter vibration were specified in the U.S. Military Specification MIL-H-8501A [30]. This document specified that helicopter vibration levels must be less than 0.15 g. The UTTAS/AAH programs lowered the military specification further, by requiring a vibration level of 0.05 g or less at the pilot, copilot and passenger stations in steady speed conditions for vibration at the blade passage frequency N/rev. None of the contractors participating in the UTTAS/AAH programs could meet the 0.05 g requirement without an excessive weight penalty in vibration control devices. The requirement was raised to 0.10 g at 20 Hz, but 0.05 g was still required below 20 Hz.

A widely accepted standard for vibration exposure criteria is ISO-2631 [19], which reflects the results of tests performed during 1964–1972. It has been approved by nearly twenty nations, including the United States, and is the basis for the vibration exposure criterion in Section 5.8.4 of U.S. Military Standard MIL-STD-1472D [32]. It shows that the UTTAS/AAH requirements were not strict enough between 4 and 8 Hz, too strict between 10 and 20 Hz, and completely unacceptable over 20 Hz, as can be seen in Figure 1-1. The ISO-2631 curve is in terms of decreased proficiency boundary. Exposure limits for health and safety reasons can be obtained by raising the decreased proficiency boundary by a factor of 2. The reduced comfort boundary, which is required in transportation vehicles for reading, writing, and eating, can be obtained by dividing by a factor of 3.15.

At the AHS/NASA Rotorcraft Dynamics symposium in 1974, a panel meeting [74] reported that vibration levels at 1/rev can become discomforting at 0.03 g, and the levels of vibration perception can be an order of magnitude lower than that. Schrage and Peskar [61] recommended a linear relation between acceleration and frequency for maximum vibration levels, such as

$$g_{\mathrm{max}} = .004f + .01 \ , \tag{1.1}$$

where g_{max} is the acceleration level measured in g's, and f is frequency measured in Hertz. This gives approximately 0.03 g at 1/rev (5 Hz), 0.05 g at 2/rev (10 Hz), and 0.09 g at 4/rev (20 Hz).

The panel [74] also reported that perfectly acceptable vibration levels at a particular frequency may become intolerable if more than one vibratory frequency is present. This could have been the motivation for Gupta and Wood's recommendation of a flight spectrum approach to helicopter vibration specifications [21]. They

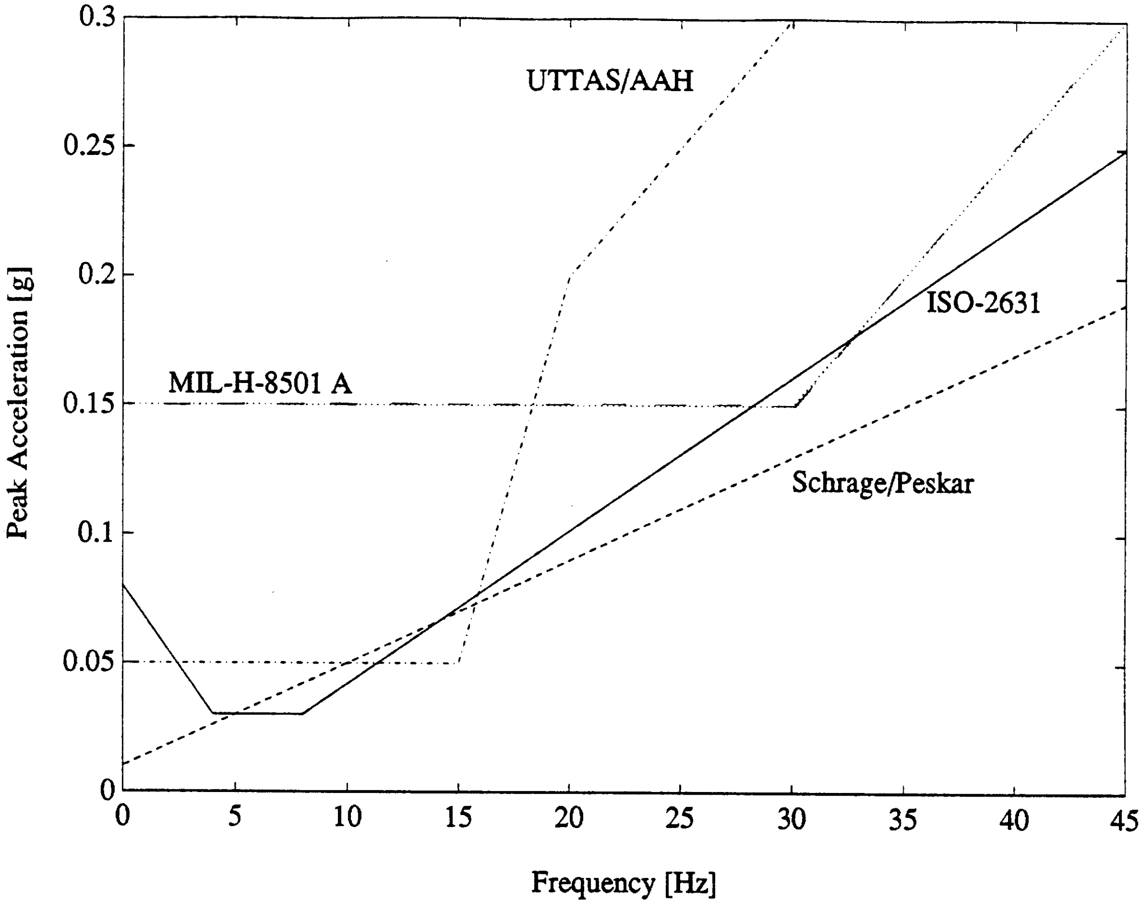

Figure 1-1: Human factor vibration requirements (adapted from Figure 1 of Schrage and Peskar [61]).

applied Miner's Rule for fatigue analysis of structural components to helicopter mission proficiency degradation. The proficiency curve of ISO-2631 replaced the typical S-N endurance limit curve for a structural component, while the helicopter's primary mission vibration spectrum was used in place of the typical load spectrum used for fatigue analysis. Compassionately, "For each helicopter evaluated, the calculation is carried out for that crew member with the most severe exposure."

The U.S. Army Tank Automotive Command (TACOM) conducted an extensive amount of research on whole-body vibration [39]. They found that intolerance to vibration was proportional to the relative motion occurring between various parts of the body. Furthermore, doubling the amplitude of the vibration would more than double the severity. This led to the deduction that "the severity of a vibration is proportional to the rate at which the body is absorbing energy." TACOM measured the vibration responses of 21 volunteer subjects, being average young males (28 years of age) of approximately 150 pounds, in over 1400 hours of testing. They measured the subjects vertical, lateral, and longitudinal power absorption, and found a large peak in the absorbed power curve at approximately 4.5 Hz. They attributed this vibration mode to the mass of the internal organs resonating with the diaphragm, which acts as a spring.

Scientists at the U.S. Army Applied Technology Laboratory and NASA Langley Research Center applied the TACOM method as well as the NASA Comfort Model (included noise as well as vibration), to five U.S. Army helicopters: a Bell UH-1H Iroquois; a Bell OH-58C Kiowa; a Bell AH1S modernized TOW Cobra; a Boeing CH-47C Chinook; and a Sikorsky UH-60A Blackhawk [28]. Above 80 knots, only one aircraft had levels below 0.09 watts. None of the helicopters could meet the specified absorbed power level requirement of 0.02 watts.

The Air Force no longer uses MIL-H-8501A. It has been superseded by MIL-F-83300 [17], which was last revised in 1991. This document has a "necessary and proper clause," which states, "throughout the Operational Flight Envelope, the aircraft shall be free of objectionable shake, vibration, or roughness. In addition, throughout the Operational Flight Envelope the aircraft shall not exhibit mechanical or aeroelastic instabilities that degrade the flying qualities."

1.3.3 Overview of Vibration Suppression Technology

Decades of research have been devoted to reducing higher harmonic vibration in helicopters. The attempts have taken various forms, ranging from passive isolation to active rotor blade control. Good reviews of passive vibration reduction methods are given by Reichert [57] and Loewy [40], while McCloud [43] includes multicyclic rotor control methods as well. Some of these techniques will be addressed in the following sections.

Vibration Isolation

Rotor vibration may be isolated from the helicopter airframe by active or passive means. Although the vibratory aerodynamic loading persists, the transmission of these loads to the rest of the helicopter are reduced. Some methods involve isolating the entire rotor and transmission from the helicopter airframe, while others involve isolating the pilot and passenger cabin.

The goal of vibration isolation concepts is to provide good low frequency isolation with relatively small displacements. Quite often, nodalization concepts may be used. Structural connections are made at beam nodes, where oscillating forces cannot be transmitted. Bell Helicopters developed a nodal beam gearbox mounting system so that the airframe was suspended from a beam connected to the gearbox [64]. The points of connection were beam nodes when the system was vibrating in response to rotor hub forces. The Kaman Corporation developed the Dynamic Anti-Resonant Vibration Isolator (DAVI), where the rotor transmission was mounted to the fuselage by special nodal isolator elements consisting of spring elements to which pendulums were attached [16, 58]. Bell Helicopters and Messerschmitt-Bolkow-Blohm (MBB) have experimented with systems that simplify the mechanics and improve the maintainability of such isolators. These systems include the Bell Liquid Inertia Vibration Eliminator (LIVE) [25], and MBB's Hydraulic Antiresonance Isolator [7], which use hydraulic plenums, rather than mechanical bearings.

MBB's Anti-Resonance Isolation System (ARIS) program applied both mechanical and hydraulic pendulums with tuneable masses to the BK-117 helicopter [8]. Flight tests as well as shake tests were performed on the helicopter. Vibration levels at the blade passage frequency were cited as less than 0.15 g for the entire forward speed range, and the isolation system weighed less than 1% of the maximum take-off weight of the BK-117.

Boeing Helicopters had success with an integrated floor/fuselage isolation system for the Model 234 Commercial Chinook [12]. The passenger floor as well as the fuel tanks were isolated from the airframe by passive nodal isolators. Vibration in the cabin could be lowered to 0.05 g on average.

Fuselage absorbers are another method of reducing helicopter airframe vibration. Usually these systems provide vibration reduction in a local area only. They are often mounted to the pilot seat, instrument panel, passenger cabin, or even fuel tanks. They are often comprised of tuned mass pendulums like the vibration isolators, but simply absorb the vibration without acting as structural connections.

Sikorsky developed a variable tune fixed frequency absorber for the S-76A [29], to address the wide RPM range of that aircraft. An absorber was placed in the nose of the commercial S-76A, and absorbers were placed in the nose and two overhead cabin locations for the Army's Black Hawk helicopter. It proved to be a reliable, inexpensive, and relatively weight efficient system.

Full isolation or absorption of a rotor vibration, requires isolators or absorbers in all axes. Elimination of more than one vibratory frequency will require devices tuned to each frequency. These systems may be heavier and more mechanically complicated than active systems. If the mechanical or hydraulic pendulums are replaced by electromechanical devices, passive systems may be adapted to active ones. A single active isolator can compensate for multi-frequency excitations without the need for several tuned devices. Active devices, however, rely on sensors, power, and a closed-loop control system in order to comprise an effective system. Therefore, weight, power, complexity, and reliability must be traded off in the design of such systems.

Passive Blade Methods

It is important to establish a criterion or goal to be met in the effort to reduce vibration. Isolating the rotor transmission or other structures from the fuselage, or absorbing vibration in particular areas, may provide specific local vibration reduction, but it will not reduce vibration levels at the hub. Cyclic blade stressing and material fatigue, acoustic noise, and power losses will still exist. In order to address these phenomena, vibration suppression in the rotating frame is essential. Several passive methods of rotor blade vibration suppression have been attempted, including pendulum absorbers, bifilar absorbers, and aeroelastically tuned tabs. These methods are discussed below, while active methods will be addressed in the following sections.

Hughes, Boeing, and MBB have all developed blade-mounted pendulum absorbers. The pendulum absorbers are mounted at the blade root, and may relieve vertical or inplane blade stresses, depending on their orientation. The absorbers rotate with the rotor and the restoring force for the pendulum mass is provided by centrifugal force. Therefore, the systems are self-tuning with rotor speed.

Vibration reduction efforts with the Hughes OH-6A helicopter led to a design that incorporated two pendulum absorbers for each rotor blade [2]. The OH-6A is a four-bladed helicopter, and it was determined that the primary source of the 4/rev vibration that this helicopter experienced were the 3/rev and 5/rev vertical shear forces that the blades were subjected to. Pendulum absorbers tuned to 3/rev and 5/rev were mounted to each blade root, and oriented to reduce the vertical vibration. The blade-mounted pendulums were able to reduce the vibration in the cockpit by 50%, but could last only 300 to 600 service hours, after which excessive wear would render them ineffective.

Boeing Helicopters developed a pendulum absorber system for its Model 347 four-bladed tandem rotor helicopter [67]. A 41 pound vertical pendulum was mounted to each of the helicopters eight blades. Experimental flight tests showed an 80 to 90% reduction in vertical hub shears, and 50 to 75% reduction in airframe vibration, but required an increase of gross weight by over 330 pounds.

A joint MBB-Boeing program used a combination of flap and lag pendulum absorbers to reduce vibration of the BO-105 helicopter in transition flight [18]. The helicopter has vibration levels of 0.1 g to 0.2 g above 50 knots, 0.3 g to 0.5 g in transition at 20 knots, and 0.5 g to 1.0 g in flares. The program used a system of 3/rev and 5/rev flap pendulums, with a 3/rev inplane pendulum. The combination of inplane and flap pendulums was able to reduce vibration levels at all flight speeds, and achieved a 50 to 80% reduction in transitional flight.

Sikorsky found that the principal source of vibration in its S-61 helicopter was inplane hub forces, and only minimal reduction could be achieved by desensitizing the coupled rotor transmission/airframe modes. A program was initiated to lower the vibration levels of this helicopter by the use of bifilar pendulum absorbers to counteract the 4/rev inplane rotor loads [50]. A reduction of vibration levels by 75% was achieved, resulting in cabin and cockpit levels of 0.1 g. The total vibration absorber system weighed 156 pounds.

Bielawa [5] studied the design of a passive tuned tab, with the objective of creating harmonic airloading of favorable amplitude and phase to cancel inherent blade motion. The tab would be appended near the trailing edge by either a hinge or a flexure and the spring rate would be tuned by proper selection of a mechanical spring or the material elasticity. Analytical studies showed some modest reductions in inplane hub shear, but increases in vertical hub loads.

Full Blade Feathering

Active control of the rotor blades is a potentially rewarding method of reducing higher harmonic vibration. It may provide vibration reduction at the rotor hub without the need for heavy pendulums that must be tuned to each vibratory frequency, or absorbers that provide only passive local area reduction. Active control systems can handle multi-frequency vibration, and are adaptable in flight. A popular method of active rotor control is blade root actuation, in which the entire blade is feathered. Boeing Helicopters, Hughes Helicopters, Sikorsky, Aerospatiale, NASA, and many others have investigated full blade feathering of articulated rotors for higher harmonic control.

Hughes Helicopters, the Army, and NASA completed a joint program in 1983, which involved flight testing a four-bladed OH-6A light (2500 lb.) helicopter equipped with full blade feathering HHC equipment [20, 75]. The flight test included both open and closed-loop testing. Electrohydraulic actuators were used to control the swashplate, and provided approximately ±2 deg blade pitch. Open-loop testing involved setting dials on electronic equipment inside the aircraft to minimize vibration. The dials controlled collective, lateral cyclic, and longitudinal 4/rev actuation signals, in both amplitude and phase. The best suppression of vibration was achieved with a combination of lateral and collective control, where the lateral component was the far more dominant. Vertical, lateral, and longitudinal accelerometer signals were fed back for closed-loop control. A cautious adaptive control algorithm was used, and provided close to 80% vibration reduction in most flight conditions. Vibration levels were kept on the order of 0.05 g for steady flight conditions up to 100 knots, and for

30 deg bank turns at 80 knots. However, vibration levels rose to 0.1–0.3 g in 1.75 g pullups at 80 knots (but still provided over a 50% reduction than with HHC off). During 40 knot decelerations in flare to hover, the controller would sometimes go out of phase, and exhibit mild divergence.

Higher harmonic control techniques were applied to a scale model BO-105, four-bladed, hingeless, helicopter rotor at the DFVLR Institute for Flight Mechanics in Braunschweig, F.R.G.[37]. The research effort involved determining the effect of 3, 4, and 5/rev control inputs to vibratory hub and blade loads. Three electrohydraulic actuators were used to control the swashplate, providing up to ±1 deg blade pitch. The actuators were able to provide excellent blade feathering accuracy to within ±0.012 deg amplitude and ±1.5 deg phase. Vibration level reductions on the order of 30 to 80% were achieved on the hub loads with a combination of 3, 4, and 5/rev open-loop controls.

After a decade of research effort, Boeing Helicopters concluded wind tunnel tests that successfully demonstrated closed-loop HHC on an articulated, three-bladed rotor in 1985. The model was a 1/6 scale, model CH-47D Chinook rotor [63]. Four electrohydraulic actuators were used to control the swashplate, providing ±3 deg of blade pitch. A slider was used for collective control, while the hydraulic actuators provided lateral and longitudinal cyclic trim, 3/rev higher harmonic control, and 2/rev performance control. The feedback signals were a combination of harmonic components from a load balance, as well as pitch link loads. Fixed gain, scheduled gain, and adaptive control algorithms were tested. Boeing found that the open-loop data response was very linear in the ±3 deg range, and repeatable to very high accuracy, which they attributed to the high precision of the actuators that they used. They were able to simultaneously suppress vertical and inplane 3/rev hub forces by 90%, continuously, as the model was "flown" throughout a wide test envelope, including trimmed flight up to 188 knots. It was found that fixed gain HHC methods were simple, fast, and provided adequate hub force suppression on the CH-47D. The secondary effects of HHC on CH-47D rotor performance and fatigue loads were acceptable. Furthermore, 2/rev control could improve rotor performance by amounts greater than any performance loss which was measured due to HHC for vibration suppression.

A research program sponsored by the French Government Agencies which included Aerospatiale, Giravions Dorand Industries, and Onera, led to the flight testing of a closed-loop higher harmonic control system in 1985 [55]. The HHC system was flown on a three-bladed, SA-349 Gazelle light helicopter up to 250 km/h. The program included open-loop identification as well as closed-loop vibration suppression. The electrohydraulic actuators that were used could provide ±1.7 deg of blade pitch, but were limited to ±0.8 deg, due to large dynamic loads encountered during open-loop testing. A stochastic adaptive regulator with vibration estimation was found to work best. Vibration reductions of 80% were achieved on average, for steady and accelerated flight, maneuvers, climbs, and descents. Vibration levels of 0.1 g were attained.

Sikorsky flight demonstrated an HHC system on a four-bladed, medium size (10,000 lb.) S-76 helicopter in 1985 [47, 69]. The flight tests were performed open-loop, up to 150 knots. Electrohydraulic actuators provided ±1 deg blade pitch. Simultaneous vibration reduction at several locations in the cabin was achieved, by properly tuning the actuator signals. Under 100 knots, vibration levels were reduced from 0.3–0.5 g to around 0.1 g. Vibration levels increased rapidly with airspeed over 100 knots, due to the ±1 deg blade pitch limit. With larger higher harmonic blade pitch angles, a 0.1 g vibration level could have been achieved, for flight conditions over 100 knots. Larger HHC blade pitch angles, however, require increased hydraulic fluid flow rates, a larger capacity pump, reservoir, and cooling system. Increasing the maximum amplitude of the HHC system from ±1 deg to ±2 deg (which may have been sufficient), would have amounted to an estimated 30% increase in HHC system weight.

Circulation Control

Circulation control rotors most often utilize the “Coanda Effect,” by using tangential blowing to delay separation from the rounded trailing edge of an elliptically shaped rotor blade. Blown airfoils can achieve high section lift coefficients without moving the blade, and higher harmonic control can be achieved without any moving parts other than the rotating blades.

The performance of a circulation control rotor is affected by variables such as slot height-to-chord ratio, slot height-to-trailing edge radius ratio, Reynolds number and Mach number, as well as jet flow pressure and velocity [73]. The advance of circulation control technology is dependent upon the evolution of composite materials, and advanced manufacturing technology. Circulation control rotor blades must often incorporate thickness and camber taper, a thin full span slot located very near the trailing edge, a hollow internal passage for airflow, structural integrity at high internal airflow operating temperatures, and high torsional blade stiffness with conventional blade bending stiffness.

The Naval Ship Research and Development Center [73] has directed the majority of circulation control projects. Circulation control research has been performed by NASA [73, 44], Giravions Dorand [44], Lockheed [76], Boeing [56], Kaman [35, 54], and Sikorsky [71]. Tests of the first generation circulation control model were conducted in 1971, under joint sponsorship of the Naval Air Systems Command and NASA [73]. The Higher Harmonic Circulation Control (HHCC) rotor model [73] demonstrated the high lift capability, and efficiency of circulation control rotors, as well proving that trimmed flight could be achieved without any moving parts other than the rotating blades. The rotor was an 80 inch diameter, four-bladed circulation control rotor, with elliptical shaped blades that used trailing edge tangential blowing. The trailing edge blowing slot was near the 95% chord location and extended over 90% of each blade length. The rotor had conventional collective control (set manually), but cyclic and higher harmonic control was performed by blowing. Blowing control was achieved by a system of cams located at the center of the rotor hub. The amplitude of cyclic or higher harmonic control was controlled by raising or lowering the respective cam. Phasing was achieved by turning a control rod, changing the azimuthal orientation of the cam. As the hub rotated, nozzles leading to the blades would be opened or closed, responding to the cams. Once the cams were properly set, the only moving parts were the rotating blades. The first generation HHCC was able to demonstrate rotor trim, lift augmentation, autorotation, and 2/rev performance control.

Giravions Dorand in Suresnes, France has built and tested several circulation control jet-flap designs including the 40 ft diameter DH-2011 "Dorand Jet-Flap," built for the U.S. Army and NASA [44]. The rotor was tested several times at the NASA Ames 40 × 80 ft wind tunnel. The rotor was two-bladed, with a teetering hub, and blade coning offset hinges, but no feathering hinges. The rotor was driven and controlled by a propulsive jet flap, which occupied the outer 30% of the blade radius. Multicyclic 2, 3, and 4/rev were applied by a cam, while conventional collective and cyclic control was provided by a swashplate. The 1971 tests demonstrated a 50% reduction in stress and vibration levels, at advance ratios from 0.4 to 0.6.

Nonpropulsive circulation control jet flaps were studied for the U.S. Army Air Mobility Research and Development Laboratory (USAAMRDL), and NASA Ames Research Center, in 1974 [54]. Half span, nonpropulsive jet flaps were analytically investigated for application to the Bell UH-1A rotor. The investigation included both two-bladed and four-bladed versions with offset flapping hinges. The objective was to eliminate transmitted root shears and study the effect on blade bending moments, and total power. Conventional collective and cyclic controls were used for trim, while 2–11/rev jet flap oscillations were considered for multicyclic control. Elimination of root shears was demonstrated for each rotor, and interestingly it took less power if the jet-flap actuated blade operated in aileron reversal, than if it operated conventionally.

Under contract with the U.S. Naval Air Systems Command, the Kaman Corporation began the design, development, and testing of full scale circulation control hardware in 1975 [35]. The contract culminated in the first flight of a full scale circulation control rotor in 1979. The objective was to reduce the maintenance and improve the reliability of helicopter rotors. Circulation control was used to eliminate the many highly loaded, oscillating rotor components, reduce vibration levels by multicyclic control, and improve payload/performance and heavy lift capability. The XH-2/CCR was the first full scale application of circulation control technology to rotary wing aircraft. It could not be flown over 26 knots, however, due to blade stall (circulation control blowing was used for collective as well as cyclic control). The

Navy cancelled the program before flight tests of multicyclic circulation control could be performed.

Perhaps the most likely candidate for multicyclic circulation control was the X-wing rotor. The X-wing concept was to combine VTOL capability with efficient high speed cruise, typical of fixed wing aircraft. The design incorporated a very stiff four-bladed, hingeless rotor, with leading and trailing edge circulation control blowing. A conventional collective system was combined with cyclic circulation control. The X-wing would take-off, and hover like a helicopter, with the rotor in the "X" configuration. The vehicle would then be operated as a fixed wing aircraft, with an expected maximum speed of 400 knots. Leading edge blowing would be essential, because it permits high lift in the reverse flow region. As the rotor is stopped, the reversed flow region grows to the full length of the retreating blade.

The X-wing presented many challenges from a vibration standpoint. Since the stopped rotor would have two forward swept wings, the blades had to be several times stiffer than conventional rotors. This required very high bandwidth control. In addition, a hingeless rotor transmits greater vibratory moments and shears to the hub, than an articulated rotor. Furthermore, as the rotor is stopped the blade passage frequency continuously decreases to zero, and is thus capable of exciting many modes of the rotor/fuselage system. X-wing programs have been developed at Boeing Helicopters [56], Lockheed [76], and Sikorsky [71], under direction of the Naval Ship Research and Development Center and NASA.

The 1988 Sikorsky/United Technologies Research Center wind tunnel tests of the X-wing rotor are of particular interest because of the extensive higher harmonic control research that was performed [71]. A 1/6 scale, 10 ft diameter rotor was tested at normal rotor speed up to 175 knots, and at 150 knots for a range of steady rotor speeds typical of conversion. A man-in-the-loop HHC and trim control system was used to simultaneously reduce 4/rev rotor balance and rotor stand vibration, while automatically maintaining rotor trim. The blowing control was achieved by a system of 48 individually actuated butterfly valves located at the rotor hub, in two rings of 24 valves equally spaced in azimuth. The lower set was used for leading edge blowing, while the upper set was used for trailing edge blowing. Eight receiving ducts channelled the air to the leading or trailing edge of each of the four blades as the system rotated. The receiver opening was as wide as two valve assemblies, so that as it rotated, it was exposed to the open area of at least two valves at all times (the NSRDC X-wing model had only eight azimuthal blowing locations, which they believe resulted in an unusually large amount of 8/rev vibration). The open-loop HHC system achieved 70–95% reductions in fixed system vibration, keeping the vibration level in the 0.05–0.10 g range. No conversions or closed-loop HHC algorithms were flown.

Controllable Twist

Controlling the twist of a rotor blade is yet another method of achieving helicopter rotor control. The most likely method of achieving blade twist is by the use of a servoflap mechanism. Servoflap designs generally require less actuation power than root pitch actuation, and have the advantage that they virtually eliminate the transmission of large oscillating pitch link loads to the airframe.

Early research in servoflap controllable twist was performed by Carpenter and Paulnock [9], and Payne [51]; however, the majority of current has been conducted by the Kaman Corporation, with some testing performed at NASA/Ames Research Center [45, 59, 70, 38]. Kaman has investigated using the servoflap for full blade feathering as well as controllable twist, and has used it for collective, cyclic, and multicyclic control, as well as automatic blade tracking. Two of Kaman's production helicopters that use servoflaps are the SH-2 Seasprite, which has rigid blades with soft torsional root springs, and servoflap controlled full blade feathering; and the K-1200 Synchropter which has dual two-bladed intermeshing rotors, teetering blades with no feathering, and servoflap controllable twist.

Kaman concluded a wind tunnel investigation of multicyclic control on a 56 ft diameter, four-bladed, controllable twist rotor in 1978 [45]. The wind tunnel tests were conducted in the NASA-Ames 40 × 80 Foot Wind Tunnel, and sponsored by both the U.S. Army and NASA. The rotor was fully articulated with a conventional pitch horn to provide primary control. The rotor blades were soft in torsion, so that the servoflap could be actuated collectively and cyclically to control the blade torsional response. Cyclic servoflap deflection was performed by a swashplate, while multicyclic control was introduced by electrohydraulic actuators in the rotating system. Any combination of 2, 3, and 4/rev harmonic servoflap deflection, and phase could be commanded. The maximum servoflap deflection was 6 deg. The test envelope included advance ratios from 0.22 to 0.33, shaft axis inclinations from -6 to -10 deg, and root collective settings from 8 to 12 deg. Kaman concluded that flatwise bending moments could be reduced by 22% to 30%, while control loads could be reduced by 83%.

1.3.4 Higher Harmonic Control Algorithms

The airloading of a rotor blade is essentially periodic, and can be decomposed as a the sum of harmonics of the rotational frequency. For an N-bladed rotor, only vibration at harmonics of the blade passage frequency, N/rev, will get transmitted to the fuselage. The loading at other rotor harmonics will cancel, due to the net contribution of the N blades [34, pg. 347]. The sources of N/rev airframe vibration include N/rev vertical forces, as well as (N-1)/rev and (N+1)/rev inplane shears and moments. The concept underlying HHC is that reduction of N/rev airframe vibration can be achieved by changing the aerodynamic properties of the blades by oscillations at (N-1)/rev, N/rev, and (N+1)/rev. Figure 1-2 illustrates the transmission of harmonics from the rotating frame to the fixed frame, and vice versa.

Higher harmonic control can be achieved in either the fixed or rotating systems. Fixed frame actuation is generally implemented through a swashplate. Cosine and sine signals at the N/rev frequency are used to command collective, lateral cyclic, and longitudinal cyclic controls in amplitude and phase. These commands are modulated by the rotor rotation to produce (N-1)/rev, N/rev, and (N+1)/rev variations in blade loading. If an actuation method is implemented in the rotating frame, then cosine and sine signals at (N-1)/rev, N/rev, and (N+1)/rev are commanded explicitly.

Any combination of hub load, pitch link load, or fuselage vibration harmonics

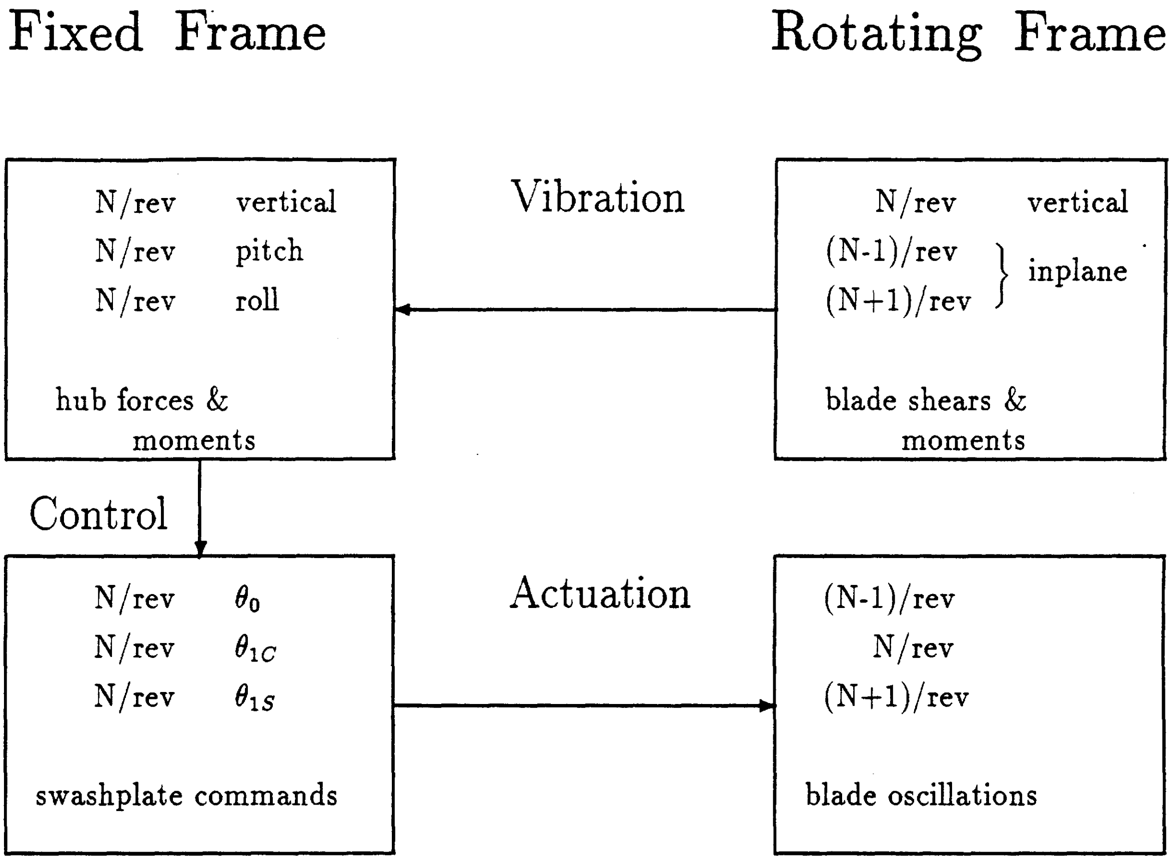

Figure 1-2: Transmission of harmonics.

can be used as feedback signals for higher harmonic control. The relationship between input harmonics and steady hub load harmonics are approximately linear, and can therefore be described by a matrix of constant coefficients [62]. Likewise, the relationship between hub load harmonics and fuselage harmonics are approximately linear, and can also be described by a matrix of constant coefficients. Multiplication of these matrices results in a constant coefficient control response matrix, **T**, which relates Fourier coefficients of the N/rev input control harmonics to the N/rev output vibration harmonics.

Discrete-Time Higher Harmonic Control Method

One of the earliest higher harmonic control algorithms, suggested by Shaw [62], assumes knowledge of the control response matrix, **T**. A harmonic analysis of the feedback variables is required at each step in the algorithm, in order to obtain the sine and cosine components of the N/rev frequency. The N/rev components are then multiplied by the inverted control response matrix, $\mathbf{T}^{-1}$, to produce N/rev swashplate commands to reduce the measured loads. If the control response of the helicopter is essentially quasisteady, the algorithm should produce deadbeat control, and eliminate the N/rev vibration in a single step [24].

Using the quasisteady assumption, the sine and cosine components of the N/rev vibration may be represented by

$$\underline{z} = \mathbf{T}\underline{u} + \underline{z}_0 \ , \tag{1.2}$$

where $\underline{z}$ is a vector of vibration amplitudes, $\underline{u}$ the vector of N/rev swashplate control amplitudes, and $\underline{z}_0$ is the vector of uncontrolled vibration amplitudes at zero swashplate deflection. The vibration levels, $\underline{z}$, are measured at each time step, and a swashplate input, $\underline{u}$, is adjusted to cancel the measured disturbance. The resulting control law is

$$\underline{u}(n+1) = \underline{u}(n) - \mathbf{T}^{-1}\underline{z}(n), \tag{1.3}$$

where the index n denotes the time step. A block diagram of the discrete time higher harmonic control algorithm is shown is Figure 1-3.

Fixed Gain and Scheduled Gain Algorithms

There are several philosophies concerning the control response matrix $\mathbf{T}$. Some researchers argue that it is fairly constant with flight conditions, and a fixed gain controller is adequate [63], while others argue that it varies significantly with flight condition and that real time identification will lead to the best controller [48]. These drastically different viewpoints have led to a variety of HHC control methods including a variety of fixed gain, scheduled gain, and adaptive controllers.

A fixed gain control algorithm is perhaps the most easily implemented algorithm. Only a single control response matrix must be identified, and gains are precomputed off-line, therefore very little computational effort is required. Fixed gain algorithms, however, cannot adapt to changing flight conditions and may provide suboptimal or inadequate performance.

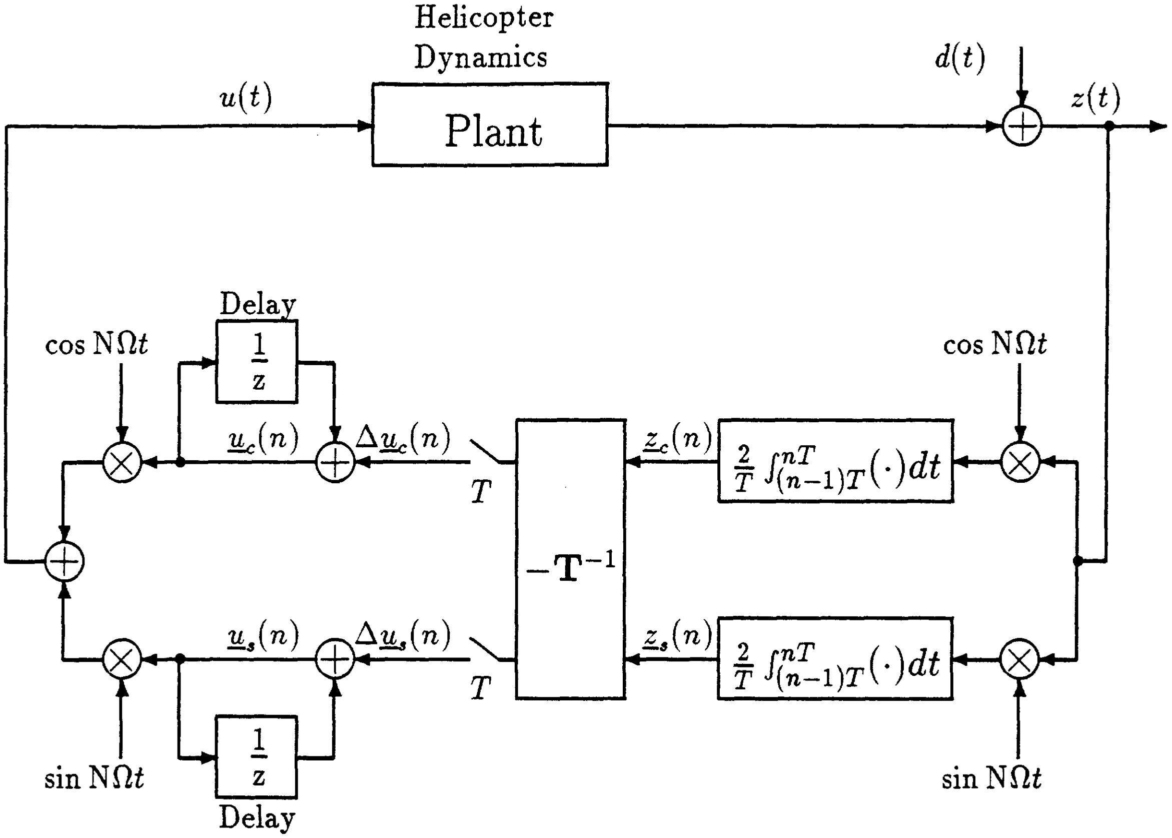

Figure 1-3: Block diagram of the discrete-time HHC algorithm (adapted from Figure 3 of Hall and Wereley [24]).

A scheduled gain controller has the advantage of being able to accommodate varying flight conditions. The control system, however, must be able to determine the flight conditions, as well as store a large number of control response matrices. These matrices must be identified prior to closed-loop operation. Scheduled gain controllers must also be free of transients and instabilities when switching from one library matrix to another.

Although the rotor flow field produces periodic disturbances, which cause the dynamics of the rotor to be periodic, an LTI model of the helicopter may often be used. Therefore, common modern control methods may be employed. One useful approach is based upon the Linear-Quadratic-Gaussian (LQG) controller [41, pg. 223]. If the vibration is to be minimized without excessive control amplitudes, a reasonable criterion to be minimized is a cost functional such as

$$J = \lim_{t_f \to \infty} \frac{1}{t_f} \int_0^{t_f} \{\underline{z}'Q\underline{z} + \underline{u}'R\underline{u}\}dt \ , \tag{1.4}$$

where t_f is the time interval, Q is a state weighting matrix, and R is a control weighting matrix. If the **T** matrix is known perfectly, a closed form solution may be found which minimizes the cost functional. After solving the appropriate Ricatti equation, the optimal control solution is simply a constant gain feedback control law of the form

$$\underline{u} = G\hat{\underline{z}}_0 \ , \tag{1.5}$$

where the feedback gain matrix is

$$G = -(\mathbf{T}^T Q \mathbf{T} + R)^{-1} \mathbf{T}^T Q \ . \tag{1.6}$$

The feedback gain G is precomputed off-line and stored as a function of flight condition. The baseline vibration $\underline{z}_0$ can be determined from a simple linear Kalman filter, with the filter gains also precomputed [20]. Even though the vibration may be estimated, the algorithm is not adaptive because the vibration state appears linearly in the control law, and the **T** matrix is not identified on-line.

Frequency Shaped Cost Functionals

The application of state feedback methods for vibration control is complicated by the presence of all frequency components in the feedback states. A vibration minimizing controller can actually aggravate fuselage dynamics and blade structural modes. Gupta and DuVal [23] proposed a method of dealing with this problem, by using a tuned state feedback method. It is an application of the frequency shaped cost functional extension of the Linear-Quadratic-Gaussian (LQG) proposed by Gupta [22].

Frequency dependent penalties can be placed on both the states and the control amplitudes in the formulation of the cost function to be minimized. The frequency shaped cost functional has the form

$$J = \int_{-\infty}^{+\infty} \left\{ \underline{z}^H(j\omega) Q(\omega) \underline{z}(j\omega) + \underline{u}^H(j\omega) R(\omega) \underline{u}(j\omega) \right\} d\omega \ , \tag{1.7}$$

where the superscript H refers to the Hermitian (complex conjugate transpose) of the matrix. Note that the state weighting matrix, Q, and the control weighting matrix, R, are frequency dependent.

The vibration to be eliminated can be passed through a second order undamped filter tuned to resonate at the blade passage frequency, NΩ. This filter has the form

$$G_{\mathrm{N}}(s) = \frac{(\mathrm{N}\Omega)^2 s}{s^2 + (\mathrm{N}\Omega)^2} \ . \tag{1.8}$$

The resonance of the filter makes the weighting function $Q(\omega)$ very large at the N/rev frequency. The filter states can be adjoined to the plant states to form an augmented state vector, and the Linear-Quadratic-Regulator (LQR) solution will yield the optimal feedback gains. The resulting system acts like a phase-locked loop, since the control signal is 180 deg out of phase with the vibration at the filter's resonant frequency. The control is able to lock onto the vibration phase and amplitude without the need for harmonic analysis.

A controller with frequency shaped cost functionals was implemented on the Rotor Systems Research Aircraft (RSRA) and tested in the NASA/Langley Transonic Dynamics Wind Tunnel [14]. The design worked well for flight speeds at 5 knots, 40 knots and 120 knots. It should be capable of operation in maneuvering flight.

Adaptive Algorithms

Adaptive algorithms can accommodate varying flight conditions, without the need to identify the flight conditions or store large numbers of matrices. The control response matrix is identified on-line rather than precomputed. Generally a Kalman filter is used to estimate the control response matrix, $\mathbf{T}$, as well as the baseline vibration level, $\underline{z}_0$.

If the vibration amplitude and control response matrix vary with flight conditions, they can be represented by a random walk model

$$\mathbf{T}(n+1) = \mathbf{T}(n) + W(n) , \tag{1.9}$$

and

$$\underline{z}_0(n+1) = \underline{z}_0(n) + \underline{w}_0(n) . \tag{1.10}$$

The $W(n)$ matrix and $\underline{w}_0(n)$ vector are zero mean white gaussian process noise. The optimal cost-to-go is obtained by performing an ensemble average over all time steps n, for $(n = 1, N)$. The optimal cost-to-go is

$$J^* = \min_{\underline{u}(n)} E\left\{ \sum_{n=1}^{N} [\underline{x}^T(n+1) Q \underline{x}(n+1) + \underline{u}^T(n) R \underline{u}(n)] \right\} , \tag{1.11}$$

where n is the time index, and $E\{\cdot\}$ denotes the expected value. Q is a state weighting matrix, and R is a control weighting matrix as before. The difficulty in calculating a solution is that the elements of the $\mathbf{T}$ matrix vary randomly, and the expectation cannot be obtained exactly. A closed form solution does exist if equation (1.11) is minimized for only one time step ($N = 1$). This is referred to as a one-step method. Molusis *et al.* [48] review a number of adaptive control schemes including "caution" and "probing." Adaptive algorithms tend to be much more complicated than fixed or scheduled gain algorithms, and are usually computationally intensive. The estimates can diverge and lead to instability in the algorithm, especially for rapidly maneuvering flight.

Experimental Comparison of HHC Algorithms

An extensive evaluation of higher harmonic control concepts was performed by the Army on an aeroelastically scaled rotor model in the NASA-Langley Transonic Dynamics Tunnel in 1981 [48]. The tests included six basic control concepts ranging in sophistication from a full adaptive controller to a gain scheduled Linear-Quadratic-Gaussian design. It was found that both deterministic and cautious adaptive controllers were able to track and maintain low vibration levels for various advance ratios, and the cautious controller could maintain low levels for rapidly maneuvering flight conditions as well. The open and closed-loop properties of the control response matrix revealed significant differences, which led to the conclusion that the elements of the **T** matrix are dependent upon the higher harmonic controls themselves, and that this could be the reason that the scheduled gain algorithms that were attempted, exhibited very poor performance. No conclusions concerning scheduled gain algorithms were made, since the problems were not fully understood.

During wind tunnel tests of a CH-47D Chinook model, Boeing Helicopters "flew" several HHC control algorithms including fixed gain, scheduled gain, and adaptive algorithms [63]. Up to 90% vibration reduction was achieved with a fixed gain algorithm. The success of this algorithm was attributed to several reasons: 1) very precise swashplate control; 2) a linear, and fairly constant, smoothly varying control response matrix from 50 to 150 knots; 3) and accurate open-loop identification of the control response matrix. The scheduled gain control algorithm also worked well, but did not provide much advantage over the previously discussed fixed gain algorithm. A local adaptive controller was also found to be successful in suppressing certain feedback variables, but the T matrix tracking accuracy was low, and the matrix estimate would diverge for some flight conditions. A global adaptive controller was found to be either unstable or ineffective, and time did not permit a full evaluation.

An analytical simulation of fixed gain and adaptive control algorithms was performed by Nygren and Schrage [49] using the Dynamic System Coupler (DYSCO) Program, in an attempt to determine the adequacy of each for higher harmonic vibration reduction. Their study concluded that fixed-gain and both global and local adaptive controllers perform adequately in medium and high speed flight, but the effectiveness is greatly reduced for all cases where the control response matrix is incorrectly initialized. The adaptive regulators were able to quickly adapt to reduce vibration when incorrectly initialized, and performed effectively throughout all maneuvers tested. The fixed-gain regulator performed effectively provided that flight conditions did not change by more than 20 knots.

1.4 Thesis Overview

The objective of this thesis is to determine the feasibility of blade-mounted actuation (especially piezoelectric servoflap actuation) for helicopter rotor higher harmonic vibration control and conventional rotor control. This is accomplished by developing a state space model of the rotor by making several simplifying assumptions that yield time-invariant dynamics. The model is then used to compute transfer functions from control inputs to hub loads. Since the rotor model is time-invariant, the transfer functions from actuator input to hub forces exist at each frequency, and hub responses can be predicted for actuation at cyclic and multicyclic frequencies, as well as steady state. Finally, the blade-mounted actuator is specified in terms of its lift coefficient (c_{l_η}) and moment coefficient (c_{m_η}), so that any actuation method may be modelled.

A trailing edge servoflap is included in the state space model for the H-34 research rotor, in order to investigate blade-mounted actuation. The model is used to generate transfer functions from servoflap deflection to hub loads, and the thrust response is used to determine the ability of the servoflap to provide conventional and higher harmonic control. The amplitude of servoflap deflections required for rotor control will determine whether piezoelectric servoflap actuation is feasible.

In Chapter 2, helicopter vibration spectra are computed from wind tunnel data provided by Boeing Helicopters [63]. Hall and Wereley [24] have suggested that the vibration producing disturbances may be stochastic, rather than deterministic processes, so that the correlation time of the disturbance and the velocity constant of the higher harmonic controller will determine the achievable performance of HHC algorithms. The wind tunnel data is analyzed in light of this methodology, to determine the degree of higher harmonic vibration suppression that is possible, based on the open-loop spectrum.

In Chapter 3, piezoelectric actuation is introduced, and the fundamentals of piezoelectric operation are presented. In addition, three methods of piezoelectric actuation for aerodynamic tailoring are reviewed that include bend/twist and extension/twist coupled composite plates (Crawley and Lazarus [10]); directionally attached piezoelectrics for rotor blade twist actuation (Barrett [4]); and piezoelectric servoflap actuation (Spangler and Hall [66]).

Chapter 4 contains the derivation of the rotor dynamics and the development of the state space rotor model. Multiblade coordinates are used to describe the dynamics of the rotor, and to represent the motions of the rotor disk. The blade dynamics include a rigid pitch mode and elastic torsion modes, so that full blade feathering and controllable twist can be studied. In addition, root pitch actuation and blade-mounted actuation are incorporated in the model. Finally, linear section aerodynamics are assumed with dynamic inflow.

Results of the state space model for the H-34 research rotor are presented in Chapter 5. The transfer functions from servoflap inputs to hub loads are computed to determine the servoflap deflection requirements for conventional and higher harmonic control. The thrust responses that can be achieved with root pitch actuation and servoflap actuation are compared, and parametric analyses are presented for blade stiffness, servoflap size and placement, and advance ratio. Finally, the conclusions are presented in Chapter 6.

Chapter 2

Rotor Vibration Spectrum from Wind Tunnel Data

Traditionally, higher harmonic disturbances were assumed to produce sinusoidal oscillations at the blade passage frequency. Under this assumption the HHC methodology of Shaw [62] should provide complete disturbance rejection. However, the results from wind tunnel tests have shown, at most, a 90% reduction in vibration levels using higher harmonic control. Hall and Wereley [24] have suggested that vibration producing disturbances may be stochastic rather than deterministic processes, which could account for the discrepancy. If the vibrations have a stochastic nature, then the correlation time of the disturbance, as well as the *velocity constant* of the HHC controller, will play a major role in determining the achievable performance of HHC algorithms. Hall and Wereley have developed a method of evaluating the performance of HHC algorithms in terms of classical control theory, which allows for the comparison of both continuous and discrete-time algorithms.

In light of the methodology developed by Hall and Wereley [24], helicopter rotor wind tunnel data will be analyzed, in order to characterize the vibration spectrum, and to determine the degree of possible reduction using HHC. The wind tunnel data was obtained from Boeing Helicopters, and corresponds to the higher harmonic control experiments described in Shaw *et al.* [63]. In this Chapter, the method developed by Hall and Wereley will be discussed, the wind tunnel test will be described, and the method of reducing the data will be covered. Finally, wind tunnel vibration spectra, and the implication for the degree of HHC vibration reduction that is possible will be presented.

2.1 HHC Disturbance Rejection Theory

The higher harmonic control methodology developed by Shaw [62] assumes knowledge of the control response matrix $\mathbf{T}$, which relates the Fourier coefficients of control inputs to the Fourier coefficients of the vibratory hub loads. Whether the HHC algorithms use fixed gain or adaptive controllers, the basic architecture of all HHC algorithms resembles that of Shaw. The bandwidth of the controller is generally assumed to be low enough that the plant dynamics are essentially quasisteady, and a linear time periodic assumption can be made. Under the quasisteady assumption, inversion of the control response matrix should produce deadbeat control, eliminating the N/rev vibrations in a single step.

Hall and Wereley [24] have shown that HHC is fundamentally similar to the sinusoidal disturbance rejection techniques of classical control theory. In the classical case, the goal is to reject constant or sinusoidal disturbances from the output of a linear time invariant (LTI) system. In HHC, the goal is to reject periodic disturbances at the blade passage frequency, where the plant dynamics are linear time periodic (LTP). The continuous-time HHC compensator has been shown to be analogous to a narrow band disturbance rejection filter, when a linear time invariant assumption has been made.

The LTI system can be represented by its transfer function $G(s)$, and a compensator $H(s)$. The disturbance is assumed to act on the plant output, so that

$$z(t) = y(t) + d(t) \,, \tag{2.1}$$

where $z(t)$ is the output, $d(t)$ is the disturbance, and $y(t)$ is the plant output due to the control input $u(t)$. Therefore, the Laplace transform of the output may be

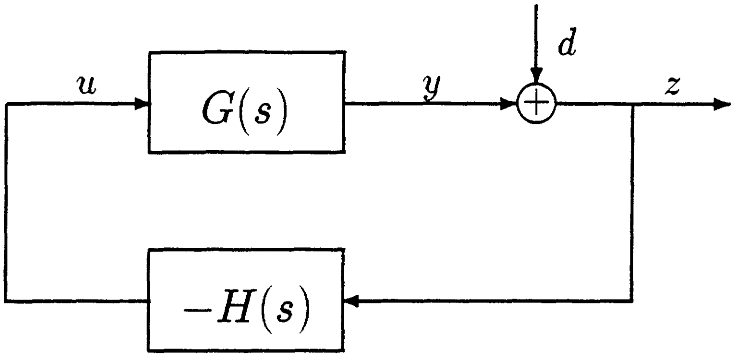

Figure 2-1: Block diagram of closed-loop compensation.

written as

$$z(s) = G(s)u(s) + d(s)\ . \tag{2.2}$$

For the closed loop system, the feedback control has the form

$$u(s) = -H(s)z(s)\ . \tag{2.3}$$

The resulting control system is illustrated in Figure 2-1. The goal of disturbance rejection is to make the response in the output due to the disturbance small, in the frequency range where the disturbance has considerable energy. In the single input single output (SISO) case, the response of the output due to a disturbance, $z(s)/d(s)$, is given by the sensitivity $S(s)$ where

$$S(s) = \frac{1}{1 + G(s)H(s)}\ . \tag{2.4}$$

The sensitivity can be made small in a particular frequency range by making $G(s)H(s)$ large in that range, but it is also important to choose $H(s)$ so that the resulting closed loop system is stable. In order to reject disturbances at a given frequency ω_0, a second order oscillator with a natural frequency ω_0 may be used. The resulting compensator

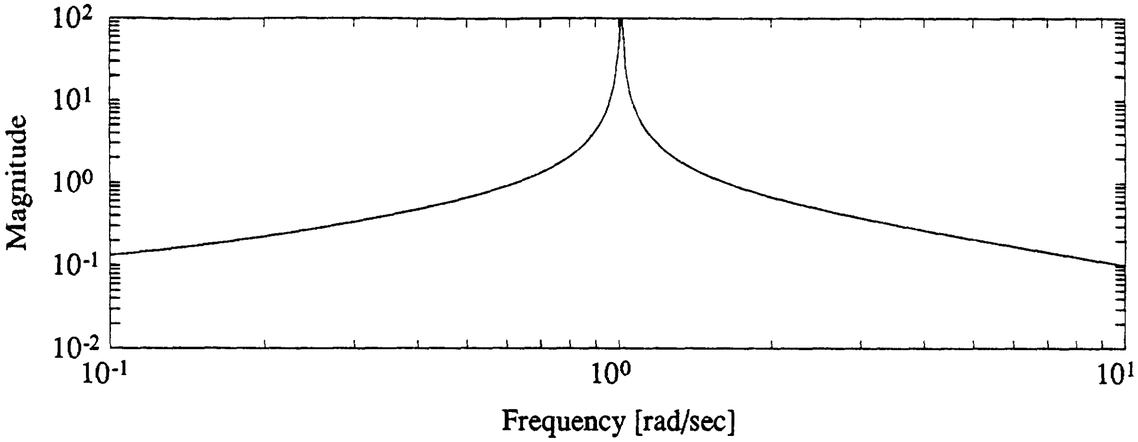

Figure 2-2: Typical transfer function of a disturbance rejection compensator centered about $\omega_0 = 1$.

is

$$H(s) = \frac{c_1 s + c_2}{s^2 + \omega_0^2} \ . \tag{2.5}$$

The coefficients, c_1 and c_2, in the numerator of the transfer function determine the location of the zero in the compensator, and must be chosen so that the open loop transfer function has adequate gain and phase margins. These coefficients also govern the width of the notch in the sensitivity transfer function. Figure 2-2 depicts the typical shape of a narrowband compensator.

Hall and Wereley have shown that the discrete time higher harmonic compensator depicted in Figure 1-3 can be implemented in continuous time with some slight modifications. By eliminating the sample and hold structure, and replacing the integral over a rotor period by a continuous Laplace integrator $1/s$, the discrete-time higher harmonic controller can be implemented in continuous-time. A direct comparison between the discrete and continuous-time controller can be achieved if $k = 1/T$. Figure 2-3 illustrates the continuous-time higher harmonic controller.

For a single input/single output LTI system, the control u and the output y can be decomposed into their cosine and sine components, and related by the control response matrix $\mathbf{T}$. The control to output relationship which was

$$y(s) = G(s)u(s) \ , \tag{2.6}$$

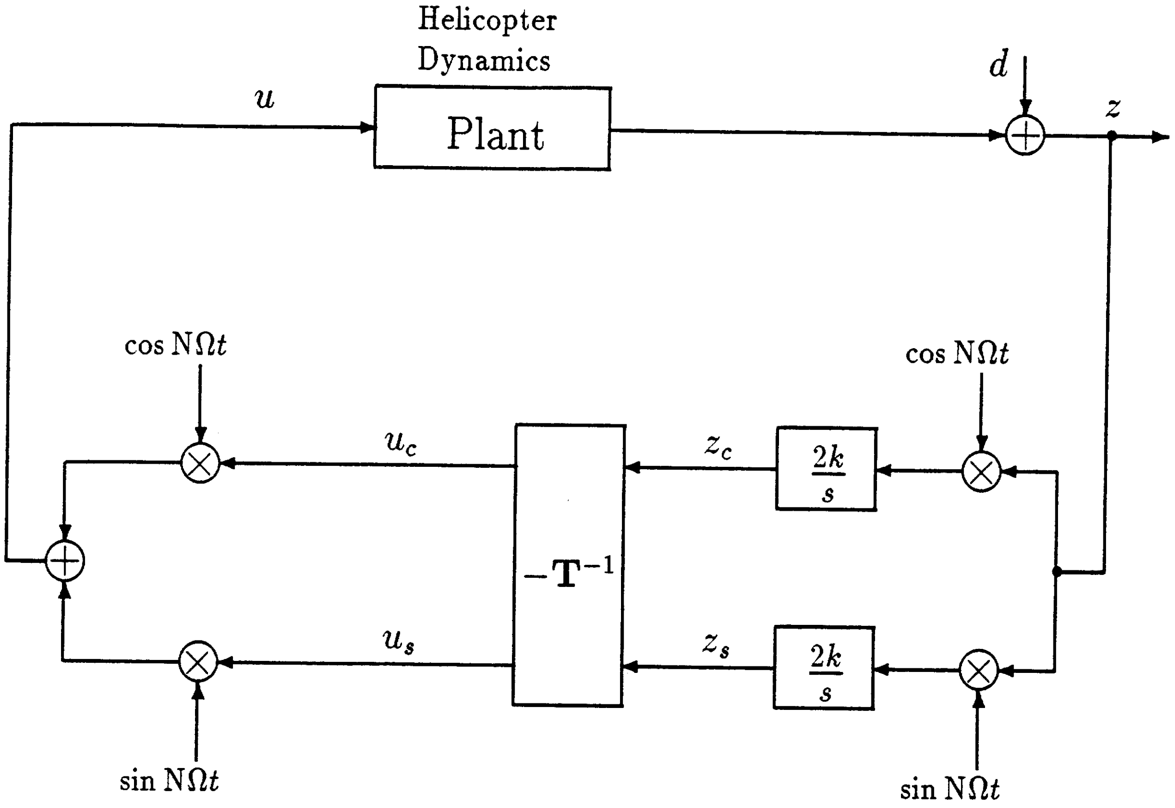

Figure 2-3: Block diagram of the continuous-time HHC algorithm (adapted from Figure 5 of Hall and Wereley [24]).

now becomes

$$\begin{Bmatrix} y_c \\ y_s \end{Bmatrix} = \mathbf{T} \begin{Bmatrix} u_c \\ u_s \end{Bmatrix} .$$

The control response matrix **T** may be written as

$$\mathbf{T} = \begin{bmatrix} T_{cc} & T_{cs} \\ T_{sc} & T_{ss} \end{bmatrix} ,$$

where the elements of the matrix are

$$T_{cc} = \quad T_{ss} = Real\{G(j\mathrm{N}\Omega)\} \tag{2.7}$$

$$T_{cs} = -T_{sc} = Imag\{G(j\mathrm{N}\Omega)\} \ . \tag{2.8}$$

The inverse of the control response matrix may be written as

$$\mathbf{T}^{-1} = \begin{bmatrix} a & b \\ -b & a \end{bmatrix} ,$$

where

$$a = \frac{Real\{G(j\mathrm{N}\Omega)\}}{\mid G(j\mathrm{N}\Omega) \mid^2} \tag{2.9}$$

$$b = -\frac{Imag\{G(j\mathrm{N}\Omega)\}}{\mid G(j\mathrm{N}\Omega) \mid^2} . \tag{2.10}$$

Hall and Wereley have shown that the continuous-time compensator associated with $\mathbf{T}^{-1}$, and the modulation/demodulation structure of Figure 2-3 is

$$H(s) = \frac{2k(as - b\mathrm{N}\Omega)}{s^2 + (\mathrm{N}\Omega)^2} . \tag{2.11}$$

This compensator has the same form as the compensator of equation (2.5), or a narrow band filter centered around $\omega_0 = \mathrm{N}\Omega$. Therefore, the HHC algorithm is analogous to narrow band disturbance rejection in the classical sense. Since the poles of the closed loop system are at $s = -k \pm j\mathrm{N}\Omega$, to first order in k, the gain k determines the exponential decay rate of the system. Since $k = 1/T$, the settling time of the closed loop system is T, so that k plays the same role in the rejection of sinusoidal disturbances as the velocity constant does for constant disturbances. If the settling time of the plant dynamics is not short with respect to T, then closed-loop control may drive the system unstable.

Hall and Wereley modelled the disturbance as a random process with a power spectral density centered about the N/rev frequency. The random nature of the disturbances could be due to the instability of the blade tip vortices, atmospheric turbulence, or the nonlinear dynamic behavior of the rotor. In fact, there is even some evidence of chaotic behavior in helicopter vibrations [60]. With the current approach, quantitative comparisons between different types of HHC algorithms can be made in terms of the RMS vibration levels that remain after closing the loop.

Hall and Wereley used Gauss-Markov disturbance models with a power spectral density of the form

$$S_{\mathrm{dd}}(j\omega) = \frac{\sigma_{\mathrm{d}}^2}{\tau}\left\{\frac{1}{\frac{1}{\tau^2+(\omega+\omega_0)^2}} + \frac{1}{\frac{1}{\tau^2+(\omega-\omega_0)^2}}\right\}, \tag{2.12}$$

and random walk disturbance models with a power spectral density of the form

$$S_{\mathrm{dd}}(j\omega) = \frac{2}{\tau}\frac{(\mathrm{N}\Omega)^2+\omega^2}{\{(\mathrm{N}\Omega)^2-\omega^2\}^2}, \tag{2.13}$$

where τ is the correlation time of the disturbance, and the spectrum is centered about ω_0. The term σ_{d} is the standard deviation of the disturbance. Independent of the form chosen for the spectrum, the ratio of closed-loop to open-loop RMS vibration levels was found to be

$$\frac{\sigma_{\mathrm{z}}}{\sigma_{\mathrm{d}}} \approx \frac{1}{\sqrt{k\tau}} = \sqrt{\frac{T}{\tau}}, \tag{2.14}$$

where σ_{d} is the open-loop RMS vibration level, σ_{z} is the closed-loop RMS vibration level, k is the velocity constant of the HHC control system, and τ is the correlation time of the random disturbance. The vibration attenuation improves as the correlation time or velocity constant increases. Slightly higher vibration levels were calculated for the discrete-time case, where the RMS vibration level asymptotically approaches

$$\frac{\sigma_{\mathrm{z}}}{\sigma_{\mathrm{d}}} \approx \sqrt{\frac{5}{3}}\frac{1}{\sqrt{k\tau}} = \frac{1.291}{\sqrt{k\tau}}. \tag{2.15}$$

The frequency response magnitude for the compensator transfer function, $H(j\omega)$, and the sensitivity transfer function, $S(j\omega)$, of a typical disturbance rejection compensator appear in Figure 2-4, where the compensator is centered around $\omega_0 = 1$. Also, the power spectral density for a Gauss-Markov disturbance, $S_{\mathrm{dd}}(j\omega)$, appears in Figure 2-6, along with the power spectral density of the output $S_{\mathrm{zz}}(j\omega)$. The

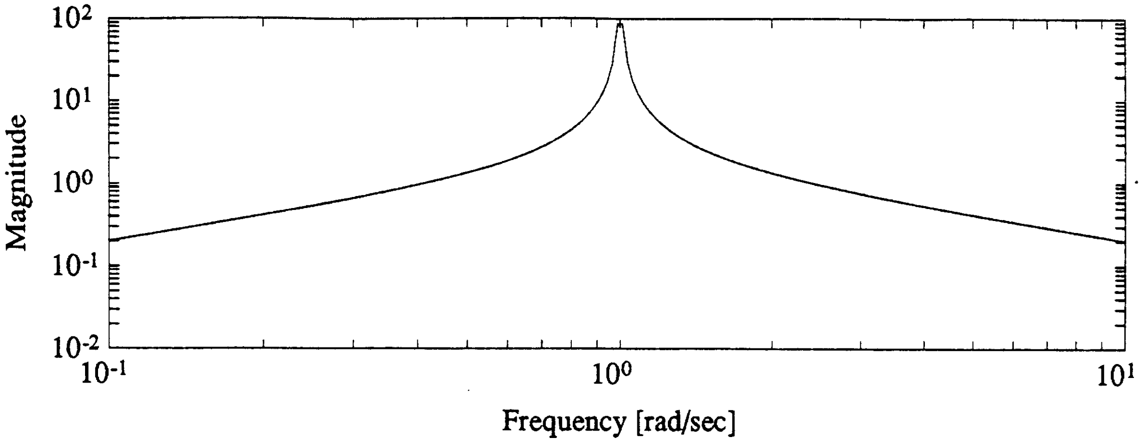

Figure 2-4: Transfer function of a typical HHC compensator H($j\omega$).

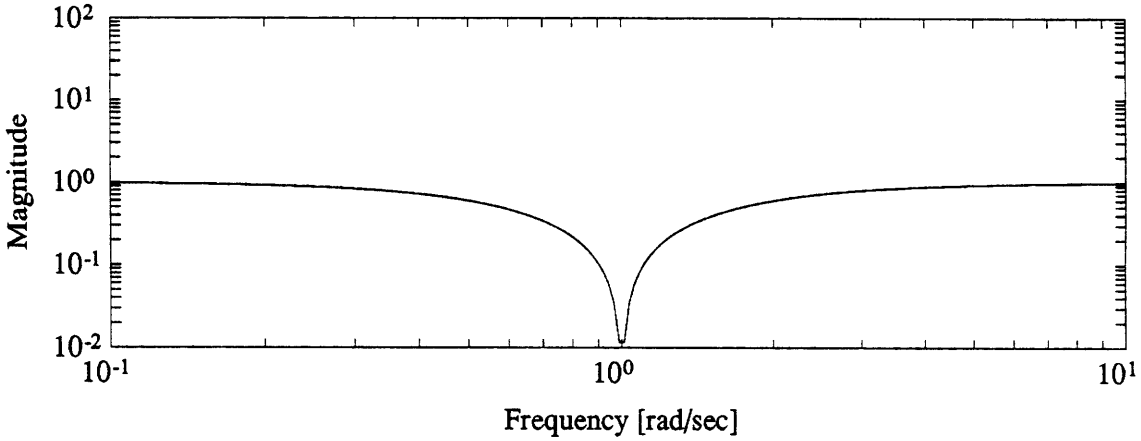

Figure 2-5: Sensitivity transfer function of a typical HHC compensator S($j\omega$).

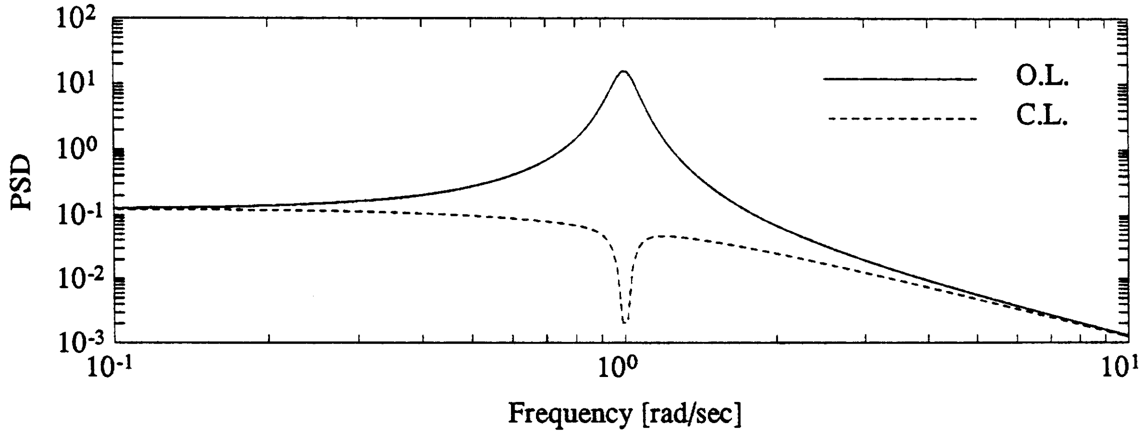

Figure 2-6: Open-loop and closed-loop power spectral densities for a typical HHC compensator in response to a random disturbance.

output power spectral density is related to the disturbance power spectral density by

$$S_{zz}(j\omega) = | S(j\omega) |^2 \, S_{dd}(j\omega) \, , \tag{2.16}$$

so that the compensator eliminates the disturbance centered around $\omega_0 = 1$. Figure 2-6 illustrates an exaggerated case where the correlation time of the disturbance is $\tau = 16T$. In this case, the small correlation time of the disturbance results in a significant spectral width, as evident by the plot. The narrowband filter fails to completely eliminate the disturbance, and a significant amount of power propagates to the output.

The area under the power spectral density curve is the RMS vibration level, and the ratio of closed-loop to open-loop RMS vibration level was given by equation (2.14). For the correlation time $\tau = 16T$, the ratio is 1/4, so that 25% of the RMS vibration level remains. Since the ratio depends upon the square root of $1/k\tau$, it is very sensitive to the magnitude of the correlation time of the disturbance τ, and limits the achievable performance of the HHC controller. So, even if the correlation time is as large as $\tau = 100T$, the closed loop vibration level will be 10% of the open-loop vibration level, resulting in only 90% vibration attenuation.

2.2 Wind Tunnel Tests

Helicopter wind tunnel data was obtained from higher harmonic control tests that Boeing Helicopters concluded in 1985. The investigation is summarized in Reference [63]. The rotor was a 1/6 scale, 10.5 ft diameter, fully articulated, 3-bladed model of the CH-47D Chinook. The model was operated at a tip speed of 731 ft/sec, which required a rotation rate of $\Omega = 22.16$ Hz.

Vibratory rotor loads were measured by a strain gage balance located directly under the rotor hub. This balance measured the rotary hub loads and was not affected by the inertial forces caused by swashplate oscillations. Although the model included a second fixed frame balance, and the blades and pitch links were instrumented,

Table 2.1: Parameters for HHC wind tunnel test (provided by Boeing Helicopters).

Run Number	Flight Speed V [knots]	Shaft Angle α_s [*deg*]	Advance Ratio μ	Blade Loading C_T/σ	Control Law
164.01	135	-5.50	0.310	0.106	open-loop
175.04	100	2.16	0.231	0.122	open-loop
179.03	60	1.06	0.138	0.139	open-loop

only vertical loads at the rotary hub balance were analyzed in this investigation. Channel #3 corresponded to the vertical component of the rotary hub balance, and was labelled “RAFBU1”.

Only baseline runs were analyzed in order to identify the open-loop vibration spectrum. The runs were made at several advance ratios with fairly high blade loading. Table 2.1 gives the parameters for the test runs that were analyzed.

2.3 Data Reduction

The vertical hub force was sampled at 900 μsec, and low-pass filtered to prevent aliasing. The length of the time histories was 1460 samples, resulting in approximately 1.3 sec of data. Since the rotation rate of the rotor was 22–23 Hz, the runs contained slightly more than 29 cycles of data.

The power spectra of the vibrations can be obtained by squaring the magnitude of a Fast Fourier Transform (FFT) of the vibration signals. The FFT is a computationally efficient method of performing a discrete Fourier Transform (DFT), and requires 2^n number of data samples. If the data sequence does not have a power of two length, then the data is padded with zeros in order for it to fulfill this requirement. Although zero padding may be necessary in order to perform a Fast Fourier Transform, it can corrupt the data.

Experimental data is usually windowed, since the discrete Fourier transform assumes a periodic extension of a finite length sequence. The windowing prevents sharp

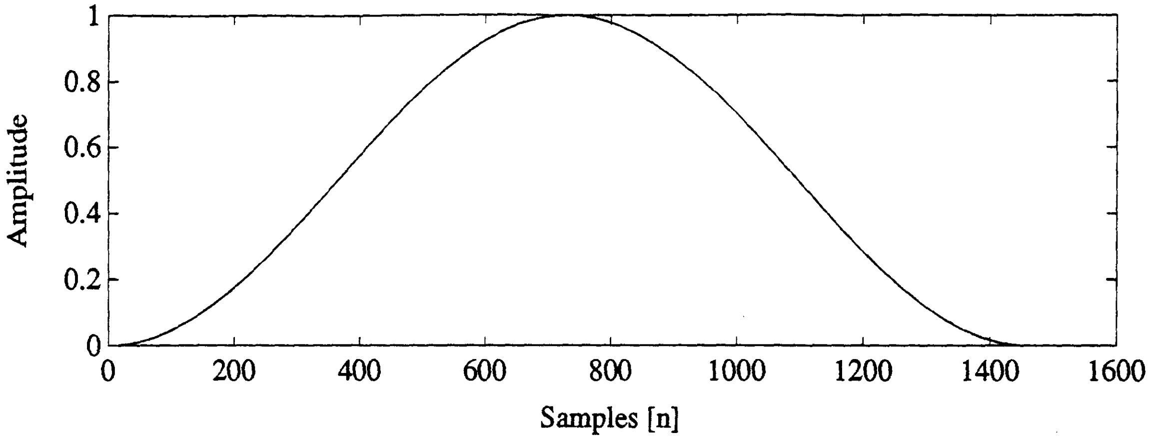

Figure 2-7: Hanning window with 1460 samples).

discontinuities in the time sequence of the data when it is periodically extended, and it tends to smooth the discrete frequency components of the data. A Hanning window weights the data highly near the middle of the sequence and only slightly near the beginning and end of the sequence. Figure 2-7 illustrates a Hanning window which is 1460 samples long, corresponding to the length of the hub force data from the Boeing tests. Figure 2-8 illustrates the discrete time transform of the same Hanning window. Multiplying the sampled data sequence by the Hanning window corresponds to convolving the data spectrum by the discrete frequency spectrum of the Hanning window. From Figure 2-8 we see that the discrete time transform of the Hanning window is 3 samples in width. Therefore, convolving the data by the Hanning spectrum will tend to spread the data spectrum by a couple of samples.

We are primarily interested in the spreading of the helicopter vibration spectrum due to a random disturbance, because the spectral width is related to the correlation time of the disturbance. As mentioned earlier, this correlation time and the controller time response are primarily responsible for determining the limits on vibration attenuation that is achievable using higher harmonic control algorithms. Since it is critical not to corrupt the spectral width of the disturbance, the data was neither windowed nor zero padded.

In order to get an accurate vibration spectrum, a data length corresponding to an integer number of rotor periods was selected, and a DFT was used instead of

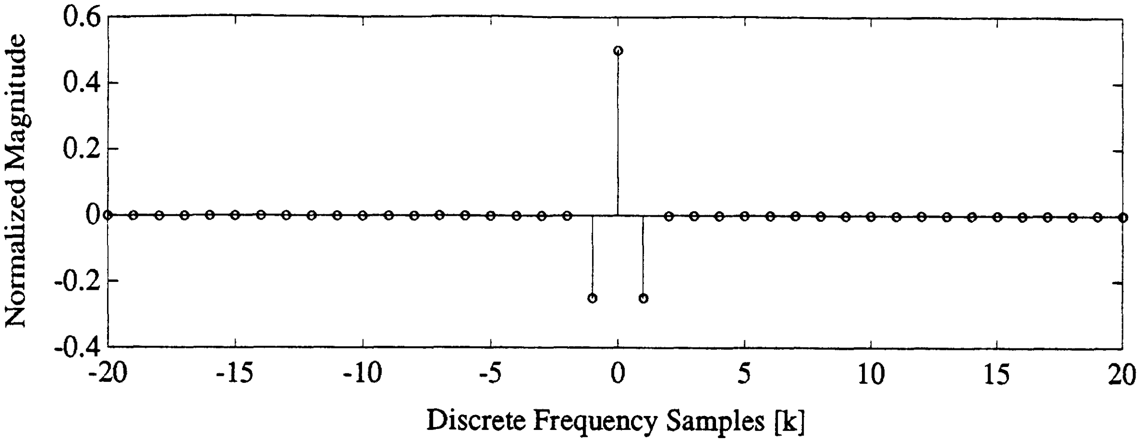

Figure 2-8: Partial discrete frequency transform of the Hanning window with 1460 samples.

an FFT. The exact rotor periods were obtained by examining the output of the instrumented pitch angle of the rotor blade. This signal is was labelled "THETABL," and corresponded to Channel 10 of the Boeing data. Since the rotation rate of the model was observed to vary, each run was analyzed separately. For each run, exactly 29 cycles of data were used; however, the variation in rotation rate resulted in varying data sequence lengths. After the data sequence was truncated to the proper length for 29 cycles of data, any linear trends in the data were removed. The discrete Fourier transform of the resulting sequence was taken, and the magnitude was squared in order to obtain the power spectral density of the hub load vibration.

The power spectral density of the vibration is a useful result, because the area under the power spectral density curve represents the mean square vibration level σ^2, or the energy in the vibration. The square root of this value is the root mean square (RMS) vibration level σ. Since the vertical hub load has units of force, the vertical acceleration levels in g's can be obtained by dividing the RMS vibration level by the gross weight of the helicopter. Only relative values are presented in this study, however, because the units on the vertical hub force signal and the method of calibration were not available.

2.4 Data Analysis

The time history and power spectrum of the vertical hub force for each of the runs listed in Table 2.1, appear in Figures 2-11 to 2-19. The time histories contain approximately 29 cycles of data over a 1.3 sec interval. For Run 164.01, the blade loading was moderate with $C_T/\sigma = 0.106$, but the advance ratio was high at $\mu = 0.310$. Run 175.04 had a higher blade loading with $C_T/\sigma = 0.122$, and a lower advance ratio of $\mu = 0.231$. Finally, Run 179.03 was heavily loaded with $C_T/\sigma = 0.139$, but it had a moderate advance ratio of $\mu = 0.138$. Each of the runs exhibited a large 1/rev vibration component that could have been due to improper blade tracking.

The periodicity of the vibrations is evident by the impulsive nature of the power spectrum plots. Spikes occur in the power spectrum at multiples of the rotation rate, $m\Omega$. Since the rotor speed is approximately 22 Hz, the plots show impulses at approximately 22, 44, 66 Hz, ... In general, the vibrations span only one frequency sample, so that it is difficult to approximate the spectral width of the disturbance. Unfortunately, knowledge of the spectral width is governed by the frequency spacing, and thus the resolution of the discrete Fourier transform. In order to improve our knowledge of the spectrum, a longer time sequence of data is required.

Due to the limitation imposed by the frequency resolution, the correlation time of the disturbance, τ, could not be well approximated. Therefore, the metric proposed by Hall and Wereley in equation (2.14) that provides the ratio of closed-loop to open-loop RMS vibration, could not be used. Instead, another approach was taken in order to analyze this data. A disturbance rejection filter resembling the continuous-time HHC compensator was applied directly to the data, in order to obtain the closed-loop power spectrum from the open-loop spectrum. The ratio of the closed-loop to open-loop power was then computed.

Since the rotor model was 3-bladed, the disturbance rejection filter was centered around the blade passage frequency, 3Ω ($\approx$ 66–69 Hz). The filter had the form

$$H(s) = \frac{2\Omega s}{s^2 + (3\Omega)^2}, \tag{2.17}$$

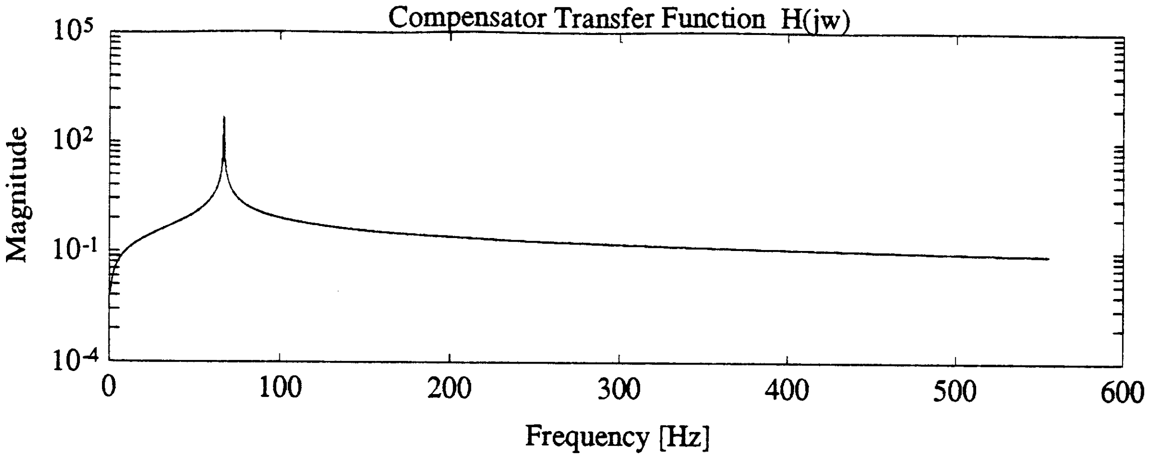

Figure 2-9: HHC filter transfer function H($j\omega$) for 3/rev frequency.

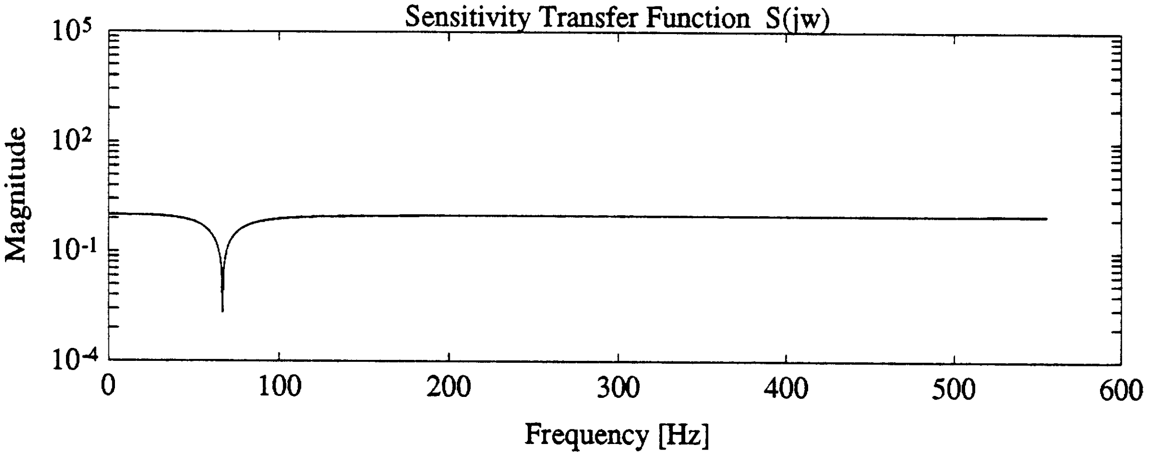

Figure 2-10: HHC filter sensitivity transfer function S($j\omega$) for 3/rev frequency.

which was derived from equation (2.11) with $k = 1/T$, $a = 1$, and $b = 0$. A representative HHC filter transfer function, and the corresponding sensitivity transfer function appear in Figures 2-9 and 2-10 respectively. The actual filters differed for each run to match the rotation rate Ω.

The closed-loop power spectrum was obtained by multiplying the open-loop spectrum by the squared magnitude of the sensitivity transfer function $\mid S(j\omega) \mid^2$ at each frequency, so that

$$S_{zz}(j\omega) = \mid S(j\omega) \mid^2 S_{dd}(j\omega) \; . \tag{2.18}$$

The area under each curve was obtained, with the ratio of the two being σ_z^2/σ_d^2. The square root of this value gives the ratio of closed-loop to open-loop RMS vibration levels, σ_z/σ_d. Since the vibration spectrum contained impulses at nearly all multiples

Table 2.2: Vibration reduction results.

Run Number	Advance Ratio μ	Blade Loading C_T/σ	C.L./O.L. RMS Ratio σ_z/σ_d	Vibration Reduction % RMS
164.01	0.310	0.106	0.287	71.3
175.04	0.231	0.122	0.066	93.4
179.03	0.139	0.139	0.179	82.1

of the rotation rate Ω, but the filter was only applied at the blade passage frequency 3Ω, it was only fair to compare the vibration ratio in that vicinity. The range was taken to be $N\Omega - \Omega/2$ to $N\Omega + \Omega/2$, or 2.5Ω to 3.5Ω . The results for each of the runs is given in Table 2.2.

The runs exhibited 70% to 90% reduction in RMS vibration levels, in general. Incomplete disturbance rejection resulted from the level of wideband noise in the vibration, rather than from the spectral spreading suggested by Hall and Wereley [24]. Although spectral spreading may put limitations on vibration reduction, the level of inherent vibration noise in the system may imply an even greater restriction.

Run 175.04 was the most impulsive at 3/rev, and therefore exhibited the greatest percentage of vibration reduction when the filter was applied. On the other hand, Run 164.01 had only a slight peak, but a significant spectral width at 3/rev, and exhibited the least vibration reduction, as would be expected. Although Run 164.01 exhibited a smaller percentage reduction in RMS vibration level than the other runs, it also had the least open-loop power to begin with. As mentioned in Chapter 1, the percentage of RMS reduction is valuable in terms of comparing HHC controllers, but the final RMS acceleration level is important, because it indicates the ride quality of the helicopter in terms of vibration exposure.

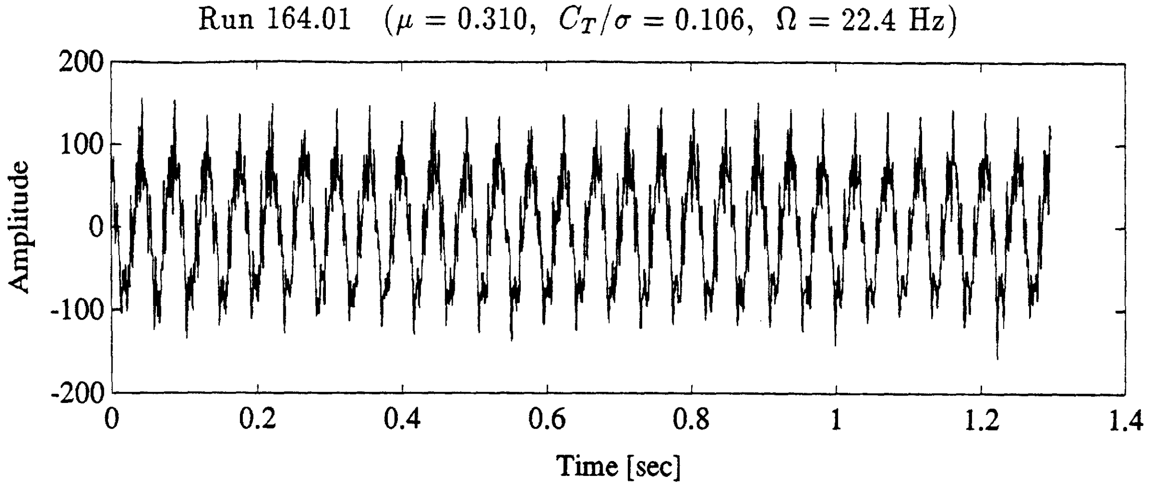

Figure 2-11: Vertical hub force time history for Run 164.01.

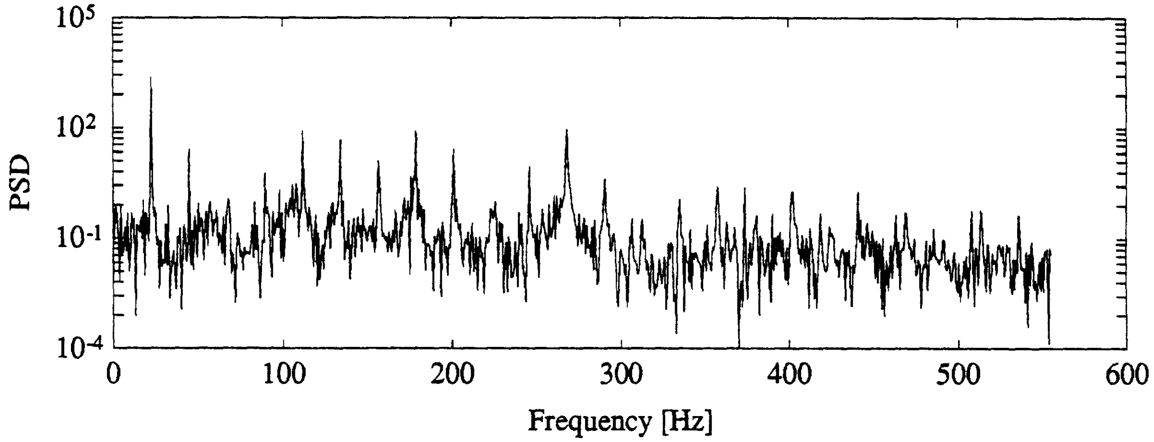

Figure 2-12: Vertical hub force power spectrum for Run 164.01.

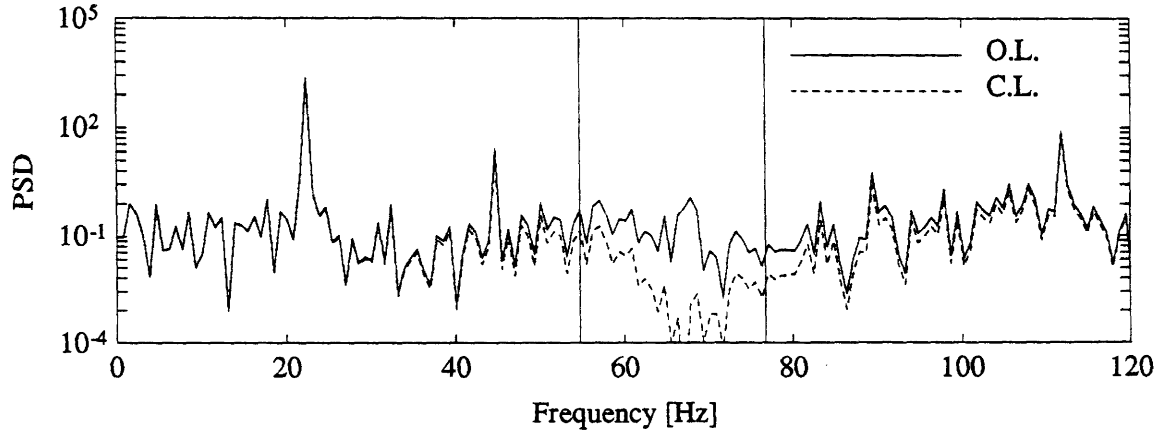

Figure 2-13: Open-loop vs. closed-loop power spectrum for Run 164.01, with 71.3% RMS reduction in the 3/rev range.

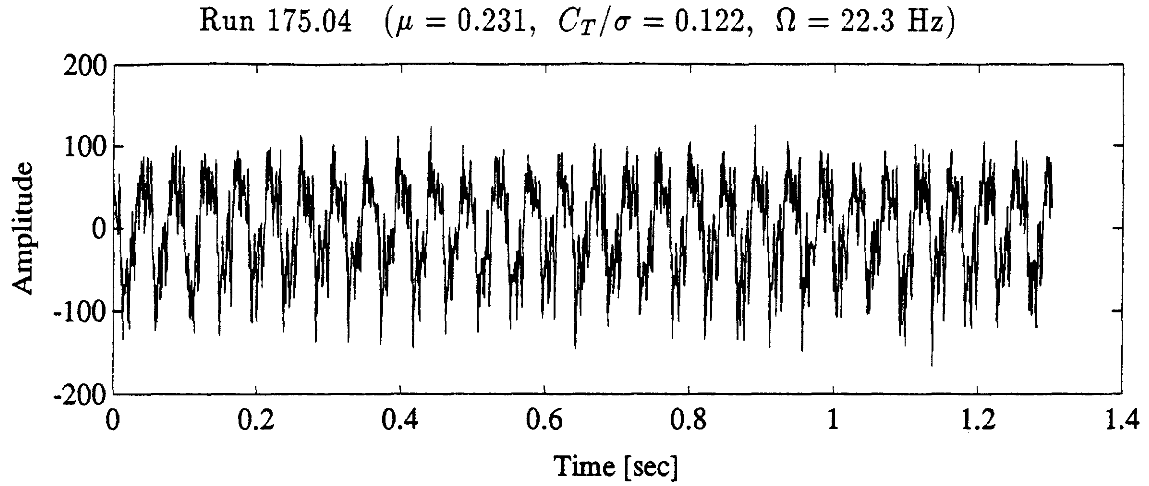

Run 175.04 ($\mu = 0.231$, $C_T/\sigma = 0.122$, $\Omega = 22.3$ Hz)

Figure 2-14: Vertical hub force time history for Run 175.04.

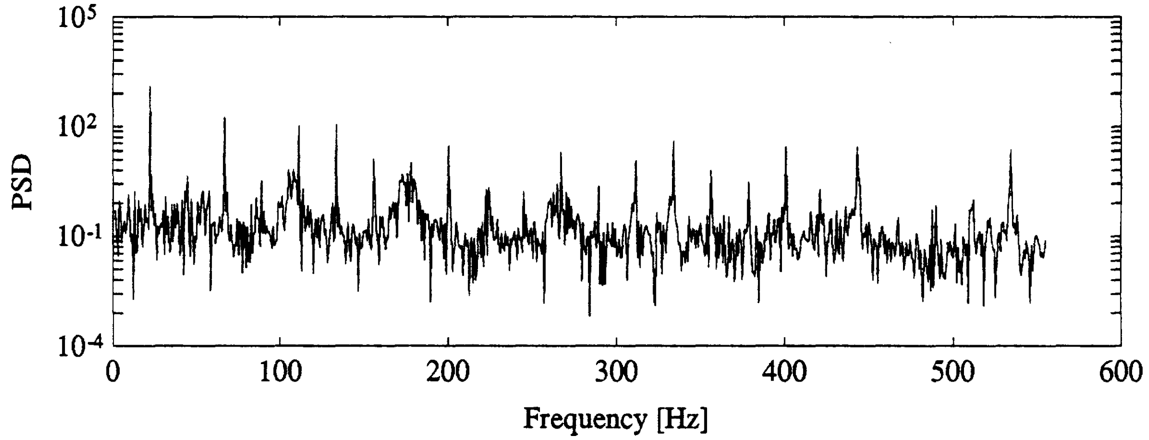

Figure 2-15: Vertical hub force power spectrum for Run 175.04.

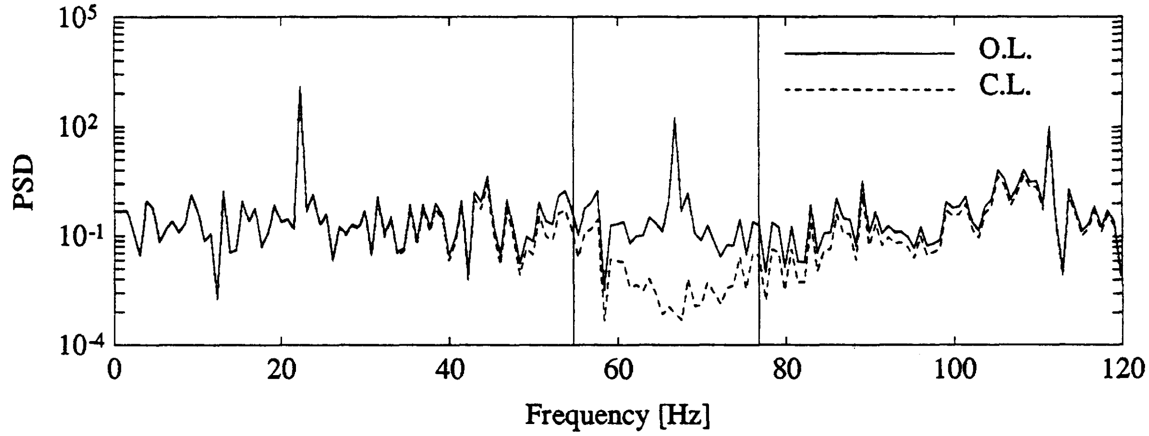

Figure 2-16: Open-loop vs. closed-loop power spectrum for Run 175.04, with 93.4% RMS reduction in the 3/rev range.

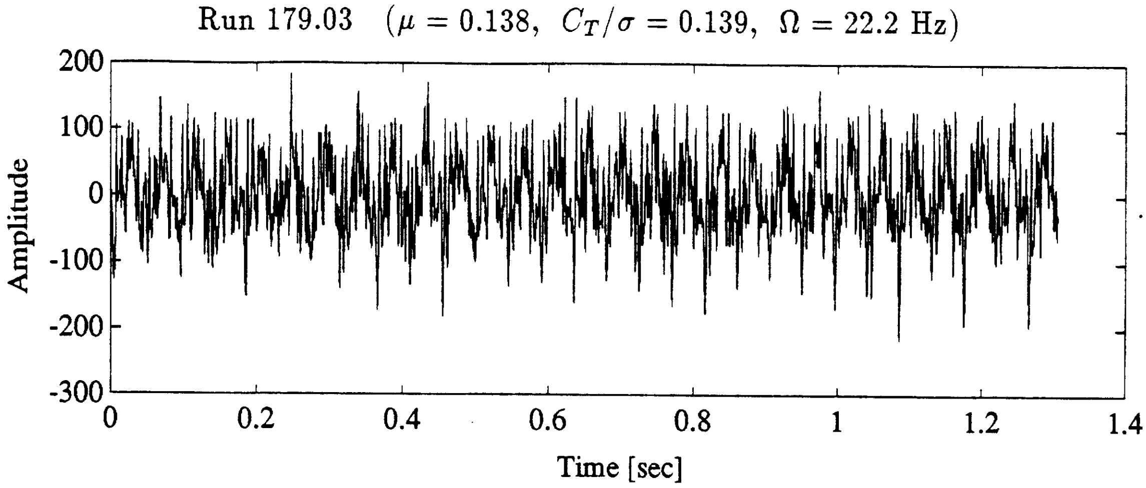

Run 179.03 ($\mu = 0.138$, $C_T/\sigma = 0.139$, $\Omega = 22.2$ Hz)

Figure 2-17: Vertical hub force time history for Run 179.03.

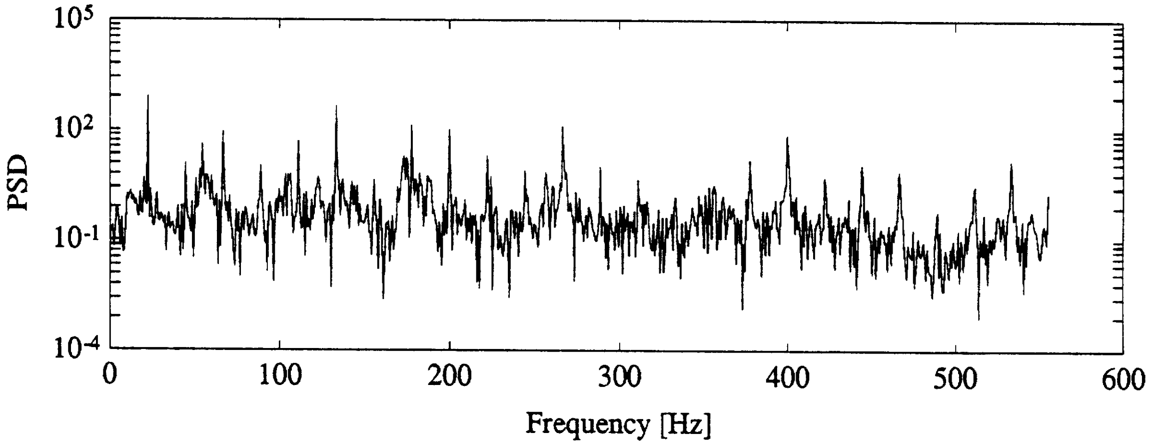

Figure 2-18: Vertical hub force power spectrum for Run 179.03.

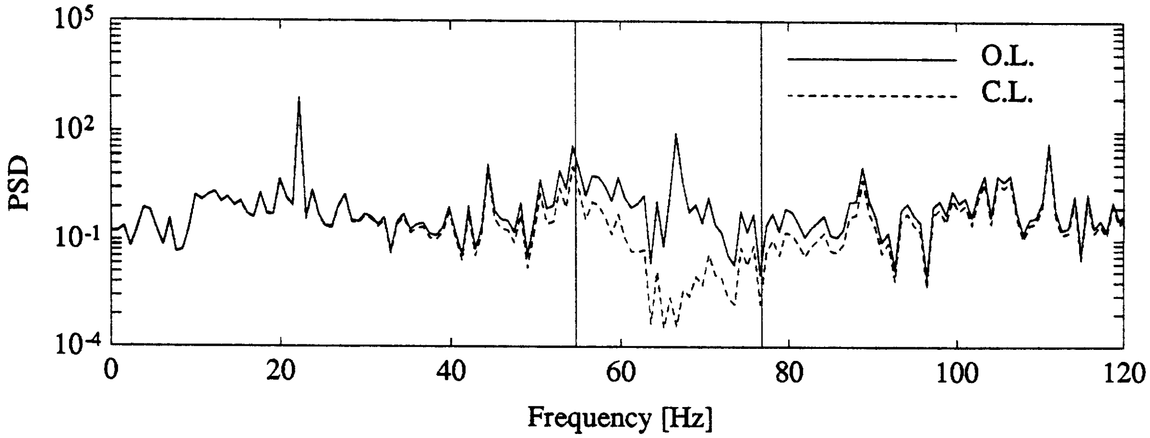

Figure 2-19: Open-loop vs. closed-loop power spectrum for Run 179.03, with 82.1% RMS reduction in the 3/rev range.

Chapter 3

Blade-Mounted Piezoelectric Actuation

Blade-mounted actuation has several advantages over fixed frame actuation. It can provide individual blade control for rotors with any number of blades, the degrees of freedom are not limited by the swashplate system, and a distributed actuation system is possible. This could be essential to simultaneously reducing vibration levels and required power.

Unfortunately, rotating frame actuation poses problems of its own. The actuators will require a relatively high bandwidth for higher harmonic control. Power must be supplied to actuators in the rotating frame, sensor signals may need to return to the fixed frame, and both actuators and sensors will be subjected to centrifugal accelerations on the order of hundreds of g's. Electrohydraulic actuation, by far the most common method for helicopter control, may not be feasible in the rotating frame. Not only will the hydraulic fluid have to be transmitted from the fixed frame to the rotating frame, but centrifugal accelerations will act on the fluid as well. Furthermore, hydraulic actuators have a relatively low bandwidth for a given mass. The inherently massive parts required for electric motors or solenoids may also make them infeasible because of high centrifugal accelerations.

A certain class of materials, known as piezoelectrics, may be well suited for the blade-mounted actuation problem. Piezoelectrics have several advantages over conventional electrohydraulic actuators. They are electrically operated, so that actuation power may be transmitted from the fixed frame to the rotating frame through an electrical slipring. Electrical sliprings tend to be much simpler and more reliable than hydraulic sliprings. In addition, piezoelectric actuators may be segmented to produce distributed lift over the rotor blades. Tailoring the lift distribution of the rotor blades with radius and azimuth may provide significant performance improvement, and segmentation can provide redundancy to the actuation method. Furthermore, piezoelectric actuators are solid state mechanisms, so they are more robust with respect to the large centrifugal loads that are inherent in rotor dynamics. Finally, they have a very high bandwidth, so that multicyclic control for performance improvement and higher harmonic control is possible. In this chapter strain actuation materials and specifically piezoelectric ceramics will be reviewed, and recent experiments involving the application of piezoelectrics for rotor blade actuation will be discussed.

3.1 Strain Actuation Materials

Strain actuation materials can provide a means of controlling structural deformations by regulating the induced strain on the structure. Unlike other actuation methods, strain actuation materials are often bonded or embedded into a structure and may act as an integral part of the structure. They have the advantage of directly influencing the strains, curvatures, and strain energy of the structure.

Structural control can be achieved by changing physical material properties such as size or stiffness, and are commonly regulated either electrically, thermally, or magnetically. Piezoelectrics and electrostrictives have electrically controlled size and stiffness. Thermoelastic or shape-memory alloys are controlled thermally, whereas magnetostrictives are magnetically controlled [3].

By far the most common type of strain actuation material is the piezoelectric. It converts electrical energy to mechanical energy and vice-versa. The electric charge generated is proportional to the imposed stress, and conversely the actuation strain is proportional to the applied electric field. Therefore, piezoelectrics can be used as sensors as well as actuators.

Although less research has been done with electrostrictives and magnetostrictives than piezoelectrics, electrostrictives may lead to more effective actuators [68]. Electrostrictive materials produce a strain proportional to the square of the applied electric field, so they have the potential for very high strains. Unfortunately, they exhibit some undesirable temperature dependent characteristics [11]. Lead magnesium niobate, or PMN, is a commonly used material with electrostrictive properties.

Shape-memory alloys such as Nitinol, a nickel-titanium alloy, have temperature dependent strain characteristics, and can produce very high strains, but are limited in bandwidth. They require heating and cooling to operate, so they can be susceptible to ambient changes, or other thermal intrusions. They may be more appropriate for quasisteady operation, due to limitations in heat dissipation.

3.2 Piezoelectric Theory

Certain natural crystalline structures develop an electric potential when subjected to a mechanical stress. Conversely, the same crystals exhibit a structural deformation when placed in an electric field. The most common of these natural piezoelectric crystals is quartz. The ions of the crystal will displace under the influence of an electric field. Likewise, stressing the material will displace the ions, and produce an electric charge.

Common polycrystalline ceramics may be polarized during manufacture to give them some piezoelectric characteristics of their own. Although the degree of piezoelectricity is not that of natural crystals such as quartz, the abundance of such ceramic materials make them very practical. Polycrystalline ceramics have domains of crystalline nature that are randomly oriented throughout the material. If a strong electric field is applied to the material during manufacture, the individual domains may be reoriented, giving the material a net piezoelectric polarization.

The characteristics of a piezoelectric material can be modeled in several ways, depending on the application at hand. A macromechanical model is most often used when studying the strain induced by the piezoelectric on a structure [3]. It is a simplified linearization of the piezoelectric characteristics, which includes electrical and mechanical relations.

The macromechanical model represents the behavior of a piezoelectric through material variables such as stress T, strain S, electric field E, and electric displacement D. Stress and strain are second order tensors that characterize the elastic behavior of the material, whereas electric field and displacement are first order tensors that characterize the electrical behavior. The electric displacement can be thought of as a directional vector representing the charge density on the material.

For nonpiezoelectric materials stress and strain are often related by an elastic matrix c, or its inverse, the compliance matrix s. The mechanical behavior of a material may be represented as either

$$T = cS \ , \tag{3.1}$$

or

$$S = sT \ . \tag{3.2}$$

The electrical properties of a nonpiezoelectric material may be related by its permittivity matrix ε, or its inverse, the impermittivity matrix β. The electrical behavior may be represented as either

$$D = \varepsilon E \ , \tag{3.3}$$

or

$$E = \beta D \ . \tag{3.4}$$

Piezoelectrics have constants which couple the mechanical and electrical properties of the material. These constants are usually expressed in a matrix form as d, so that the coupled mechanical and electrical material relations are

$$S = s^E T + d_t E \tag{3.5}$$

$$D = dT + \varepsilon^T E \ , \tag{3.6}$$

where the subscript t indicates a transpose. Generally the compliances and permittivities have superscripts that denote the measurement conditions. A superscript T indicates constant or zero stress, S indicates constant strain or a mechanically clamped condition, E indicates constant electric field or a short circuit condition, and D indicates constant electric displacement or an open circuit condition.

A piezoelectric ceramic begins as a completely isotropic material, with randomly oriented crystal domains. In order to pole the ceramic, a strong electric field is applied which reorients the crystal dipoles in a common direction, the poling direction. The material becomes transversely isotropic, with material properties identical in directions perpendicular to the poling direction. Piezoelectrics are ideally transversely isotropic with respect to electrical, mechanical and piezoelectric properties. By convention, the x_3 Cartesian direction denotes the poling direction, so that the material properties are identical in the plane spanned by the x_1 and x_2 directions. Generally, the x_1 and x_2 directions are oriented so that they align with the principal physical axes of the ceramic specimen. A very high electric field is required to pole the ceramic, and this is most easily accomplished through a thin specimen. Therefore, a piezoceramic film or wafer will most likely be poled through the thickness. The transverse isotropy of the material is apparent when equations (3.5) and (3.6) are written explicitly as

$$\begin{bmatrix} S_1 \\ S_2 \\ S_3 \\ S_4 \\ S_5 \\ S_6 \\ \\ D_1 \\ D_2 \\ D_3 \end{bmatrix} = \begin{bmatrix} s_{11}^E & s_{12}^E & s_{13}^E & 0 & 0 & 0 & 0 & 0 & d_{31} \\ s_{12}^E & s_{11}^E & s_{13}^E & 0 & 0 & 0 & 0 & 0 & d_{31} \\ s_{13}^E & s_{13}^E & s_{33}^E & 0 & 0 & 0 & 0 & 0 & d_{33} \\ 0 & 0 & 0 & s_{55}^E & 0 & 0 & 0 & d_{15} & 0 \\ 0 & 0 & 0 & 0 & s_{55}^E & 0 & d_{15} & 0 & 0 \\ 0 & 0 & 0 & 0 & 0 & s_{66}^E & 0 & 0 & 0 \\ \\ 0 & 0 & 0 & 0 & d_{15} & 0 & \varepsilon_1^T & 0 & 0 \\ 0 & 0 & 0 & d_{15} & 0 & 0 & 0 & \varepsilon_1^T & 0 \\ d_{31} & d_{31} & d_{33} & 0 & 0 & 0 & 0 & 0 & \varepsilon_3^T \end{bmatrix} \begin{bmatrix} T_1 \\ T_2 \\ T_3 \\ T_4 \\ T_5 \\ T_6 \\ \\ E_1 \\ E_2 \\ E_3 \end{bmatrix},$$

where the stresses and strains are denoted using matrix notation. Note that for a transversely isotropic material,

$$s_{66} = 2(s_{11} - s_{12}) . \tag{3.7}$$

Therefore, only 10 independent constants are required to characterize the behavior of piezoelectrics (5 compliances, 2 dielectric constants, and 3 piezoelectric coupling terms).

Since the dielectric matrix, ε^T, is diagonal, there is no coupling between dielectric properties in different directions. In addition, piezoceramics exhibit no behavior analogous to shear coupling. Therefore, only three piezoelectric coupling coefficients are required to characterize a piezoelectric ceramic, d_{33}, d_{31}, and d_{15}. By convention, the first subscript of the piezoelectric coefficient denotes the electrical variable, while the second coefficient denotes the mechanical variable. The coefficients are commonly referred to as the longitudinal, transverse, and shear piezoelectric coefficients respectively, because of the strain behavior that they influence. Likewise, the modes of operation are commonly referred to as longitudinal, transverse, and shear.

The method of applying an electric field parallel to the poling direction is often referred to as E_3 *operation*, because the electric field is parallel to the x_3 direction. An E_3 field induces both longitudinal and transverse strain as illustrated in Figure 3-1. The E_3 field will cause the piezoceramic to strain in the x_3 direction, with the strain proportional to d_{33}. If E_3 is in the direction of poling, then the piezoceramic will expand in that direction (the x_3 direction). If E_3 opposes the poling direction, then the piezoceramic will contract in the x_3 direction. This is commonly referred to as longitudinal operation. The strain in the x_3 direction, in the absence of mechanically applied stresses is

$$S_3 = d_{33} E_3 , \tag{3.8}$$

which is positive when E_3 is in the direction of poling.

Transverse operation also uses the E_3 field, but the actuation strain is in the x_1 direction. An E_3 field will create not only a strain in the x_3 direction proportional to d_{33}, but will also create a strain in the x_1 direction proportional to d_{31}. The coefficient

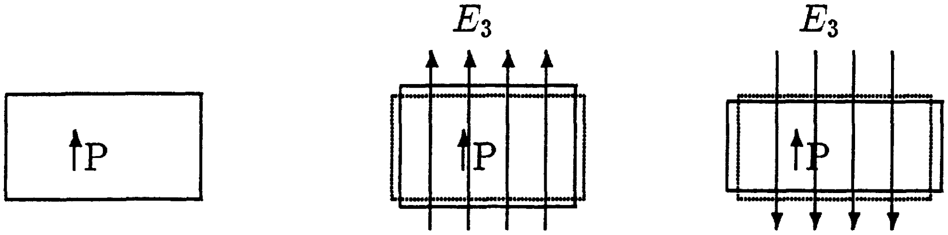

Figure 3-1: Longitudinal/transverse piezoelectric operation.

d_{31} is generally negative, because it arises due to strain in the x_3 direction and the resulting Poisson effect in the x_1 and x_2 directions. The strain in the x_1 direction, in the absence of mechanically applied stresses, is

$$S_1 = d_{31} E_3 \ . \tag{3.9}$$

Longitudinal and transverse operation of a piezoceramic is illustrated in Figure 3-1.

Shear operation makes use of an electric field perpendicular to the poling direction to create a shear strain in the piezoceramic material. The shear mode of operation is illustrated in Figure 3-2. If poling is in the x_3 direction (by convention), then an electric field in the x_1 direction will shear the material proportional to d_{15}. The shear strain is

$$S_5 = d_{15} E_5 \ . \tag{3.10}$$

Although the value of d_{15} is usually greater than d_{33} or d_{31}, the shear mode is seldom used. It is difficult to induce a large net displacement, because very large voltages are required to apply the field.

A strong electric field which opposes the poling direction can degrade the original polarization or even reverse the polarization of a piezoelectric material. The minimum field strength required to depole the piezoceramic is known as the coercive field, E_c. Higher fields may be applied in the poling direction; however, fields several times stronger than E_c in the poling direction can cause electrical breakdown, and

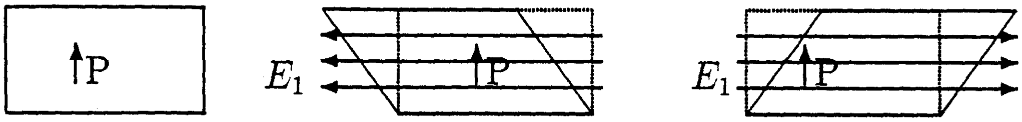

Figure 3-2: Shear piezoelectric operation.

discharge arcing either through the material or around the edges of the piezoceramic. It is common to put a limit on voltage amplifiers that drive piezoelectric devices, so that only a fraction of the coercive field strength can be obtained against the poling direction, while only a fraction of the breakdown field strength can be obtained in the poling direction.

Some of the early applications of piezoelectric ceramics used barium titanate ($BaTiO_3$). In the majority of current applications lead zirconate titanate (PZT) is used. Typical strains for PZT are about 200–300 microstrain. The maximum strain available from a piezoceramic material is limited by the maximum allowable electric field, where the coercive field limits the field that can be applied against the poling direction, and the electrical breakdown field limits the electric field that can be applied in the poling direction.

Piezoceramics can achieve relatively high stresses, but only very small displacements (on the order of microstrain). Increasing the size and thickness of the piezoceramic will increase the total strain displacement, but the voltages required to produce the electric field can quickly become infeasible. However, the displacements can be amplified by using a stack of piezoceramics. A stack can increase the total displacement, without requiring an increase in field strength. The individual piezoceramics retain their original properties, and require the same field strengths as if they were operating independently. Electrodes may be placed between the stacked piezoceramics with adequate insulation, and the system may be wired for either series or parallel

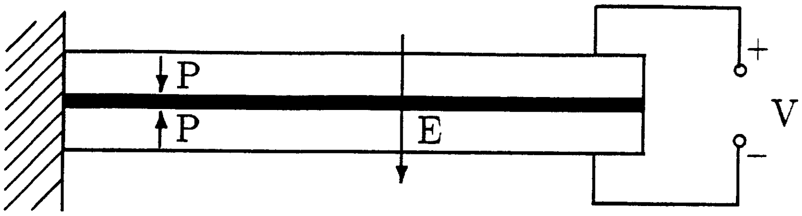

Figure 3-3: Piezoelectric bender wired for series operation.

operation. Piezoceramics stacks can be designed to utilize either the d_{33} or d_{15} effects.

Piezoceramics can also amplify displacement by transforming small strains to relatively large transverse displacements. If piezoceramics are bonded to two surfaces of a thin beam, the d_{31} effect may be utilized to actuate the structure. If one piezoceramic is extended while the other is contracted, bending can be induced in the structure. If the thickness of the beam is made very small, the resulting actuator is called a *bimorph* or a *bender*. Generally, one end of the bender is clamped while the other is used for the actuation displacement. Benders mechanically transform small strains to relatively large transverse displacements.

Benders may be wired for series or parallel operation with a common electrode to apply the voltage. In series operation the common electrode is left electrically floating, while the voltage potential is applied across the electrodes on the exterior piezoceramic surfaces, as in Figure 3-3. In parallel operation the common electrode is grounded, while a positive voltage is applied to both of the exterior electrodes, as in Figure 3-4. (Both configurations have the same maximum field and strain levels, which is determined by the coercive field of the piezoceramic.)

Piezoceramics have a critical temperature, the Curie temperature, above which they completely lose their piezoelectricity. Near the Curie temperature, a piezoceramic will depole with a field much less than the coercive field. Piezoceramics should be operated well below this temperature. The Curie temperature for PZT ceramics is about 360°C (680°F).

Piezoceramic materials are generally very strong in compression, but weak in tension. The tensile strength of PZT is in the range of 21–35 MPa (3000–5000 psi).

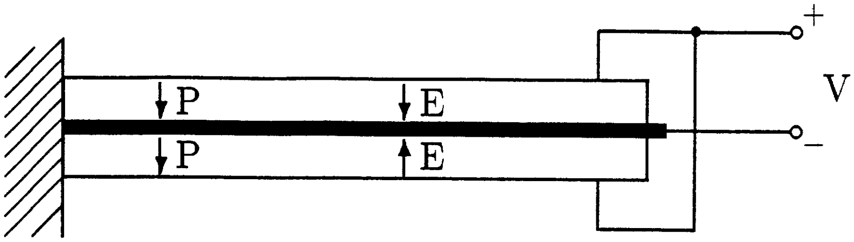

Figure 3-4: Piezoelectric bender wired for parallel operation.

Although stronger in compression, compressive stress levels of 56 MPa (8000 psi) can degrade piezoelectric properties or even depole the material. If a piezoceramic material becomes depoled, it is convenient to have a way of repoling it. This can usually be accomplished by using the same electrodes that are used for actuation. If the piezoceramic is subjected to a field larger than the coercive field (about 1200 V/mm), the field can repole the material.

Although the behavior of piezoceramic materials is approximately linear for small field strains, the assumption that the piezoelectric strain coefficients are constants, can lead to errors in practice. In general, the piezoelectric strain coefficients vary with operating conditions, resulting in nonlinear behavior of the piezoceramic. Commonly encountered nonlinearities include strain rate dependence, hysteresis, and creep [3].

3.3 Piezoelectric Actuation of Rotor Blade Twist

Helicopter rotor control may be achieved by controlling the twist of the rotor blades, as discussed in Section 1.2. Controllable twist rotors have traditionally employed swashplate driven servoflap mechanisms that produce aerodynamic moments that twist the rotor blades. Several methods of active twist control of an airfoil through the use of piezoelectrics will be discussed in this section.

Lazarus and Crawley [10] have used piezoelectric ceramics to induce strain in isotropic and anisotropic plates . Piezoelectric ceramics were attached to a bend/twist or extension/twist coupled composite plates, and piezoelectric strain was used to actuate the plates. When the respective plates were actuated for bending or extension the plates would also twist due to the material coupling, and the angle of attack would change. Lazarus was able to demonstrate closed-loop control of an active twist plate in the wind tunnel [36].

Although this method may prove useful for some airfoil applications, it is probably infeasible for a rotor blade. Since rotor blades tend to be relatively thin airfoils with very high aspect ratios, they are generally rather soft in flapwise bending. For a bend/twist coupled blade, large flapwise bending deflections would introduce large twist deflections as well. In addition, the longitudinal bending of a plate or wing is usually coupled with the transverse bending. Thus, a change in camber usually accompanies bending actuation. The highly coupled torsion, longitudinal, and transverse bending characteristics of such a method makes it undesirable for active blade control. Likewise, large centrifugal accelerations may make extension/twist coupling undesirable.

Barrett [4] developed the concept of directionally attached piezoelectric (DAP) crystals, with the objective of actively and independently changing the bending and twist distributions of a rotor blade. The directionally attached piezoelectric actuators (DAPs) were used to demonstrate active twist and bending of a rotor blade, with ±2 deg of twist achieved, and tip flapping deflections reduced to 1–4% of their original levels.

Directional attachment effectively reduces the transverse stiffness of the actuator element, while maintaining its longitudinal stiffness. In this manner, an isotropic actuator element emulates an anisotropic one, and bending and twist deflections are essentially decoupled. Directional attachment of a piezoelectric can be achieved in three ways: partial attachment; shear lag; or some combination of these two [4]. The partial attachment and transverse shear lag methods are illustrated in Figures 3-5 and 3-6.

Barrett showed that an aluminum beam specimen could be torsionally actuated with directionally attached piezoelectrics, without any bending/twist coupling. Lead

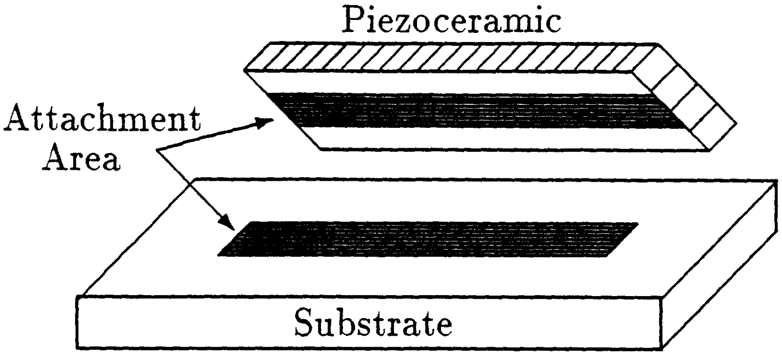

Figure 3-5: Partial attachment of a DAP (adapted from Figure 1 of Barrett [4].)

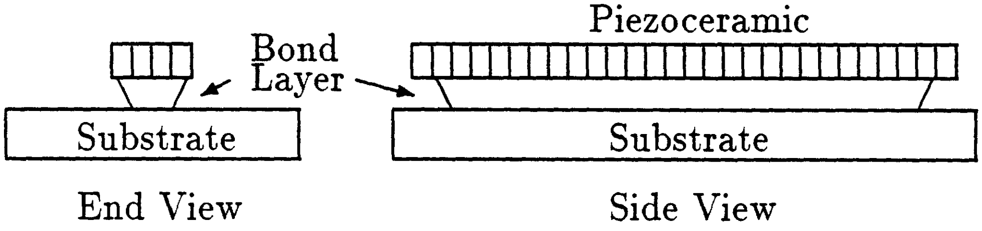

Figure 3-6: Transverse shear lag of a DAP (adapted from Figure 1 of Barrett [4].)

zirconate titanate (PZT) G-1195 was used for the DAPs, while aluminum 2024-T3 was used for the beam. The beam specimen had DAPs attached at 45 deg angles with the length of the specimen on the top and bottom surfaces. An illustration of the beam specimen appears in Figure 3-7. The DAPs on the top were attached at +45 deg, while the ones on the bottom were attached at −45 deg. Simultaneous actuation in extension or contraction produced torsional deflections that were slightly extension/twist coupled. Aligning the DAPs at $[+45/+45]$ deg, rather than at $[+45/-45]$ deg, would have produced a specimen that was bend/twist coupled rather than extension/twist coupled.

Barrett also applied directionally attached piezoactuators to a rotor blade model

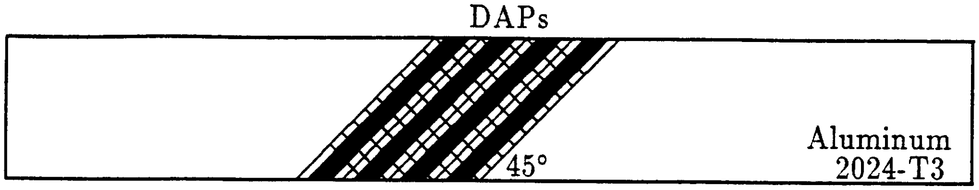

Figure 3-7: DAP beam actuated for twist (adapted from Figure 5 of Barrett [4].)

to actuate it in bending and twist. The blade stiffness target value was that of a 1/8 scale rotor model from the Integrated Technology Rotor (ITR) program [33], and the rotor blade section was modified from a NACA 0012 airfoil section. The airfoil foam core was machined flat from 5% to 30% chord location to accommodate the piezoelectric crystals. The placement of the DAPs to the rotor blade section is illustrated in Figure 3-8. Each side of the blade contained 12 piezoelectric crystal banks of 5 crystals each, and the crystal banks were wired for optimal actuation of the first torsion mode. The flap and torsional stiffnesses were significantly higher than the Froude scaled target values, but the distributed mass and chordwise stiffness were close to the target values.

Vibration testing in flap and torsion was also conducted. The blade exhibited torsional tip deflections as high as ±2.0 deg, for first mode actuation at the resonant frequency. However, the torsional tip deflections were less than ±0.1 deg for static actuation. Flapping vibration suppression was successfully achieved by feeding back an accelerometer signal from the blade tip, to the DAPs. With feedback engaged, the tip deflections were reduced to less than 4% of their original values for the open loop case, for vibration frequencies less than the first flap frequency.

Barrett [4] has shown that directionally attached piezoelectric (DAP) crystals can be used to actuate a rotor blade in twist and bending independently, and that they can be used to suppress some vibrations. DAPs generally cannot induce large twist deflections in rotor blades at low frequencies. Barrett's results show tip twist

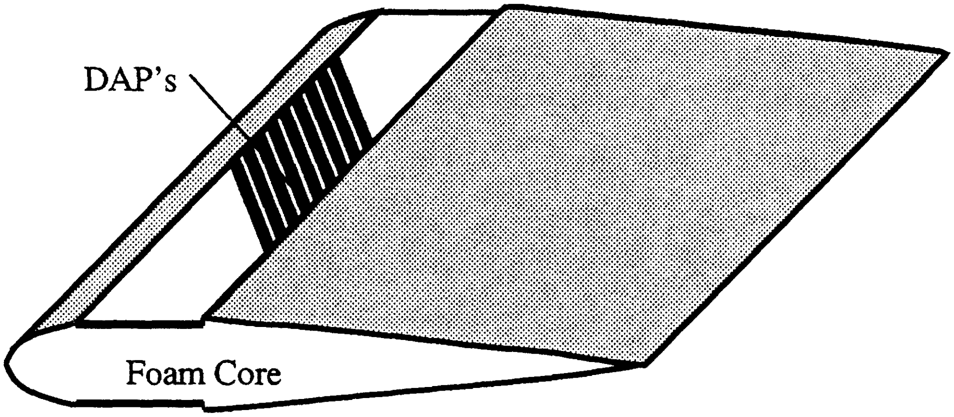

Figure 3-8: DAP rotor blade section (adapted from Figure 9 of Barrett [4].)

responses near the first torsional mode of nearly 2 deg. However, this may be a result of operating near structural resonance, rather than due to the authority of the actuation scheme. In reality, the rotor blade torsional response will be well damped by aerodynamic effects. The N/rev response will probably be on the order of 0.1 deg, depending upon the real aerodynamic damping. Since higher harmonic control will require blade twists more than an order of magnitude higher than this level, DAP actuation for this purpose seems unlikely.

3.4 Piezoelectric Servoflap

Another blade-mounted piezoelectric actuation concept employs piezoceramics to actuate a rotor blade trailing edge flap. Since servoflap controlled blades can require flap deflections up to 10 deg, and piezoceramics are usually small strain, large force devices, mechanical advantage must be used to get larger displacements out of the piezoactuators. Naturally, conservation of energy dictates the trade-off between force and displacement in the piezoceramic. As discussed in Section 3.2, piezoceramic displacements can be amplified by applying them to two surfaces of a thin plate. By

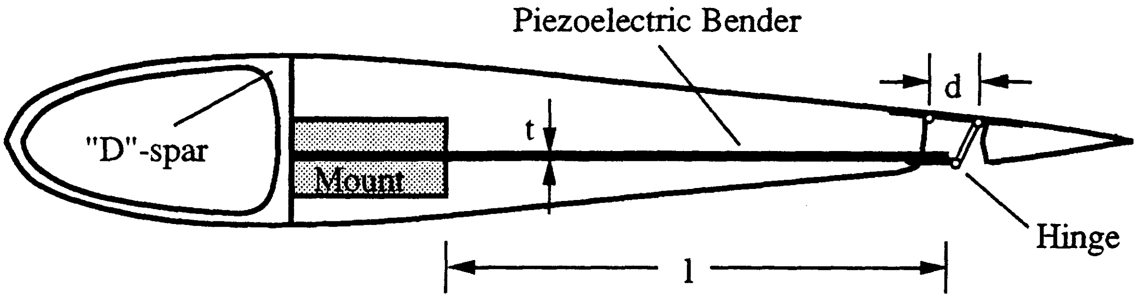

Figure 3-9: Cross section of piezoelectric servoflap mechanism (adapted from Figure 1 of Spangler and Hall [66].)

differentially operating the piezoceramics in extension and contraction, the plate will bend in response to the differential strain induced upon it.

Spangler and Hall [65] have used such a bending device to actuate a rotor blade trailing edge flap. One end of a thin piezoelectric beam was mounted near the spar of the rotor blade section. The other end was attached to a hinge mounted to the servoflap so that a tip deflection, resulting from beam bending, would produce a servoflap deflection. An illustration of the general blade section setup is given in Figure 3-9.

Spangler and Hall [66] developed a 1/5 scale wind tunnel test model based upon the CH-47D rotor blade. The full scale blade has a 2.5 ft chord, and a 30 ft span, with a 12% thick Boeing VR-7 airfoil section, and rotates at 225 rpm. Aeroelastic scaling laws were derived to maintain dynamic similarity between the full scale rotor parameters and the wind tunnel model parameters. The wind tunnel capability and the size of commercially available piezoceramics governed the length scale and velocity scale respectively. The length and velocity scales were $L = 1/5$ and $U = 1/10$ respectively.

The piezoceramic material that was used was lead zirconate titanate (PZT) type G-1195, and it was determined that a maximum strain of 150 microstrain could be obtained with this material. The piezoceramic bender length was constrained to the length of the semichord, due to the geometric constraints of the airfoil. The actual airfoil test section had a span of one foot, so that seven 1.5 inch wide piezoceramics could be used to actuate the trailing edge flap. The piezoceramic benders were 1.5 in × 2.5 in × 0.021 in. The design velocity was the 1/10 scaled tip speed of the full scale rotor, or 70.8 ft/s. Spangler and Hall [66] found that optimum efficiency is obtained when the moment arm length d is chosen to impedance match the piezoceramic energy with the work done on the airstream. The scale values resulted in an optimal moment arm length of $d = 0.085$ in.

The airfoil section was rigidly mounted to the wind tunnel at the 1/4 chord, so that the only degree of freedom was the flap angle, η. Near the design flight speed a peak-to-peak flap angle of 12 deg was attainable for the design field at 4 Hz. The 4 Hz frequency corresponds to the N/rev frequency, which is 11.25 Hz in the full scale. Spangler and Hall [66] have shown through energy arguments that the desired deflections could be achieved in the full scale with piezoceramics that are several times thicker than current off-the-shelf sizes.

Lift and moment coefficients were measured for a tunnel velocity near the design point speed, for various electric field strengths. At 4 Hz, the peak-to-peak change in lift coefficient due to the flap angle was about 0.10, while the peak-to-peak change in moment coefficient was about -0.06. These results were much lower than values derived from theory, and the deficiency was believed to have been the result of a sizeable boundary layer due to low Reynolds number flow.

Piezoelectric servoflap actuation has been demonstrated on a wind tunnel model and seems potentially feasible in the full scale. Since relatively high flap response amplitudes can be achieved, independent of the structure's dynamic properties (i.e. structural resonance is not required to achieve high amplitudes), the actuation method should work for real flight conditions. Flap deflections on the order of 10 deg should be attainable in full scale. Advances in piezoceramic materials could provide even greater performance.

Although piezoelectric actuation of a servoflap is potentially feasible, the ability of such an actuation method to achieve higher harmonic vibration control must be determined. An analytical rotor model will be derived in Chapter 4 that will include the effect of a servoflap, so that transfer functions from servoflap inputs to hub loads can be calculated to determine the feasibility of servoflap actuation for HHC. Based on the results of Spangler and Hall [66], servoflap deflections up to 10 deg will be assumed to be obtainable using piezoelectric actuation.

Chapter 4

State Space Rotor Model Derivation

In this Chapter, a state space model of rotor dynamics is derived, so that transfer functions from control inputs to hub loads can be obtained. Since we are interested in piezoelectric servoflap actuation, the effect of a servoflap will be included in this model. The transfer functions from servoflap inputs to hub loads will be used to determine the ability of a servoflap mechanism to provide higher harmonic control. In addition, the amount of servoflap deflection required for HHC can be determined, which will have implications on the piezoelectric actuation of these devices. Finally, the continuous transfer functions obtained from this model should provide valuable insight into the design of control systems for higher harmonic vibration suppression.

The equations of motion governing the structural dynamics of the rotor blade can be derived independently of the aerodynamics which force the system. This will be done in order to simplify the derivation. Multiblade coordinates can be used to describe the degrees of freedom of the rotor, and represent modes of the rotor disk. They provide a convenient description of the rotor motion and steady hub loads, in the fixed frame. The model will be expressed in state space form so that the transfer functions may be easily calculated, and linear control techniques may be applied.

For simplicity, the rotor will be articulated, with rigid blade flapping, but no blade bending. The mathematical derivation will be general enough that any number of torsional modes may be included, but one or two modes should be sufficient. Linear aerodynamics will also be assumed so that the blade motions and rotor inflow will appear as perturbations in angle of attack. In addition, the simple inflow model developed by Pitt and Peters [53] will be used.

4.1 Multiblade Coordinates

In this Section, the mathematics required to develop the rotor equations of motion are described, especially those associated with the transformation between the rotating and fixed reference frames. In particular, multiblade coordinates are used to represent the blade deflections. One of the difficulties in deriving the transfer functions of a rotor from swashplate (or servoflap) inputs, which are in the fixed frame, to acceleration or force is that the rotor, where all the forces are generated, is rotating. Therefore, the equations of motion in general are time-varying. Since transfer functions exist only for linear time-invariant systems, this implies that rotors should not have a transfer function. It turns out, however, that the response of a rotor is time-invariant, or nearly so, especially for a rotor with a large number of blades. In this context, "large" may mean four or even three blades. Multiblade coordinates are particularly useful for describing the dynamics of the rotor in this case, because the resulting blade degrees of freedom are in the fixed frame.

Helicopter blade dynamics can be expressed either in the fixed (vehicle) frame, or in the rotating (rotor) frame. In some respects, it is easier to derive the blade equations of motion in rotating frame, because the aerodynamic forces are more easily represented there. However, because vehicle loads, swashplate control inputs, and wind gusts are all represented in the fixed frame, it is helpful to represent the rotor dynamics and hub loads in terms of the fixed frame as well. Therefore, a transformation from the rotating frame to the fixed frame is required.

To begin, each blade is given an integer index, q. The blade index is in the range $1 \leq q \leq \mathrm{N}$, and the reference blade has the index $q = 1$. The azimuthal location of any blade may be written as

$$\psi_q = \psi + (q-1)\frac{2\pi}{\mathrm{N}}, \tag{4.1}$$

where ψ is the azimuth of the reference blade. Figure 4-1 illustrates the rotor blade azimuth angle ψ, with respect to the forward flight velocity of the helicopter. If nondimensional time is used, then

$$\psi_q = \bar{t} + (q-1)\Delta\bar{t}, \tag{4.2}$$

where $\Delta\bar{t} = \Delta\psi = 2\pi/\mathrm{N}$, the azimuthal spacing between blades. The rotor period is $T = 2\pi/\Omega$, or in nondimensional time $\overline{T} = 2\pi$. The blade passage period is $T_\mathrm{b} = 2\pi/\mathrm{N}\Omega$, or $\overline{T}_\mathrm{b} = 2\pi/\mathrm{N}$.

The equations of motion of a single blade can be derived in the rotating frame, and expressed as a function of azimuth ψ. If ψ_q is substituted for ψ, then the equations can represent the motion of several identical blades. The coefficients in the equations of motion may be expressed in terms of multiblade coordinates, and products of sines or cosines can be expanded to the sum of sines and cosines by equations (4.13)—(4.15). Groups of terms containing the factors 1, $\cos(\psi)$, $\sin(\psi)$, ... may be collected and individually set equal to zero, to give N equations of motion for the fixed frame harmonics, for each equation of motion of the rotor blade. The fixed frame equations of motion expressed in multiblade coordinates will represent the modal dynamics of a rotor disk containing N blades.

Fourier series may be used to represent the blade motions, if they are assumed to be periodic. Any periodic function, such as the blade flap angle $\beta(\psi)$, has a fundamental dimensionless period of 2π, and may be represented as a linear combination of cosine and sine functions with the same fundamental period. For example, β may be written as

$$\beta(\psi) = \beta_0 + \beta_{1c}\cos(\psi) + \beta_{1s}\sin(\psi) + \beta_{2c}\cos(2\psi) + \beta_{2s}\sin(2\psi) + \dots\,. \tag{4.3}$$

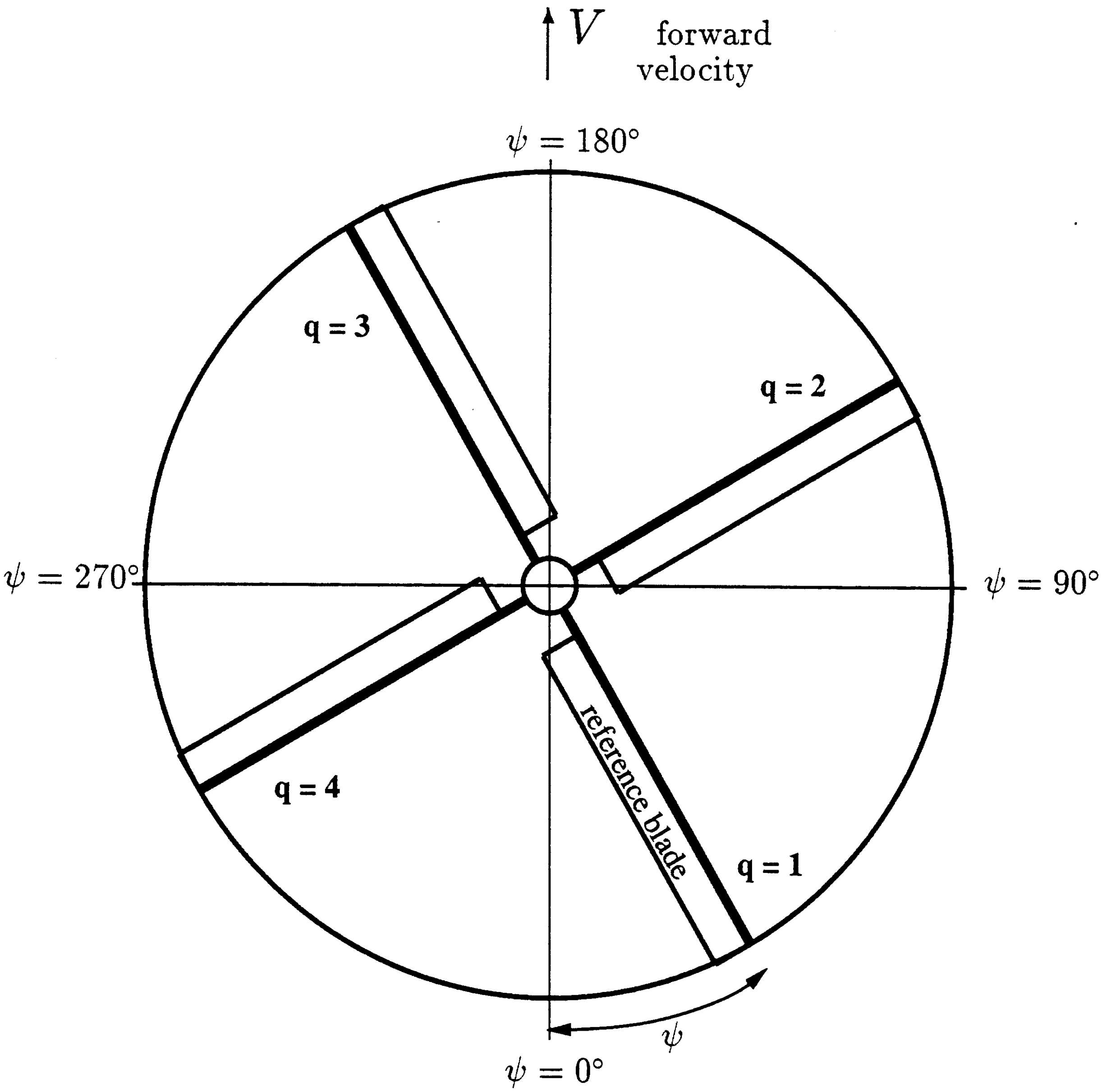

Figure 4-1: Rotor blade azimuth angle ψ, and blade indices.

The Fourier coefficients may be evaluated from integrals of $\beta(\psi)$ as

$$\beta_0 = \frac{1}{2\pi} \int_0^{2\pi} \beta(\psi) d\psi \; , \tag{4.4}$$

$$\beta_{nc} = \frac{1}{\pi} \int_0^{2\pi} \beta(\psi) \cos(n\psi) d\psi \; , \tag{4.5}$$

$$\beta_{ns} = \frac{1}{\pi} \int_0^{2\pi} \beta(\psi) \sin(n\psi) d\psi \; . \tag{4.6}$$

The Fourier series linearly transforms a continuous periodic function $\beta(\psi)$, to an infinite set of constant coefficients (β_0, β_{1C}, β_{1S}, β_{2C}, β_{2S}, ...). Generally, only the lowest few harmonics have significant magnitude, so that the continuous function may be described by a small set of Fourier coefficients.

The discrete Fourier series (DFS) is similar to the continuous Fourier series, except that the discrete Fourier series fits a periodic function at several discrete points, and therefore requires a finite set of coefficients. For the helicopter rotor, these points are the azimuthal blade locations. Multiblade coordinates use the N lowest Fourier coefficients to transform rotor blade degrees of freedom in the rotating frame, to rotor disk degrees of freedom in the fixed frame. The total number of degrees of freedom are maintained, because there is a degree of freedom for each of the N blades and multiblade coordinates use N Fourier coefficients to represent the rotor disk. For example, the flap angles of the rotor blades are β_1, β_2, $\ldots\beta_{\mathrm{N}}$. The blade angles get transformed by the discrete Fourier series to the fixed frame coefficients β_0, $\beta_{1\mathrm{c}}$, $\beta_{1\mathrm{s}}$, $\ldots\beta_{\mathrm{d}}$, which represent flapping modes of the rotor disk. The fixed frame coefficients are

$$\beta_0 = \frac{1}{\mathrm{N}} \sum_{q=1}^{\mathrm{N}} \beta(\psi_q) \ , \tag{4.7}$$

$$\beta_{n\mathrm{c}} = \frac{2}{\mathrm{N}} \sum_{q=1}^{\mathrm{N}} \beta(\psi_q) \cos(n\psi_q) \ , \tag{4.8}$$

$$\beta_{n\mathrm{s}} = \frac{2}{\mathrm{N}} \sum_{q=1}^{\mathrm{N}} \beta(\psi_q) \sin(n\psi_q) \ , \tag{4.9}$$

$$\beta_{\mathrm{d}} = \frac{1}{\mathrm{N}} \sum_{q=1}^{\mathrm{N}} \beta(\psi_q)(-1)^q \ . \tag{4.10}$$

The coefficients β_0, β_{nc}, β_{ns}, and β_{d} are the multiblade coordinates. Note that the differential term β_{d} only exists when there is an even number of blades. So for a 4-bladed rotor,

$$\beta_q = \beta_0 + \beta_{1\mathrm{c}} \cos(\psi_q) + \beta_{1\mathrm{s}} \sin(\psi_q) + \beta_{\mathrm{d}}(-1)^q \ , \tag{4.11}$$

whereas for a 5-bladed rotor,

$$\beta_q = \beta_0 + \beta_{1c}\cos(\psi_q) + \beta_{1s}\sin(\psi_q) + \beta_{2c}\cos(\psi_q) + \beta_{2s}\sin(\psi_q)\ . \tag{4.12}$$

The coefficient β_0 is the coning degree of freedom, and β_{1c}, and β_{1s} are the longitudinal and lateral tip-path-plane-tilt degrees of freedom, respectively. The remaining degrees of freedom are reactionless modes, since they involve no net force or moment on the rotor hub.

The equations of motion governing rotor blade dynamics inherently include terms that contain the product of trigonometric functions. The following rules can be helpful in expanding the product of sines and cosines, to the sum of sines and cosines:

$$\cos(a\psi)\cos(b\psi) = \frac{1}{2}\cos((a+b)\psi) + \frac{1}{2}\cos((a-b)\psi)\ , \tag{4.13}$$

$$\sin(a\psi)\cos(b\psi) = \frac{1}{2}\sin((a+b)\psi) + \frac{1}{2}\sin((a-b)\psi)\ , \tag{4.14}$$

$$\sin(a\psi)\sin(b\psi) = \frac{1}{2}\cos((a-b)\psi) - \frac{1}{2}\cos((a+b)\psi)\ . \tag{4.15}$$

In order to determine hub reaction loads, the force contributed by each blade must be included. This implies that the equations of motion for the rotor disk include the summation of trigonometric terms of the form

$$\frac{1}{\mathrm{N}}\sum_{q=1}^{\mathrm{N}}\cos(n\psi_q) = \delta_{n,\mathrm{N}}\cos(n\psi)\ , \tag{4.16}$$

and

$$\frac{1}{\mathrm{N}}\sum_{q=1}^{\mathrm{N}}\sin(n\psi_q) = \delta_{n,\mathrm{N}}\sin(n\psi)\ . \tag{4.17}$$

With this notation, $\delta_{n,\mathrm{N}} = 1$ if n is an integer multiple of the number of blades N, and $\delta_{n,\mathrm{N}} = 0$ otherwise.

A rotor with an even number of blades will include differential modes containing the factor $(-1)^q$ [34, pg. 358], and summations similar to those of equations (4.16) and (4.17) are generally required. For the purpose of this research, however, we will retain only the first three multiblade coordinates, β_0, β_c, and β_s. Therefore, the summations that include differential terms will not be necessary. The multiblade coordinate expansion of the flapping angle will be limited to

$$\beta(\psi) = \beta_0 + \beta_c \cos\psi + \beta_s \sin\psi \ , \tag{4.18}$$

with only the first three terms are retained. This is a reasonable approximation if the rotor has three or more blades. The dynamics of the hovering rotor become time-invariant, and higher coefficients produce reactionless terms which contribute no net force or moment on the rotor hub.

The blade section airloads are proportional $(\overline{r} + \mu \sin\psi)^2$, and will discussed in Section 4.5. In forward flight these airloads are cyclic, and will modulate the N/rev terms. If the rotor has four or more blades this effect will still produce nearly time-invariant dynamics. If the rotor has three blades, the N/rev terms that influence the steady hub loads are proportional to $\frac{1}{4}\mu^2$. Since the advance ratio is on the order of $\mu = .1$, the effects are very small and can be neglected. Therefore, the three degree of freedom multiblade coordinate representation is reasonable, and produces nearly time-invariant dynamics even in forward flight. The approximation is valid for rotors with three or more blades, and improves with increasing blade number and decreasing advance ratio.

With the three degree of freedom multiblade coordinate approximation, all inputs, outputs, and state variables will contain terms with factors 1, $\cos\psi$, and $\sin\psi$. Therefore, the rotor controls will be in terms of collective and cyclic inputs. The hub load outputs will be the thrust, pitch moment, and roll moment, and any internal state variables will have collective and cyclic components. For example, the flapping angle β will be in terms of the coning angle (β_0), longitudinal tip-path-plane-tilt (β_c), and the lateral tip-path-plane-tilt (β_s). Summation operators will be used to transform generalized forces on the blades to forces on the rotor disk modes. The operators are

$$(\cdot)_0 = \frac{1}{N}\sum_{q=1}^{N}(\cdot) \ , \tag{4.19}$$

$$(\cdot)_c = \frac{2}{\mathrm{N}} \sum_{q=1}^{\mathrm{N}} (\cdot) \cos(\psi_q) \ , \tag{4.20}$$

$$(\cdot)_s = \frac{2}{\mathrm{N}} \sum_{q=1}^{\mathrm{N}} (\cdot) \sin(\psi_q) \ . \tag{4.21}$$

In summary, several assumptions have been made that will lead to simple, linear time-invariant (LTI) rotor dynamics, which will be expressed in a constant coefficient state space model. The blade dynamics are periodic with a nondimensional period of 2π. The blades are identical, so that the nondimensional blade passage period is $2\pi/\mathrm{N}$. Only the first three multiblade coordinates will be retained, since they dominate the response. Finally, the rotor will be assumed to have three or more blades so that the dynamics and airloads are nearly time-invariant.

In the remainder of this Chapter the equations of motion of the rotor blade will be derived. The degrees of freedom will be transformed to multiblade coordinates in order to describe the dynamics of the rotor disk modes. Finally, the equations of motion will be formulated in state space matrix form.

4.2 Rotor Model Characteristics

The rotor model has been developed in terms of nondimensional quantities, so that general rotor configurations can be analyzed without the need to specify dimensions. The rotor properties have been normalized by the rotor radius R, the rotor speed Ω, and density of air ρ where appropriate. Relevant rotor properties include the geometry of the blade and servoflap, blade inertias and stiffnesses, and the lift and moment coefficients for the rotor blade and servoflap.

The rotor blade was assumed to have constant structural and aerodynamic properties along its span in order to simplify the solution. This assumption gives orthogonal natural mode solutions. Since they are uncorrelated, the modal dynamics are uncoupled and a relatively simple model results. This assumption is not essential to the model. The rotor blade properties can vary with span, or even be lumped if one is willing to do more work. However, constant blade properties should be sufficient in

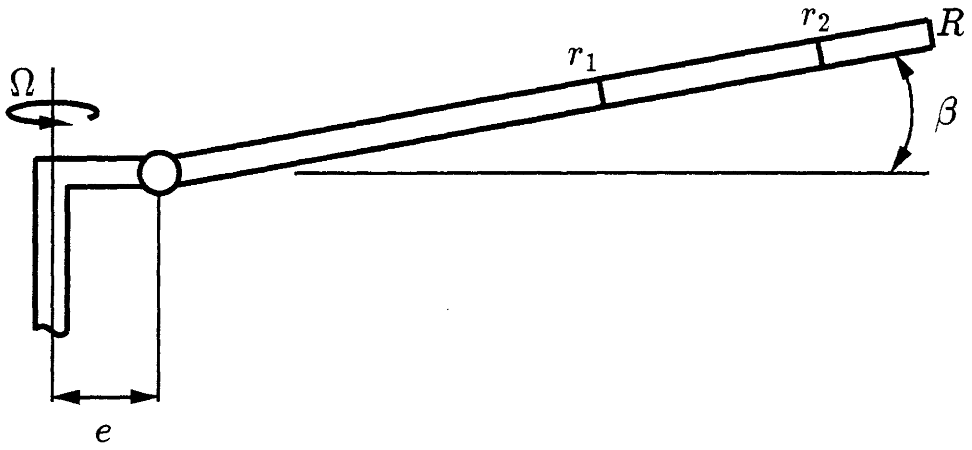

Figure 4-2: Rotor blade geometry (side view).

order to determine the feasibility of the servoflap concept, and will simplify the model as well as the analysis.

The important parameters required in order to specify the geometry of the rotor are the chord length (c), and the flapping hinge offset (e). The servoflap spans the inboard radial location $r = r_1$ to the outboard radial location $r = r_2$. The geometry of the rotor blade is illustrated in Figure 4-2. Each of these lengths may be normalized by the rotor radius R, to give $\bar{c}$, $\bar{e}$, $\bar{r}_1$, and $\bar{r}_2$.

The mass and stiffness of the blade are not explicitly required, rather they are implicitly derived from the flapping inertia I_β, the pitch inertia I_θ, and the first torsional frequency of the rotor blade. To nondimensionalize the inertias, we define the characteristic inertia of the rotor blade

$$I_\mathrm{b} = \int_e^R mr^2 dr \ , \tag{4.22}$$

where m is the sectional mass of the blade. The flapping inertia I_β, and the torsional modal inertias I_{θ_k} are nondimensionalized by I_b, so that $I_\beta^* = I_\beta / I_\mathrm{b}$, and $I_{\theta_k}^* = I_{\theta_k} / I_\mathrm{b}$. The inertia I_b is also used to define the Lock number, the nondimensional parameter that relates aerodynamic to inertial forces. The Lock number is

$$\gamma = \frac{\rho a c R^4}{I_\mathrm{b}} . \tag{4.23}$$

Nondimensional time was used, where $\bar{t} = \Omega t = \psi$. Therefore, frequencies are normalized by the rotor speed Ω. For example, the nondimensional first torsional frequency of the rotor blade is $\overline{\omega}_1 = \omega_1/\Omega$, while the flapping frequency of the rotor blade is $\overline{\nu}_\beta = \nu_\beta/\Omega$.

The center of gravity (C.G.), aerodynamic center (A.C.), and elastic axis (E.A.) were assumed to coincide with the pitch axis of the blade at the 1/4 chord, to further simplify the model. This implies that the *in vacuo* flapping and torsion of the blade are uncoupled, because the center of gravity and elastic axis are coincident. Furthermore, the lift force will not twist the blade, because the aerodynamic center and elastic axis coincide. In addition, a symmetric airfoil section was assumed, which exhibits no aerodynamic moment about its 1/4 chord.

Although blade sectional lift is generally a complicated function of angle of attack, Mach number, and Reynolds number, a linear approximation can be made that characterizes the lift curve on the outboard region of the blade, where most of the lift occurs. Sectional blade lift was assumed to be proportional to the angle of attack of the blade α, with a constant lift curve slope $c_{l_\alpha} = a$. Linear approximations were also made for the increment in lift and moment about the 1/4 chord, due to the servoflap. The increment in lift is proportional to the servoflap angle η, and a constant lift curve slope $c_{l_\eta} = n$. The moment is proportional to η, and the constant $c_{m_\eta} = p$. The aerodynamic properties of the rotor blade and servoflap are determined exclusively by the constants a, n, and p .

The blade degrees of freedom are the flapping angle β, and the torsional modal coordinates θ_k, where k is the mode number. The moments were nondimensionalized by $I_\mathrm{b}\Omega^2$, so that the nondimensional flapping and twist moments are

$$\overline{M}_\mathrm{F} = \frac{M_\mathrm{F}}{I_\mathrm{b}\Omega^2} , \tag{4.24}$$

and

$$\overline{N} = \frac{N}{I_b \Omega^2} , \tag{4.25}$$

respectively. The inputs to the model are the root pitch angle θ_r, and the servoflap angle η. Finally, the outputs of interest are the thrust, pitch, and roll coefficients, which are C_T, C_M, and C_L, respectively.

4.3 Blade Torsional Modal Analysis

The derivation of the aeroelastic equations of motion for the helicopter rotor can be broken down into two parts, the *in vacuo* blade dynamics, and the aerodynamics. The *in vacuo* blade dynamics include only inertial and elastic effects, with the rotor effectively operating in a vacuum. The aerodynamics of the rotor can be formulated independently, and treated as functions which force the blade dynamics. The homogeneous solution of the partial differential equation which governs the free torsional motion of the rotor blade corresponds to the *in vacuo* solution and will be derived in this Section. The aerodynamics that force the structural response will be formulated separately in Section 4.5.

The partial differential equation that governs the free torsional motion of the rotor blade is

$$I_\theta \frac{\partial^2 \theta}{\partial t^2} - GJ \frac{\partial^2 \theta}{\partial r^2} = 0 , \tag{4.26}$$

where θ is the pitch angle of the rotor blade section, I_θ is the sectional moment of inertia about the pitch axis, and GJ is the torsional stiffness of the section. The moment of inertia I_θ and the torsional stiffness GJ are assumed to be constant along the length of the span for simplicity, although this assumption is easily relaxed. A logical trial solution for the elastic twist of the blade is one that separates variables, such as

$$\theta_{\mathrm{tw}}(r,t) = \xi_\theta(r) \sin(\omega t) , \tag{4.27}$$

where θ_{tw} is the elastic twist of the rotor blade. This solution may be substituted into the governing differential equation to give

$$-\omega^2\xi_\theta(r) - \left(\frac{GJ}{I_\theta}\right)\frac{\partial^2\xi_\theta(r)}{\partial r^2} = 0\ . \tag{4.28}$$

Since the rotor has a hinge offset of length e, the blade is torsionally clamped at the root $r = e$, while it is free at the tip $r = R$. The boundary conditions are

$$\theta_{\text{tw}}(r,t)\big|_{r=e} = 0\ , \tag{4.29}$$

and

$$GJ\frac{\partial\theta_{\text{tw}}(r,t)}{\partial r}\bigg|_{r=R} = 0\ . \tag{4.30}$$

So the elastic twist is zero at the blade root, while the moment is zero at the blade tip. In order to satisfy these boundary conditions the mode shape $\xi_\theta(r)$ must have the form

$$\xi_{\theta_k}(r) = \sin\left(\frac{\pi(2k-1)}{2(R-e)}(r-e)\right)\ , \tag{4.31}$$

or if written in terms of the normalized radius $\overline{r}$,

$$\xi_{\theta_k}(\overline{r}) = \sin\left(\frac{\pi(2k-1)}{2(1-\overline{e})}(\overline{r}-\overline{e})\right)\ . \tag{4.32}$$

The corresponding modal frequencies are

$$\omega_k = \frac{\pi(2k-1)}{2(1-\overline{e})}\sqrt{\frac{GJ}{I_\theta R^2}}\ . \tag{4.33}$$

The rotor model is derived so that full blade feathering by root pitch actuation or controllable twist through servoflap actuation can be investigated. The pitch of the rotor blade includes the contribution of feathering as well as elastic deformation, and can be expressed as a combination of the two. The structural response will be that of a system with moving supports [46, pg. 299], where full feathering of the rotor blade may excite the elastic twist modes of the blade. The torsion equations may be solved by assuming that the pitch of the blade is a linear combination of a rigid-body translation θ_{r}, and the elastic deformation θ_{tw}, so that

$$\theta(r,t) = \theta_{\mathrm{r}}(t) + \theta_{\mathrm{tw}}(r,t)\,. \tag{4.34}$$

Substitution of $\theta(r,t)$ into the governing differential equation (4.26) yields

$$I_\theta \frac{\partial^2 \theta_{\mathrm{r}}}{\partial t^2} + I_\theta \frac{\partial^2 \theta_{\mathrm{tw}}}{\partial t^2} - GJ \frac{\partial^2 \theta_{\mathrm{tw}}}{\partial r^2} = 0\,. \tag{4.35}$$

The moment due to rigid-body inertia may be brought to the right hand side of the equation, where it appears as a forcing, so that

$$I_\theta \frac{\partial^2 \theta_{\mathrm{tw}}}{\partial t^2} - GJ \frac{\partial^2 \theta_{\mathrm{tw}}}{\partial r^2} = N\,. \tag{4.36}$$

In general, the torsional moment N will depend on aerodynamic forces as well as inertial forces, so that

$$N = N_{\ddot{\theta}_r} + N_{\mathrm{aero}}\,, \tag{4.37}$$

where N_{aero} is due to aerodynamic forces, and the inertial force is

$$N_{\ddot{\theta}_r} = -I_\theta \ddot{\theta}_{\mathrm{r}}\,. \tag{4.38}$$

The partial differential equation (4.36) may be decomposed into modal coordinates by integrating each term in the equation over the mode shape. A single differential equation for each mode k may be obtained, in terms of the k th modal mass, stiffness, and force which are

$$I_{\theta_k} = \int_e^R \xi_{\theta_k}(r) I_\theta \xi_{\theta_j}(r)\,dr\,, \tag{4.39}$$

$$K_{\theta_k} = \int_e^R \xi_{\theta_k}(r) GJ \frac{\partial^2 \xi_{\theta_j}(r)}{\partial r^2}\,dr\,, \tag{4.40}$$

$$N_k = \int_e^R \xi_{\theta_k}(r) N\,dr\,, \tag{4.41}$$

respectively. If the mode shapes are not orthogonal (which is generally the case for an assumed mode solution), then the dynamics will be expressed by a coupled matrix differential equation. Cross coupling terms of the form

$$I_{\theta_{kj}} = \int_e^R \xi_{\theta_k}(r) I_\theta \xi_{\theta_j}(r) dr \ , \tag{4.42}$$

$$K_{\theta_{kj}} = \int_e^R \xi_{\theta_k}(r) GJ \frac{\partial^2 \xi_{\theta_j}(r)}{\partial r^2} dr \ , \tag{4.43}$$

will be required for the mass and stiffness matrices, respectively.

The kth modal frequency is ω_k, where $\omega_k = \sqrt{K_{\theta_k}/I_{\theta_k}}$. Therefore, the kth torsional modal mass and stiffness for the rotor blade are

$$I_{\theta_k} = \frac{(1-\bar{e})}{2} I_\theta \ , \tag{4.44}$$

and

$$K_{\theta_k} = (2k-1)^2 \frac{\pi^2}{8(1-\bar{e})} GJ \ , \tag{4.45}$$

respectively. For the remainder of this derivation the torsional dynamics will be formulated in a general manner, so that any number of torsional modes may be included in the model. The first torsional frequency of rotor blades are typically 3Ω–6Ω, which places the second torsional frequency at 9Ω–18Ω. Since we will generally be dealing with rotors that have 3–5 blades, and the $N\Omega$ responses are of interest for higher harmonic control, the first torsional mode should dominate the response at $N\Omega$. Therefore, the inclusion of one or two torsional modes should be sufficient for this model.

4.4 *In Vacuo* Blade Dynamics

The *in vacuo* blade dynamics contain only inertial and elastic effects, and will be derived in this Section. The aerodynamics force the structural response of the rotor and are formulated in Section 4.5. Once the blade equations of motion are derived, they will be transformed into multiblade coordinates so that they represent the dynamics of several rotor disk modes.

Although an arbitrary number of torsional modes may be included in the model, rigid blade flapping without blade bending was assumed. Flapwise bending could be included in the model, but the effects are expected to be minor for an articulated rotor. The effect of gravity on the blade dynamics was also neglected, because the centrifugal accelerations governing the blade motions are higher than gravitational accelerations by several orders of magnitude.

In the remainder of this report, the elastic twist coordinates will be expressed as θ_k, in order to simplify the notation. The mode number can take on integer values $k = 1, 2, \ldots$, and an expression that includes the mode number k implies a summation over the number of modes used in the model.

The method of Lagrange was used to obtain the equations of motion of the rotor blade [46, pg. 47], which follows directly from energy arguments. The kinetic and potential energies of the rotor blade are given by

$$T^* = \frac{1}{2}I_\beta\dot{\beta}^2 + \frac{1}{2}I_z\Omega^2 + \frac{1}{2}I_{\theta_k}\dot{\theta}_k^2 \tag{4.46}$$

and

$$V = \frac{1}{2}K_\beta\beta^2 + \frac{1}{2}K_{\theta_k}\theta_k^2 \ , \tag{4.47}$$

respectively, where the general form of the torsional mode has been used. The Lagrangian is

$$\begin{aligned} L &= T^* - V & (4.48)\\ &= \frac{1}{2}I_\beta\dot{\beta}^2 + \frac{1}{2}I_z\Omega^2 - \frac{1}{2}K_\beta\beta^2 + \frac{1}{2}I_{\theta_k}\dot{\theta}_k^2 - \frac{1}{2}K_{\theta_k}\theta_k^2 \ . & (4.49)\end{aligned}$$

The blade moment of inertia about the flapping hinge, I_β, is given by

$$I_\beta = \int_e^R m(r-e)^2 dr \ , \tag{4.50}$$

and can be substituted into the Lagrangian of equation (4.49). The blade moment of inertia about the rotor shaft, I_z, is given by

$$I_z = \int_e^R m\,(e + (r - e)\cos(\beta))^2\,dr\ , \tag{4.51}$$

and can also be substituted into the Lagrangian. For small angles, a second order approximation may be used, so that $\cos\beta \approx (1 - \beta^2/2)$ and $\cos^2\beta \approx (1 - \beta^2)$. Since constant energy terms in the Lagrange expression may be ignored, and the rotation rate Ω is constant, only varying terms of I_z need to be retained. The blade moment of inertia about the rotor shaft I_z may be rewritten as

$$I_z = \text{const} - \beta^2 \left[I_\beta + \int_e^R me(r - e)dr \right]\ , \tag{4.52}$$

where the constant term may be ignored. Since there are no energy terms in the Lagrangian that contain both β and θ_k, the equations of motion for the flapping and twisting of the blade will be uncoupled. Lagrange equations may be written for the blade generalized coordinates Ξ_j, where Ξ_j includes β and θ_k . If the generalized forces are Θ_j, then the Lagrange equations may be written as

$$\frac{d}{dt}\left(\frac{\partial L}{\partial \dot{\Xi}_j}\right) - \frac{\partial L}{\partial \Xi_j} = \Theta_j\ . \tag{4.53}$$

The generalized forces are the flap moment M_F, and the twist moment N due to aerodynamic and control forces on the blade. The Lagrange equations for the twist and flapping dynamics of the rotor blade may be independently written as

$$I_{\theta_k}\ddot{\theta}_k + K_{\theta_k}\theta_k = N_k\ , \tag{4.54}$$

and

$$I_\beta\ddot{\beta} + \left(I_\beta\Omega^2 + K_\beta + \Omega^2 \int_e^R me(r - e)dr \right)\beta = M_F\ , \tag{4.55}$$

respectively. When time is nondimensionalized by the rotor speed, so that $\bar{t} = \Omega t$, then equations (4.55) and (4.54) may be divided by $I_b\Omega^2$ to give the nondimensional equations of motion

$$I^*_{\theta_k}\ddot{\theta}_k + I^*_{\theta_k}\overline{\omega}_k^2\theta_k = \frac{N_k}{I_b\Omega^2}\ , \tag{4.56}$$

and

$$I^*_\beta\ddot{\beta} + I^*_\beta\overline{\nu}_\beta^2\beta = \frac{M_F}{I_b\Omega^2}\ . \tag{4.57}$$

The term $\overline{\omega}_k$ is the nondimensional torsional frequency of the kth mode, given by

$$\overline{\omega}_k = \sqrt{\frac{K_{\theta_k}}{\Omega^2 I_{\theta_k}}}\ . \tag{4.58}$$

The term $\overline{\nu}_\beta$ is the nondimensional flapping frequency, which is obtained from

$$\overline{\nu}_\beta^2 = 1 + \frac{K_\beta}{\Omega^2 I_\beta} + \frac{\int_e^R me(r-e)dr}{I_\beta}\ . \tag{4.59}$$

Note that centrifugal forces contribute a restoring force to the blade flapping motion. Without a flapping spring K_β or a flap hinge offset e, the blade will flap at the rotor speed Ω. However, the presence of either a flapping spring or a hinge offset will increase the flapping frequency.

The equations of motion that represent the dynamics of the rotor disk may be derived by following the method outlined in Section 4.1 . The flapping angle β and its first two time derivatives with respect to $\bar{t}$, can be written in terms of multiblade coordinates as

$$\beta = \beta_0 + \beta_c \cos\psi + \beta_s \sin\psi\ , \tag{4.60}$$

$$\dot{\beta} = \dot{\beta}_0 + \dot{\beta}_c \cos\psi + \dot{\beta}_s \sin\psi - \beta_c \sin\psi + \beta_s \cos\psi\ , \tag{4.61}$$

$$\ddot{\beta} = \ddot{\beta}_0 + \ddot{\beta}_c \cos\psi + \ddot{\beta}_s \sin\psi - 2\dot{\beta}_c \sin\psi + 2\dot{\beta}_s \cos\psi - \beta_c \cos\psi - \beta_s \sin\psi\ . \tag{4.62}$$

The kth torsional modal coordinate and its derivatives can also be written in multiblade coordinates as

$$\theta_k = \theta_{k,0} + \theta_{k,c} \cos\psi + \theta_{k,s} \sin\psi\ , \tag{4.63}$$

$$\dot{\theta}_k = \dot{\theta}_{k,0} + \dot{\theta}_{k,c} \cos\psi + \dot{\theta}_{k,s} \sin\psi - \theta_{k,c} \sin\psi + \theta_{k,s} \cos\psi\ , \tag{4.64}$$

$$\ddot{\theta}_k = \ddot{\theta}_{k,0} + \ddot{\theta}_{k,\mathrm{c}} \cos\psi + \ddot{\theta}_{k,\mathrm{s}} \sin\psi - 2\dot{\theta}_{k,\mathrm{c}} \sin\psi + 2\dot{\theta}_{k,\mathrm{s}} \cos\psi - \theta_{k,\mathrm{c}} \cos\psi$$
$$- \theta_{k,\mathrm{s}} \sin\psi \ . \tag{4.65}$$

If the degrees of freedom in the flapping and pitch equations of motion are expressed in terms of multiblade coordinates, and the collective and cyclic summation operators $(\cdot)_0$, $(\cdot)_\mathrm{c}$, and $(\cdot)_\mathrm{s}$, of equations (4.19)—(4.21) are applied to the blade equations of motion, then the equations of motion for collective and cyclic rotor disk modes can be obtained. The equations of motion for the flapping and twist motion of the rotor disk in multiblade coordinates are

$$I_\beta^* \begin{bmatrix} 1 & & \\ & 1 & \\ & & 1 \end{bmatrix} \begin{Bmatrix} \ddot{\beta}_0 \\ \ddot{\beta}_\mathrm{c} \\ \ddot{\beta}_\mathrm{s} \end{Bmatrix} + I_\beta^* \begin{bmatrix} 0 & 0 & 0 \\ 0 & 0 & 2 \\ 0 & -2 & 0 \end{bmatrix} \begin{Bmatrix} \dot{\beta}_0 \\ \dot{\beta}_\mathrm{c} \\ \dot{\beta}_\mathrm{s} \end{Bmatrix}$$
$$+ I_\beta^* \begin{bmatrix} \overline{\nu}_\beta^2 & & \\ & (\overline{\nu}_\beta^2 - 1) & \\ & & (\overline{\nu}_\beta^2 - 1) \end{bmatrix} \begin{Bmatrix} \beta_0 \\ \beta_\mathrm{c} \\ \beta_\mathrm{s} \end{Bmatrix} = \begin{Bmatrix} (\overline{M}_F)_0 \\ (\overline{M}_F)_\mathrm{c} \\ (\overline{M}_F)_\mathrm{s} \end{Bmatrix} , \tag{4.66}$$

and

$$I_{\theta_k}^* \begin{bmatrix} 1 & & \\ & 1 & \\ & & 1 \end{bmatrix} \begin{Bmatrix} \ddot{\theta}_{k,0} \\ \ddot{\theta}_{k,\mathrm{c}} \\ \ddot{\theta}_{k,\mathrm{s}} \end{Bmatrix} + I_{\theta_k}^* \begin{bmatrix} 0 & 0 & 0 \\ 0 & 0 & 2 \\ 0 & -2 & 0 \end{bmatrix} \begin{Bmatrix} \dot{\theta}_{k,0} \\ \dot{\theta}_{k,\mathrm{c}} \\ \dot{\theta}_{k,\mathrm{s}} \end{Bmatrix}$$
$$+ I_{\theta_k}^* \begin{bmatrix} \overline{\omega}_k^2 & & \\ & (\overline{\omega}_k^2 - 1) & \\ & & (\overline{\omega}_k^2 - 1) \end{bmatrix} \begin{Bmatrix} \theta_{k,0} \\ \theta_{k,\mathrm{c}} \\ \theta_{k,\mathrm{s}} \end{Bmatrix} = \begin{Bmatrix} (\overline{N}_k)_0 \\ (\overline{N}_k)_\mathrm{c} \\ (\overline{N}_k)_\mathrm{s} \end{Bmatrix} , \tag{4.67}$$

in terms of the nondimensional blade inertias, and frequencies. The flapping moment $\overline{M}_F$ is derived solely from aerodynamic forces; however, the twist moment $\overline{N}$ includes contributions from root pitch actuation and a propeller moment, as well as aerodynamics. These effects will be discussed before the aerodynamics are formulated.

Full blade feathering can excite the elastic twist modes of the rotor blade through the D'Alembert inertial force resulting from the pitch motion. The torsion due to root pitch actuation is

$$N_{\ddot{\theta}} = -I_\theta \ddot{\theta}_{\mathrm{r}} \,. \tag{4.68}$$

Integrating this moment over the torsional mode shape gives the modal force due to root pitch actuation, which is

$$N_{\ddot{\theta}\,k} = -I_\theta \ddot{\theta}_{\mathrm{r}} \int_e^R \xi_{\theta_k}(r)dr \,. \tag{4.69}$$

Dividing $N_{\ddot{\theta}\,k}$ by $I_{\mathrm{b}}\Omega^2$ results in the nondimensional moment

$$\overline{N}_{\ddot{\theta}\,k} = -\frac{I_\theta^* \ddot{\theta}}{\Omega^2} \int_{\overline{e}}^1 \xi_{\theta_k}(\overline{r})d\overline{r} \,. \tag{4.70}$$

Appendix A uses a convenient notation to define common rotor integrals used in this derivation. The integral in equation (4.70) may be expressed as G_k^0, by using the definitions of Appendix A. The pitch acceleration $\ddot{\theta}_{\mathrm{r}}$ may be obtained by expressing θ_{r} in multiblade coordinates and differentiating twice with respect to nondimensional time $\overline{t}$. The pitch angle and angular acceleration are

$$\theta_{\mathrm{r}} = \theta_{\mathrm{r,0}} + \theta_{\mathrm{r,c}} \cos\psi + \theta_{\mathrm{r,s}} \sin\psi \,, \tag{4.71}$$

$$\begin{aligned}\ddot{\theta}_{\mathrm{r}} = \ddot{\theta}_{\mathrm{r,0}} + \ddot{\theta}_{\mathrm{r,c}} \cos\psi + \ddot{\theta}_{\mathrm{r,s}} \sin\psi - 2\dot{\theta}_{\mathrm{r,c}} \sin\psi + 2\dot{\theta}_{\mathrm{r,s}} \cos\psi - \theta_{\mathrm{r,c}} \cos\psi \\ - \theta_{\mathrm{r,s}} \sin\psi \,.\end{aligned} \tag{4.72}$$

So, the torsional moment due to root pitch actuation may be written in matrix form as

$$\begin{Bmatrix} (\overline{N}_{\ddot{\theta}\,k})_0 \\ (\overline{N}_{\ddot{\theta}\,k})_c \\ (\overline{N}_{\ddot{\theta}\,k})_s \end{Bmatrix} = -I_\theta^* G_k^0 \begin{bmatrix} 1 & 0 & 0 \\ 0 & 1 & 0 \\ 0 & 0 & 1 \end{bmatrix} \begin{Bmatrix} \ddot{\theta}_{\mathrm{r,0}} \\ \ddot{\theta}_{\mathrm{r,c}} \\ \ddot{\theta}_{\mathrm{r,s}} \end{Bmatrix} - I_\theta^* G_k^0 \begin{bmatrix} 0 & 0 & 0 \\ 0 & 0 & 2 \\ 0 & -2 & 0 \end{bmatrix} \begin{Bmatrix} \dot{\theta}_{\mathrm{r,0}} \\ \dot{\theta}_{\mathrm{r,c}} \\ \dot{\theta}_{\mathrm{r,s}} \end{Bmatrix}$$

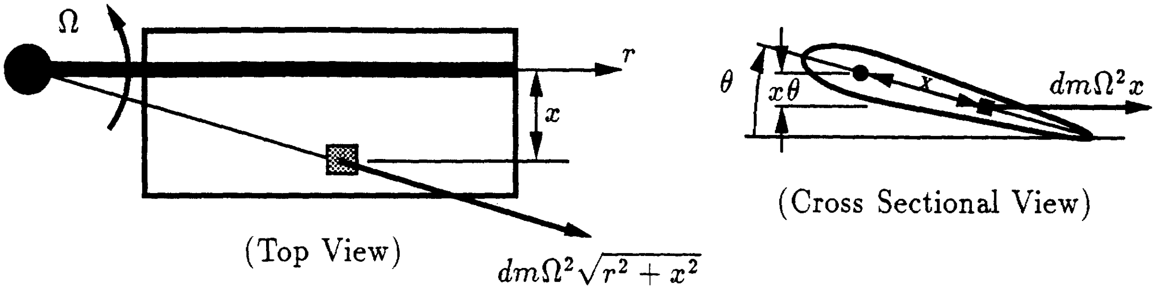

(Top View)

(Cross Sectional View)

Figure 4-3: Origin of the propeller moment (adapted from Figure 9-5 of Johnson [34]).

$$- I_\theta^* G_k^0 \begin{bmatrix} 0 & 0 & 0 \\ 0 & -1 & 0 \\ 0 & 0 & -1 \end{bmatrix} \begin{Bmatrix} \theta_{\mathrm{r},0} \\ \theta_{\mathrm{r},c} \\ \theta_{\mathrm{r},s} \end{Bmatrix} . \tag{4.73}$$

In the same way that centrifugal forces create a restoring moment for the blade flapping dynamics, they also create a restoring moment for the blade torsional dynamics. This restoring moment is usually referred to as a *propeller moment*, and is proportional to the pitch angle of the airfoil. The effect of the propeller moment was left out of the energy expression (4.49) of the previous Section, so that it could be treated separately here. Although its origin is subtle, the propeller moment tends to stiffen the rotor blade and deserves particular attention.

A rotor blade section at a pitch angle θ will experience a moment about its feathering axis due to centrifugal force [34, pg. 406]. For a blade mass element dm, the centrifugal force acts on a line through the center of rotation, as illustrated in Figure 4-3. If the blade mass element is a distance x behind the feathering axis there is then a chordwise component of this centrifugal force equal to $x\Omega^2 dm$. When the blade is pitched up by an angle θ, this chordwise force acts on a line a distance $x\theta$ below the feathering axis. If the mass element is forward of the feathering axis, the centrifugal force component is directed forward and acts on a line above the feathering axis.

Therefore, the propeller moment opposes the pitch motion of the blade and provides a restoring force. The effect of the propeller moment is a torsional stiffening of the rotor blade.

Figure 4-3 illustrates the moment about the feathering axis, developed by an element of mass *dm* due to the propeller moment. The sectional propeller moment can be approximated by assuming small pitch angles and integrating over the blade chord. This gives

$$N_\theta \approx -\int (x\theta)(x\Omega^2 dm) \approx -\Omega^2 I_\theta \theta \, , \tag{4.74}$$

where *dm* is the chordwise mass at a distance x behind the feathering axis. The propeller moment provides a constant moment about the feathering axis which "stiffens" the elastic twist modes of the rotor blade. Integration of the propeller moment over a mode shape gives the modal force due to the propeller moment

$$N_{\theta\, k} = -\Omega^2 I_\theta \int_{\bar{e}}^{1} \xi_{\theta_k}(\bar{r}) d\bar{r} \theta_{\mathrm{r}} - \Omega^2 I_\theta \int_{\bar{e}}^{1} \xi_{\theta_k}^2(\bar{r}) d\bar{r} \theta_k \, . \tag{4.75}$$

If $N_{\theta\, k}$ is normalized by $I_b \Omega^2$ and the integrals of Appendix A are used, the resulting nondimensional propeller moment is

$$\overline{N}_{\theta\, k} = -I_\theta^* G_k^0 \theta_{\mathrm{r}} - I_\theta^* H_k^0 \theta_k \, . \tag{4.76}$$

The root pitch angle θ_{r}, and the torsional modal coordinate θ_k were expressed in multiblade coordinates, and substituted into equation (4.76). Once again the collective and cyclic summation operators were applied, in order to obtain the effect of propeller moment on the torsion mode k in multiblade coordinates. The forcing due to the propeller moment is

$$\begin{Bmatrix} (\overline{N}_{\theta\, k})_{\mathrm{o}} \\ (\overline{N}_{\theta\, k})_{\mathrm{c}} \\ (\overline{N}_{\theta\, k})_{\mathrm{s}} \end{Bmatrix} = -I_\theta^* G_k^0 \begin{bmatrix} 1 & 0 & 0 \\ 0 & 1 & 0 \\ 0 & 0 & 1 \end{bmatrix} \begin{Bmatrix} \theta_{\mathrm{r},0} \\ \theta_{\mathrm{r,c}} \\ \theta_{\mathrm{r,s}} \end{Bmatrix} - I_\theta^* H_k^0 \begin{bmatrix} 1 & 0 & 0 \\ 0 & 1 & 0 \\ 0 & 0 & 1 \end{bmatrix} \begin{Bmatrix} \theta_{k,0} \\ \theta_{k,\mathrm{c}} \\ \theta_{k,\mathrm{s}} \end{Bmatrix} \tag{4.77}$$

The matrices governing the *in vacuo* dynamics of the rotor blade, including the effect of propeller moment and root pitch actuation, have been derived. The equations of motion have been transformed into multiblade coordinates, so that they describe the collective and cyclic modes of the rotor disk, in the fixed frame. Likewise, the matrices governing the aerodynamics of the rotor will be formulated in the next Section. The aerodynamics will be combined with the structural dynamics, in order to obtain a state space model describing the complete dynamics of the rotor disk.

4.5 Aerodynamics

The hub plane is defined as the reference plane normal to the rotor shaft, and α_{d} is the rotor disk plane angle of attack with respect to V, the helicopter velocity. The helicopter velocity may be decomposed into two components, one parallel to the disk plane and one normal to the disk plane. The velocities can be nondimensionalized by the rotor blade tip speed ΩR . The nondimensional component parallel to the disk plane is the advance ratio

$$\mu = \frac{V \cos \alpha_{\mathrm{d}}}{\Omega R} \ . \tag{4.78}$$

The nondimensional component normal to the disk plane is the free stream inflow ratio

$$\lambda_{\mathrm{f}} = \frac{V \sin \alpha_{\mathrm{d}}}{\Omega R} \ . \tag{4.79}$$

The total inflow is the free stream inflow plus the induced inflow (λ_{i}), so that

$$\lambda = \lambda_{\mathrm{f}} + \lambda_{\mathrm{i}} \ , \tag{4.80}$$

where the induced inflow is the rotor induced velocity divided by ΩR.

Although the inflow is generally a complicated function of radius and azimuth, a linear approximation can provide adequate results [34], [52], [53]. The linear approximation,

$$\lambda = \lambda_0 + \lambda_{\mathrm{c}} \bar{r} \cos \psi + \lambda_{\mathrm{s}} \bar{r} \sin \psi \ , \tag{4.81}$$

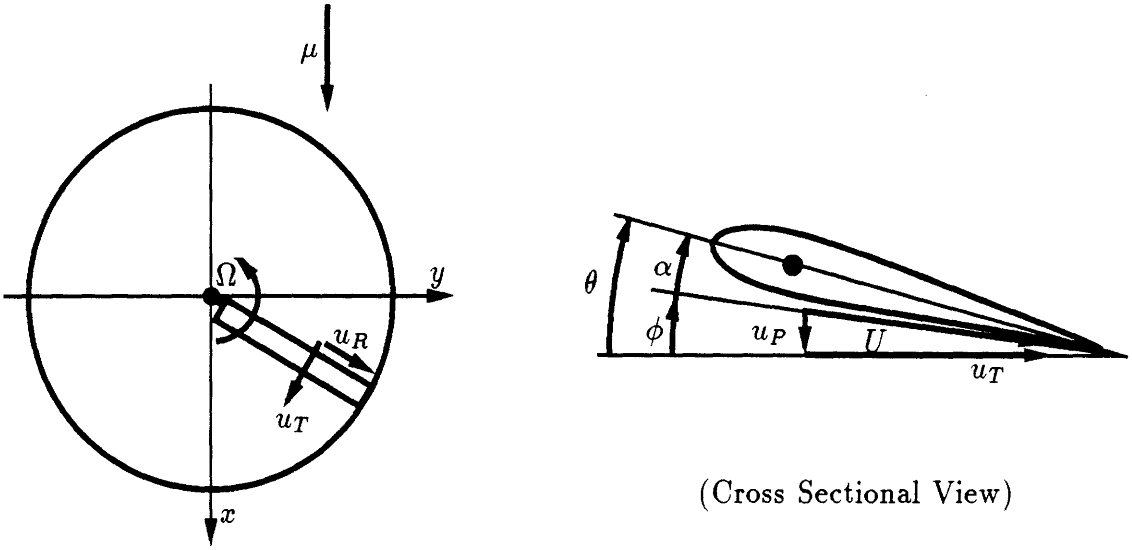

(Top View)

(Cross Sectional View)

Figure 4-4: Aerodynamics of the rotor blade (adapted from Figures 5-11 and 5-12 of Johnson [34]).

was used for the purpose of this research with simple dynamics developed by Pitt and Peters [53]. It will be discussed in more detail in Section 4.7.

The nondimensional rotating frame velocity components are u_T, u_R, and u_P, which are illustrated in Figure 4-4. The term u_T is the tangential velocity, u_R is the radial velocity, and u_P is the normal velocity. In forward flight these velocity components are

$$u_T = \bar{r} + \mu \sin\psi \ , \tag{4.82}$$

$$u_R = \mu \cos\psi \ , \tag{4.83}$$

$$u_P = \lambda + (\bar{r} - \bar{e})\dot{\beta} + \mu\beta\cos\psi \ , \tag{4.84}$$

which are functions of the rotor blade azimuth ψ. The sectional radius has been normalized by R, so that $\bar{r} = r/R$. A flap hinge offset of length e has been assumed, and it is also normalized by R, so that $\bar{e} = e/R$. Figure 4-4 also illustrates the respective angles of the rotor blade aerodynamics. The lift and drag sectional aerodynamic forces on a blade are

$$L = \frac{1}{2}\rho c U^2 (\Omega R)^2 c_l \; , \tag{4.85}$$

and

$$D = \frac{1}{2}\rho c U^2 (\Omega R)^2 c_d \; , \tag{4.86}$$

respectively, where $U = \sqrt{u_T^2 + u_P^2}$, c_l is the sectional lift coefficient, and c_d is the sectional drag coefficient. The angle of attack is $\alpha = \theta - \phi$, where ϕ is the inflow angle of the section. The vertical force on a sectional element of the rotor blade is

$$F_z = L\cos\phi - D\sin\phi \; , \tag{4.87}$$

which can be simplified if small angle approximations are made. If λ, β, ϕ, and θ are small, then u_P/u_T and α will also be small. Thus, $\phi \approx u_P/u_T$, $\alpha \approx \theta - u_P/u_T$, and $U^2 \approx u_T^2$. With the small angle approximations $F_z \approx L$, so we have

$$F_z \approx \frac{1}{2}\rho c u_T^2 (\Omega R)^2 c_l \; . \tag{4.88}$$

The sectional lift coefficient is generally a complicated function of section geometry, angle of attack, Mach number, and Reynolds number, among other things. In this model, however, c_l will be approximated by a linear combination of angle of attack α, and servoflap deflection η, so that

$$c_l = c_{l_\alpha}\alpha + c_{l_\eta}\eta \; . \tag{4.89}$$

The lift curves are assumed to be linear, with the constant slopes $c_{l_\alpha} = a$, and $c_{l_\eta} = n$. The contribution due to the servoflap is nonzero only from $\overline{r} = \overline{r}_1$ to $\overline{r} = \overline{r}_2$, the spanwise extent of the servoflap. Outside of this range $c_{l_\eta} = 0$. The sectional pitch is a combination of the root pitch angle and the elastic twist of the blade, so that the sectional angle of attack is

$$\alpha = \theta_r + \theta_k - u_P/u_T \; . \tag{4.90}$$

Since the generalized coordinates for the rotor model are the flapping angle β and the torsional modes θ_k, the generalized forces are the flapping moment M_F and the modal torsion N_k. The airfoil is assumed to be symmetric with $c_{m_\alpha} = 0$, and the aerodynamic center and elastic axis of the airfoil coincide, so that the only aerodynamic force that twists the blade is due to the servoflap. The moments will be derived in terms of the aerodynamic forces on the blade, and multiblade coordinates will be used to express the influence of the moments on the three rotor disk modes.

The sectional lift along the blade produces a moment about the flapping hinge with moment arm $(r - e)$. The total flapping moment may be obtained by integrating the sectional lift over the moment arm. This gives

$$M_F = \int_e^R (r - e) L dr \ . \tag{4.91}$$

Nondimensionalizing M_F by $I_b \Omega^2$ gives

$$\frac{M_F}{I_b \Omega^2} = \gamma \int_{\bar{e}}^{1} \frac{1}{2} (\bar{r} - \bar{e}) u_T^2 \alpha d\bar{r} + \gamma \int_{\bar{r}_1}^{\bar{r}_2} \frac{1}{2} \bar{n} (\bar{r} - \bar{e}) u_T^2 \eta d\bar{r} \ , \tag{4.92}$$

where γ is the Lock number, η is the servoflap deflection, and $\bar{n}$ is the lift coefficient of the servoflap divided by the lift curve slope of the airfoil a. The angle of attack in equation (4.92) can be expanded to give

$$\alpha(\bar{r}) = \theta_r + \theta_{tw} - \frac{u_P}{u_T} \tag{4.93}$$

$$= \theta_r + \theta_{tw} - \frac{1}{u_T} \left(\lambda + \mu \beta \cos \psi + (\bar{r} - \bar{e}) \dot{\beta} \right) \ . \tag{4.94}$$

Note that pitch, flapping, and downwash affect the apparent angle of attack of the blade, and therefore the lift. The nondimensional flapping moment has contributions due to the servoflap deflection and each variation in angle of attack, so that

$$\overline{M}_F = \overline{M}_{\theta_r} + \overline{M}_{\theta_k} + \overline{M}_\lambda + \overline{M}_\beta + \overline{M}_{\dot{\beta}} + \overline{M}_\eta \ . \tag{4.95}$$

The angle of attack expansion of equation (4.94) may be substituted into the flapping moment equation (4.92), to give the components of the flapping moment

$$\overline{M}_{\theta_{\mathrm{r}}} = \gamma \int_{\overline{e}}^{1} \frac{1}{2}(\overline{r}-\overline{e}) u_T^2 d\overline{r}\, \theta_{\mathrm{r}} \,, \tag{4.96}$$

$$\overline{M}_{\theta_k} = \gamma \int_{\overline{e}}^{1} \frac{1}{2}(\overline{r}-\overline{e}) \xi_{\theta_k}(\overline{r}) u_T^2 d\overline{r}\, \theta_k \,, \tag{4.97}$$

$$\overline{M}_{\lambda} = -\gamma \int_{\overline{e}}^{1} \frac{1}{2}(\overline{r}-\overline{e}) u_T \lambda(\overline{r}) d\overline{r} \,, \tag{4.98}$$

$$\overline{M}_{\beta} = -\gamma \int_{\overline{e}}^{1} \frac{1}{2}(\overline{r}-\overline{e}) \xi_{\beta}'(\overline{r}) u_T (\mu \cos\psi) d\overline{r}\, \beta \,, \tag{4.99}$$

$$\overline{M}_{\dot\beta} = -\gamma \int_{\overline{e}}^{1} \frac{1}{2}(\overline{r}-\overline{e}) \xi_{\beta}(\overline{r}) u_T d\overline{r}\, \dot\beta \,, \tag{4.100}$$

$$\overline{M}_{\eta} = \gamma \int_{\overline{r}_1}^{\overline{r}_2} \frac{1}{2}(\overline{r}-\overline{e}) \overline{n} u_T^2 d\overline{r}\, \eta \,. \tag{4.101}$$

where $\xi_\beta(\overline{r})$ represents the mode shapes of the blade flapping. Only rigid flapping is assumed in the current model, so that $\xi_\beta(\overline{r}) = (\overline{r}-\overline{e})$. Note that $\overline{M}_\eta$ is integrated over the servoflap, from $\overline{r}_1$ to $\overline{r}_2$. The linear inflow approximation, $\lambda = \lambda_0 + \lambda_c \overline{r} \cos\psi + \lambda_s \overline{r} \sin\psi$, and the velocity component $u_T = \overline{r} + \mu \sin\psi$ may be substituted into the flapping moment components and expanded. Finally, substitution of the rotor integrals of Appendix A into the moment integral expansions yields

$$\overline{M}_{\theta_{\mathrm{r}}} = \frac{\gamma}{2}\left[J^2 + 2\mu J^1 \sin\psi + \mu^2 J^0 \sin^2\psi\right] \theta_{\mathrm{r}} \,, \tag{4.102}$$

$$\overline{M}_{\theta_k} = \frac{\gamma}{2}\left[M_k^2 + 2\mu M_k^1 \sin\psi + \mu^2 M_k^0 \sin^2\psi\right] \theta_k \,, \tag{4.103}$$

$$\begin{aligned} \overline{M}_{\lambda} = &-\frac{\gamma}{2}\left[J^1 + \mu J^0 \sin\psi\right] \lambda_0 \\ &- \frac{\gamma}{2}\left[J^2 + \mu J^1 \sin\psi\right] (\lambda_c \cos\psi + \lambda_s \sin\psi) \,, \end{aligned} \tag{4.104}$$

$$\overline{M}_{\beta} = -\frac{\gamma}{2}\left[\mu L^1 \cos\psi + \mu^2 L^0 \cos\psi \sin\psi\right] \beta \,, \tag{4.105}$$

$$\overline{M}_{\dot\beta} = -\frac{\gamma}{2}\left[K^1 + \mu K^0 \sin\psi\right] \dot\beta \,, \tag{4.106}$$

$$\overline{M}_{\eta} = \frac{\gamma}{2}\left[\overline{n} B^2 + 2\overline{n}\mu B^1 \sin\psi + \overline{n}\mu^2 B^0 \sin^2\psi\right] \eta \,. \tag{4.107}$$

Multiblade coordinates may be used in the flapping moment expressions, while the collective and cyclic summation operators are applied. The resulting aerodynamic flapping moments in multiblade coordinates are

$$
\begin{aligned}
\begin{Bmatrix} (\overline{M}_{\mathrm{F}})_0 \\ (\overline{M}_{\mathrm{F}})_c \\ (\overline{M}_{\mathrm{F}})_s \end{Bmatrix} = {} & \gamma \begin{bmatrix} 0 & (\frac{1}{4}\mu K^0 - \frac{1}{4}\mu L^1) & 0 \\ (-\frac{1}{2}\mu L^1) & 0 & (-\frac{1}{2}K^1 - \frac{1}{8}\mu^2 L^0) \\ 0 & (\frac{1}{2}K^1 - \frac{1}{8}\mu^2 L^0) & 0 \end{bmatrix} \begin{Bmatrix} \beta_0 \\ \beta_{\mathrm{c}} \\ \beta_{\mathrm{s}} \end{Bmatrix} \\
& + \gamma \begin{bmatrix} (-\frac{1}{2}K^1) & 0 & (-\frac{1}{4}\mu K^0) \\ 0 & (-\frac{1}{2}K^1) & 0 \\ (-\frac{1}{2}\mu K^0) & 0 & (-\frac{1}{2}K^1) \end{bmatrix} \begin{Bmatrix} \dot{\beta}_0 \\ \dot{\beta}_{\mathrm{c}} \\ \dot{\beta}_{\mathrm{s}} \end{Bmatrix} \\
& + \gamma \begin{bmatrix} (\frac{1}{4}\mu^2 J^0 + \frac{1}{2}J^2) & 0 & (\frac{1}{2}\mu J^1) \\ 0 & (\frac{1}{8}\mu^2 J^0 + \frac{1}{2}J^2) & 0 \\ (\mu J^1) & 0 & (\frac{3}{8}\mu^2 J^0 + \frac{1}{2}J^2) \end{bmatrix} \begin{Bmatrix} \theta_{\mathrm{r},0} \\ \theta_{\mathrm{r},\mathrm{c}} \\ \theta_{\mathrm{r},\mathrm{s}} \end{Bmatrix} \\
& + \gamma \begin{bmatrix} (\frac{1}{4}\mu^2 M_k^0 + \frac{1}{2}M_k^2) & 0 & (\frac{1}{2}\mu M_k^1) \\ 0 & (\frac{1}{8}\mu^2 M_k^0 + \frac{1}{2}M_k^2) & 0 \\ (\mu M_k^1) & 0 & (\frac{3}{8}\mu^2 M_k^0 + \frac{1}{2}M_k^2) \end{bmatrix} \begin{Bmatrix} \theta_{k,0} \\ \theta_{k,\mathrm{c}} \\ \theta_{k,\mathrm{s}} \end{Bmatrix} \\
& + \gamma \begin{bmatrix} (-\frac{1}{2}J^1) & 0 & (-\frac{1}{4}\mu J^1) \\ 0 & (-\frac{1}{2}J^2) & 0 \\ (-\frac{1}{2}\mu J^0) & 0 & (-\frac{1}{2}J^2) \end{bmatrix} \begin{Bmatrix} \lambda_0 \\ \lambda_{\mathrm{c}} \\ \lambda_{\mathrm{s}} \end{Bmatrix} \\
& + \gamma \begin{bmatrix} (\frac{1}{4}\overline{n}\mu^2 B^0 + \frac{1}{2}\overline{n}B^2) & 0 & (\frac{1}{2}\overline{n}\mu B^1) \\ 0 & (\frac{1}{8}\overline{n}\mu^2 B^0 + \frac{1}{2}\overline{n}B^2) & 0 \\ (\overline{n}\mu B^1) & 0 & (\frac{3}{8}\overline{n}\mu^2 B^0 + \frac{1}{2}\overline{n}B^2) \end{bmatrix} \begin{Bmatrix} \eta_0 \\ \eta_{\mathrm{c}} \\ \eta_{\mathrm{s}} \end{Bmatrix}
\end{aligned}
\tag{4.108}
$$

The torsional moment due to aerodynamic forces was referred to as N_{aero}, in Section 4.4. This moment has components due to both servoflap deflection and aerodynamic damping. The generalized force for the torsional mode k due to these aerodynamics may be calculated by integrating N_{aero} over the torsional mode shape. The moment corresponding to the torsional mode k is

$$\overline{N}_{\mathrm{aero}\,k} = \overline{N}_{\eta\,k} + \overline{N}_{\dot{\theta}\,k} \,, \tag{4.109}$$

where $\overline{N}_{\eta\,k}$ is the moment due to servoflap deflection, and $\overline{N}_{\dot{\theta}\,k}$ is aerodynamic damping. Deflecting the servoflap produces a moment about the rotor blade

$$\overline{N}_{\eta\,k} = \gamma \int_{\overline{r}_1}^{\overline{r}_2} \frac{1}{2}\overline{pc}\xi_{\theta_k}(\overline{r})u_T^2 d\overline{r}\,\eta\;. \tag{4.110}$$

Aerodynamic forces are primarily responsible for damping the torsional motion of the rotor blade, and tend to dominate structural damping. If quasi-steady aerodynamics are assumed, and the elastic axis coincides with the quarter chord, the equations of motion for the torsional dynamics will include a damping term [6, pg. 279] of the form

$$\overline{N}_{\dot{\theta}\,k} = -\gamma \int_{\overline{e}}^{1} \frac{\overline{c}^2}{16}\xi_{\theta_k}^2(\overline{r})u_T d\overline{r}\,\dot{\theta}_k\;. \tag{4.111}$$

When the tangential velocity is expanded as $u_T = \overline{r} + \mu \sin\psi$ in equations (4.110) and (4.111), the moments can be expressed in terms of the rotor integrals of Appendix A, to give

$$\overline{N}_{\eta\,k} = \frac{\gamma\overline{pc}}{2}\left[C_k^2 + 2\mu C_k^1 \sin\psi + \mu^2 C_k^0 \sin^2\psi\right]\eta\;, \tag{4.112}$$

$$\overline{N}_{\dot{\theta}\,k} = -\frac{\gamma\overline{c}^2}{16}\left[H_k^1 + \mu H_k^0 \sin\psi\right]\dot{\theta}_k\;. \tag{4.113}$$

Once again, multiblade coordinates are used for the degrees of freedom η and θ_k, and the collective and cyclic summation operators are applied to equations (4.112) and (4.113). The torsional moments in multiblade coordinates are

$$\begin{Bmatrix} (\overline{N}_{\mathrm{aero}\,k})_0 \\ (\overline{N}_{\mathrm{aero}\,k})_{\mathrm{c}} \\ (\overline{N}_{\mathrm{aero}\,k})_{\mathrm{s}} \end{Bmatrix} = \gamma \begin{bmatrix} 0 & (\frac{1}{32}\mu\overline{c}^2 H_k^0) & 0 \\ 0 & 0 & (-\frac{1}{16}\overline{c}^2 H_k^1) \\ 0 & (\frac{1}{16}\overline{c}^2 H_k^1) & 0 \end{bmatrix} \begin{Bmatrix} \theta_{k,0} \\ \theta_{k,\mathrm{c}} \\ \theta_{k,\mathrm{s}} \end{Bmatrix}$$

$$+\gamma \begin{bmatrix} (-\frac{1}{16}\overline{c}^2 H_k^1) & 0 & (-\frac{1}{32}\mu\overline{c}^2 H_k^0) \\ 0 & (-\frac{1}{16}\overline{c}^2 H_k^1) & 0 \\ (-\frac{1}{16}\mu\overline{c}^2 H_k^0) & 0 & (-\frac{1}{16}\overline{c}^2 H_k^1) \end{bmatrix} \begin{Bmatrix} \dot{\theta}_{k,0} \\ \dot{\theta}_{k,\mathrm{c}} \\ \dot{\theta}_{k,\mathrm{s}} \end{Bmatrix}$$

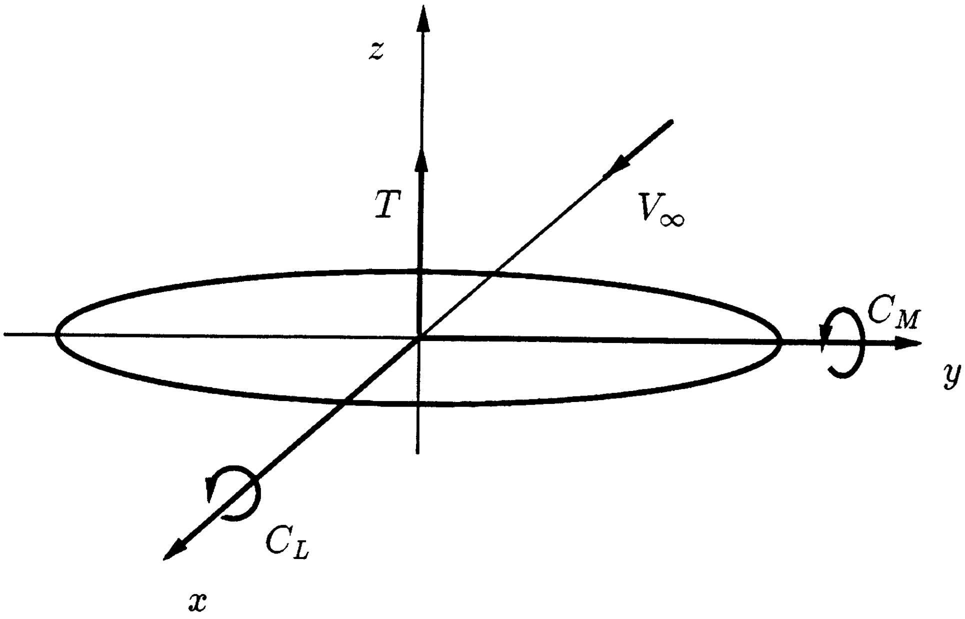

Figure 4-5: Rotor disk coordinates and direction of hub loads.

$$+\gamma\begin{bmatrix} (\frac{1}{4}\overline{pc}\mu^2C_k^0+\frac{1}{2}\overline{pc}C_k^2) & 0 & (\frac{1}{2}\overline{pc}\mu C_k^1) \\ 0 & (\frac{1}{8}\overline{pc}\mu^2C_k^0+\frac{1}{2}\overline{pc}C_k^2) & 0 \\ (\overline{pc}\mu C_k^1) & 0 & (\frac{3}{8}\overline{pc}\mu^2C_k^0+\frac{1}{2}\overline{pc}C_k^2) \end{bmatrix}\begin{Bmatrix} \eta_0 \\ \eta_c \\ \eta_s \end{Bmatrix} \qquad (4.114)$$

4.6 Hub Reactions

The hub reactions of interest in this model are T, M_x, and M_y, the thrust, roll moment, and pitch moment respectively. Helicopter axes are usually oriented with the z axis pointing upward, the x axis pointing rearward, and the y axis pointing starboard. The thrust force is defined as positive in the upward direction normal to the disk plane (in the z direction). The roll moment is positive toward the retreating side (about the x axis), and the pitch moment is positive "nose up" (about the y axis). The fixed frame vehicle axes and hub loads appear in Figure 4-5.

The forces and moments on individual blades in the rotating frame appear as hub loads in the fixed frame. The vertical shear force S and flapping hinge moment M_β are primarily responsible for the body forces of interest, namely T, M_x, and M_y. The root moment, M_β, results from the flapping angle of the rotor blade. For a rotor blade with a flap hinge, this moment will be nonzero only if the configuration includes a hinge spring. The root flap moment is then

$$M_\beta = K_\beta \beta \ , \tag{4.115}$$

where K_β is the spring constant of the flapping hinge.

The vertical shear force at the blade root S is the integral of the vertical force acting along the blade, where the vertical force is composed of the section aerodynamic lift acting upward and the section inertia force acting downward. The vertical shear force is therefore

$$S = \int_e^R F_z dr - \int_e^R m\ddot{z} dr \ . \tag{4.116}$$

For a blade with a flap hinge offset of length e, the sectional vertical acceleration is

$$\ddot{z} \approx (r - e)\ddot{\beta} \ . \tag{4.117}$$

The first integral in the expression for S is due to aerodynamic forces on the blade. Assuming small angles, the vertical force F_z on the blade is approximately the sectional lift L. The second integral is a result of the blade flapping inertia. If the vertical acceleration $\ddot{z}$ from equation (4.117) is substituted into equation (4.116), and L is substituted for F_z, then the vertical shear force becomes

$$S = \int_e^R \frac{1}{2}\rho c u_T^2 (\Omega R)^2 c_l dr - \int_e^R m(r - e)\ddot{\beta} dr \ . \tag{4.118}$$

The resultant force is normalized by $\rho A(\Omega R)^2$, so that $\overline{S} = S/\rho A(\Omega R)^2$. The normalized shear force may be written in terms of the nondimensional radius $\overline{r}$ as

$$\overline{S} = \frac{\sigma a}{N}\int_{\overline{e}}^{1} \frac{1}{2} u_T^2 \alpha d\overline{r} + \frac{\sigma a}{N}\int_{\overline{r}_1}^{\overline{r}_2} \frac{1}{2}\overline{n} u_T^2 \eta d\overline{r} - \frac{\sigma a}{N}\left(\frac{J^0}{\gamma D^2}\right)\ddot{\beta} \ . \tag{4.119}$$

The shear force has components due to the sectional angle of attack defined in equation (4.94), as well as the servoflap angle, and blade inertia. Therefore, the vertical shear force may be written as

$$\overline{S} = \overline{S}_{\theta_r} + \overline{S}_{\theta_k} + \overline{S}_{\lambda} + \overline{S}_{\beta} + \overline{S}_{\dot{\beta}} + \overline{S}_{\ddot{\beta}} + \overline{S}_{\eta} \; , \tag{4.120}$$

where the components of the vertical shear force are

$$\overline{S}_{\theta_r} = \frac{\sigma a}{N} \int_{\overline{e}}^{1} \frac{1}{2} u_T^2 d\overline{r} \, \theta_r \; , \tag{4.121}$$

$$\overline{S}_{\theta_k} = \frac{\sigma a}{N} \int_{\overline{e}}^{1} \frac{1}{2} \xi_{\theta_k}(\overline{r}) u_T^2 d\overline{r} \, \theta_k \; , \tag{4.122}$$

$$\overline{S}_{\lambda} = -\frac{\sigma a}{N} \int_{\overline{e}}^{1} \frac{1}{2} u_T \lambda(\overline{r}) d\overline{r} \; , \tag{4.123}$$

$$\overline{S}_{\beta} = -\frac{\sigma a}{N} \int_{\overline{e}}^{1} \frac{1}{2} \xi_{\beta}'(\overline{r}) u_T (\mu \cos\psi) d\overline{r} \, \beta \; , \tag{4.124}$$

$$\overline{S}_{\dot{\beta}} = -\frac{\sigma a}{N} \int_{\overline{e}}^{1} \frac{1}{2} \xi_{\beta}(\overline{r}) u_T d\overline{r} \, \dot{\beta} \; , \tag{4.125}$$

$$\overline{S}_{\ddot{\beta}} = -\frac{\sigma a}{N} \left(\frac{J^0}{\gamma D^2} \right) \ddot{\beta} \; , \tag{4.126}$$

$$\overline{S}_{\eta} = \frac{\sigma a}{N} \int_{r_1}^{r_2} \frac{1}{2} \overline{n} u_T^2 d\overline{r} \, \eta \; . \tag{4.127}$$

By substituting the integrals of Appendix A, the vertical shear forces can be written

$$\overline{S}_{\theta_r} = \frac{\sigma a}{2N} \left[D^2 + 2\mu D^1 \sin\psi + \mu^2 D^0 \sin^2\psi \right] \theta_r \; , \tag{4.128}$$

$$\overline{S}_{\theta_k} = \frac{\sigma a}{2N} \left[G_k^2 + 2\mu G_k^1 \sin\psi + \mu^2 G_k^0 \sin^2\psi \right] \theta_k \; , \tag{4.129}$$

$$\begin{aligned} \overline{S}_{\lambda} = & -\frac{\sigma a}{2N} \left[D^1 + \mu D^0 \sin\psi \right] \lambda_0 \\ & - \frac{\sigma a}{2N} \left[D^2 + \mu D^1 \sin\psi \right] (\lambda_c \cos\psi + \lambda_s \sin\psi) \; , \end{aligned} \tag{4.130}$$

$$\overline{S}_{\beta} = -\frac{\sigma a}{2N} \left[\mu F^1 \cos\psi + \mu^2 F^0 \cos\psi \sin\psi \right] \beta \; , \tag{4.131}$$

$$\overline{S}_{\dot{\beta}} = -\frac{\sigma a}{2N} \left[E^1 + \mu E^0 \sin\psi \right] \dot{\beta} \; , \tag{4.132}$$

$$\overline{S}_{\ddot{\beta}} = -\frac{\sigma a}{N} \left[\frac{J^0}{\gamma D^2} \right] \ddot{\beta} \; , \tag{4.133}$$

$$\overline{S}_{\eta} = \frac{\sigma a}{2N} \left[\overline{n} A^2 + 2\overline{n} \mu A^1 \sin\psi + \overline{n} \mu^2 A^0 \sin^2\psi \right] \eta \; . \tag{4.134}$$

The rotor thrust is calculated by summing the vertical shear forces of each blade, so that

$$T = \sum_{q=1}^{\mathrm{N}} S_q \, , \tag{4.135}$$

where S_q is the shear contribution from the qth blade. Nondimensionalizing the thrust by $\rho A(\Omega R)^2$ gives the thrust coefficient

$$C_T = \frac{T}{\rho A(\Omega R)^2} = \sum_{q=1}^{\mathrm{N}} \overline{S}_q = \mathrm{N}(\overline{S}_q)_0 \, . \tag{4.136}$$

The thrust coefficient written in terms of the shear components and the collective summation operator is

$$C_T = \mathrm{N}\left((\overline{S}_{\theta_t})_0 + (\overline{S}_{\theta_k})_0 + (\overline{S}_{\lambda})_0 + (\overline{S}_{\beta})_0 + (\overline{S}_{\dot{\beta}})_0 + (\overline{S}_{\ddot{\beta}})_0 + (\overline{S}_{\eta})_0\right) \, . \tag{4.137}$$

The moment on the rotor hub produced by a blade has two components, one due to the hinge moment M_β, and the other produced by the vertical shear force acting at a distance e away from the hub center. Therefore, the hub moment due to the qth blade is

$$M_q = (M_\beta + e\,S)_q \tag{4.138}$$

The contributions of the hinge moment and vertical shear to the hub moment are depicted in Figure 4-6. The moment may be nondimensionalized by $\rho AR(\Omega R)^2$, so that

$$\begin{aligned} C_{M_q} &= \frac{M_\beta + e\,S}{\rho AR(\Omega R)^2} \\ &= \frac{\sigma a}{\mathrm{N}\gamma}\left(\frac{K_\beta}{I_\mathrm{b}\Omega^2}\right)\beta + \overline{e}\,\overline{S} \end{aligned} \tag{4.139}$$

If $(K_\beta / I_\mathrm{b}\Omega^2)$ is expressed in terms of the nondimensional free-flapping frequency $\overline{\omega}_\beta$, and equation (4.120) is substituted for $\overline{S}$ in equation (4.139), then the expression

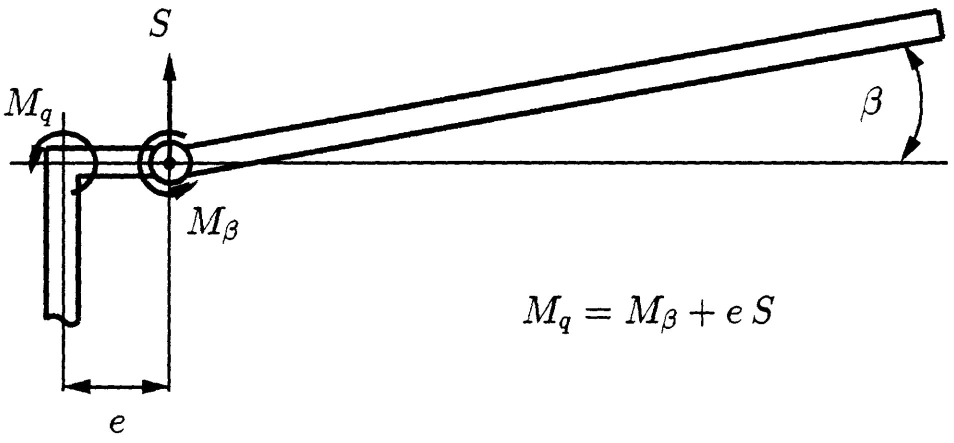

Figure 4-6: Hub moment due to vertical shear force and hinge moment.

becomes

$$C_{M_q} = \frac{\sigma a}{\mathrm{N}\gamma}\left(\overline{\omega}_\beta^2 I_\beta^*\right)\beta + \overline{e}\left(\overline{S}_{\theta_r} + \overline{S}_{\theta_k} + \overline{S}_\lambda + \overline{S}_\beta + \overline{S}_{\dot\beta} + \overline{S}_{\ddot\beta} + \overline{S}_\eta\right) \ . \tag{4.140}$$

The components in the M_y and M_x directions are

$$(C_{M_q})_y = -C_{M_q}\cos\psi_q \ , \tag{4.141}$$

and

$$(C_{M_q})_x = \quad C_{M_q}\sin\psi_q \ , \tag{4.142}$$

respectively. These give the contribution to the pitch and roll coefficients due to the qth blade. If the contributions of each blade are summed, then the pitch and roll coefficients are

$$C_M = \sum_{q=1}^{\mathrm{N}} -C_{M_q}\cos\psi_q = -\mathrm{N}(C_{M_q})_c \ , \tag{4.143}$$

and

$$C_L = \sum_{q=1}^{\mathrm{N}} \ \ C_{M_q}\sin\psi_q = \mathrm{N}(C_{M_q})_s \ , \tag{4.144}$$

respectively. The pitch and roll coefficients written in terms of the shear components and cyclic summation operators are

$$C_M = -\sum_{q=1}^{\mathrm{N}} \left(\frac{\sigma a}{\mathrm{N}\gamma} \left(\overline{\omega}_\beta^2 I_\beta^* \right) \beta_q + \overline{e}\overline{S}_q \right) \cos\psi_q \tag{4.145}$$

$$= -\sigma a \left(\frac{\overline{\omega}_\beta^2 I_\beta^*}{2\gamma} \right) \beta_{\mathrm{c}} - \frac{1}{2}\overline{e}\mathrm{N} \left((\overline{S}_{\theta_r})_{\mathrm{c}} + (\overline{S}_{\theta_k})_{\mathrm{c}} + (\overline{S}_\lambda)_{\mathrm{c}} + (\overline{S}_\beta)_{\mathrm{c}} + (\overline{S}_{\dot\beta})_{\mathrm{c}} + (\overline{S}_{\ddot\beta})_{\mathrm{c}} + (\overline{S}_\eta)_{\mathrm{c}} \right) , \tag{4.146}$$

and

$$C_L = \sum_{q=1}^{\mathrm{N}} \left(\frac{\sigma a}{\mathrm{N}\gamma} \left(\overline{\omega}_\beta^2 I_\beta^* \right) \beta(\psi_q) + \overline{e}\overline{S}_q \right) \sin\psi_q \tag{4.147}$$

$$= \sigma a \left(\frac{\overline{\omega}_\beta^2 I_\beta^*}{2\gamma} \right) \beta_{\mathrm{s}} + \frac{1}{2}\overline{e}\mathrm{N} \left((\overline{S}_{\theta_r})_{\mathrm{s}} + (\overline{S}_{\theta_k})_{\mathrm{s}} + (\overline{S}_\lambda)_{\mathrm{s}} + (\overline{S}_\beta)_{\mathrm{s}} + (\overline{S}_{\dot\beta})_{\mathrm{s}} + (\overline{S}_{\ddot\beta})_{\mathrm{s}} + (\overline{S}_\eta)_{\mathrm{s}} \right) . \tag{4.148}$$

Once again the degrees of freedom can be expressed in multiblade coordinates for the collective and cyclic rotor disk modes. The thrust, pitch, and roll coefficients written in matrix form are

$$\begin{Bmatrix} C_T \\ C_M \\ C_L \end{Bmatrix} = \sigma a \begin{bmatrix} 0 & (\frac{1}{4}\mu E^0 - \frac{1}{4}\mu F^1) & 0 \\ (\frac{1}{4}\overline{e}\mu F^1) & (-\frac{1}{2\gamma}\overline{\omega}_\beta^2 I_\beta^* - \frac{1}{2}\overline{e}\frac{J^0}{\gamma D^2}) & (\frac{1}{4}\overline{e}E^1 + \frac{1}{16}\overline{e}\mu^2 F^0 \\ 0 & (\frac{1}{4}\overline{e}E^1 - \frac{1}{16}\overline{e}\mu^2 F^0) & (\frac{1}{2\gamma}\overline{\omega}_\beta^2 I_\beta^* + \frac{1}{2}\overline{e}\frac{J^0}{\gamma D^2}) \end{bmatrix} \begin{Bmatrix} \beta_0 \\ \beta_{\mathrm{c}} \\ \beta_{\mathrm{s}} \end{Bmatrix}$$

$$+ \sigma a \begin{bmatrix} (-\frac{1}{2}E^1) & 0 & (-\frac{1}{4}\mu E^0) \\ 0 & (\frac{1}{4}\overline{e}E^1) & (\overline{e}\frac{J^0}{\gamma D^2}) \\ (-\frac{1}{4}\overline{e}\mu E^0) & (\overline{e}\frac{J^0}{\gamma D^2}) & (-\frac{1}{4}\overline{e}E^1) \end{bmatrix} \begin{Bmatrix} \dot\beta_0 \\ \dot\beta_{\mathrm{c}} \\ \dot\beta_{\mathrm{s}} \end{Bmatrix}$$

$$+ \sigma a \begin{bmatrix} (-\frac{J^0}{\gamma D^2}) & 0 & 0 \\ 0 & (\frac{1}{2}\overline{e}\frac{J^0}{\gamma D^2}) & 0 \\ 0 & 0 & (-\frac{1}{2}\overline{e}\frac{J^0}{\gamma D^2}) \end{bmatrix} \begin{Bmatrix} \ddot\beta_0 \\ \ddot\beta_{\mathrm{c}} \\ \ddot\beta_{\mathrm{s}} \end{Bmatrix}$$

$$+\sigma a\begin{bmatrix} (\frac{1}{4}\mu^2 D^0+\frac{1}{2}D^2) & 0 & (\frac{1}{2}\mu D^1) \\ 0 & (-\frac{1}{16}\overline{e}\mu^2 D^0-\frac{1}{4}\overline{e}D^2) & 0 \\ (\frac{1}{2}\overline{e}\mu D^1) & 0 & (\frac{3}{16}\overline{e}\mu^2 D^0+\frac{1}{4}\overline{e}D^2) \end{bmatrix}\begin{Bmatrix} \theta_{\mathrm{r},0} \\ \theta_{\mathrm{r,c}} \\ \theta_{\mathrm{r,s}} \end{Bmatrix}$$

$$+\sigma a\begin{bmatrix} (\frac{1}{4}\mu^2 G_k^0+\frac{1}{2}G_k^2) & 0 & (\frac{1}{2}\mu G_k^1) \\ 0 & (-\frac{1}{16}\overline{e}\mu^2 G_k^0-\frac{1}{4}\overline{e}G_k^2) & 0 \\ (\frac{1}{2}\overline{e}\mu G_k^1) & 0 & (\frac{3}{16}\overline{e}\mu^2 G_k^0+\frac{1}{4}\overline{e}G_k^2) \end{bmatrix}\begin{Bmatrix} \theta_{k,0} \\ \theta_{k,\mathrm{c}} \\ \theta_{k,\mathrm{s}} \end{Bmatrix}$$

$$+\sigma a\begin{bmatrix} (-\frac{1}{2}D^1) & 0 & (-\frac{1}{4}\mu D^1) \\ 0 & (\frac{1}{4}\overline{e}D^2) & 0 \\ (-\frac{1}{4}\overline{e}\mu D^0) & 0 & (-\frac{1}{4}\overline{e}D^2) \end{bmatrix}\begin{Bmatrix} \lambda_0 \\ \lambda_{\mathrm{c}} \\ \lambda_{\mathrm{s}} \end{Bmatrix}$$

$$+\sigma a\begin{bmatrix} (\frac{1}{4}\overline{n}\mu^2 A^0+\frac{1}{2}\overline{n}A^2) & 0 & (\frac{1}{2}\overline{n}\mu A^1) \\ 0 & (-\frac{1}{16}\overline{en}\mu^2 A^0-\frac{1}{4}\overline{en}A^2) & 0 \\ (\frac{1}{2}\overline{en}\mu A^1) & 0 & (\frac{3}{16}\overline{en}\mu^2 A^0+\frac{1}{4}\overline{en}A^2) \end{bmatrix}\begin{Bmatrix} \eta_0 \\ \eta_{\mathrm{c}} \\ \eta_{\mathrm{s}} \end{Bmatrix} \tag{4.149}$$

4.7 Inflow Dynamics

The inflow dynamics to be used in this model are based on that of Pitt and Peters [53]. It is a linear unsteady theory derived from actuator disk theory, that relates transient rotor loads to induced flow field response. The induced flow is expressed as

$$\lambda = \lambda_0 + \lambda_{\mathrm{c}}\overline{r}\cos\psi + \lambda_{\mathrm{s}}\overline{r}\sin\psi\ , \tag{4.150}$$

where λ_0, λ_{c}, and λ_{s} are the magnitudes of the uniform, fore-to-aft, and side-to-side variations in induced flow, respectively. The induced flow distributions are related to the perturbations in thrust, pitch moment, and roll moment by the linear first-order relation

$$\left[M\right]\begin{Bmatrix}\dot{\lambda}_0\\ \dot{\lambda}_c\\ \dot{\lambda}_s\end{Bmatrix}+\left[L\right]^{-1}\begin{Bmatrix}\lambda_0\\ \lambda_c\\ \lambda_s\end{Bmatrix}=\begin{Bmatrix}C_T\\ C_M\\ C_L\end{Bmatrix}, \tag{4.151}$$

where the x-axis is positive aft, the y-axis is positive starboard, and the z-axis is positive upward. (Note that the order and orientation of these loads differ slightly from that of Pitt and Peters.) The L and M matrices have been solved in closed form in Reference [53]. With appropriate modifications for the new orientation, the L and M matrices are

$$[L]=\frac{1}{v_P}\begin{bmatrix}\frac{1}{2} & \frac{15\pi}{64}\sqrt{\frac{1-\sin\alpha_d}{1+\sin\alpha_d}} & 0\\ \frac{15\pi}{64}\sqrt{\frac{1-\sin\alpha_d}{1+\sin\alpha_d}} & \frac{-4\sin\alpha_d}{1+\sin\alpha_d} & 0\\ 0 & 0 & \frac{4}{1+\sin\alpha_d}\end{bmatrix}, \tag{4.152}$$

$$[M]=\begin{bmatrix}\frac{128}{75\pi} & 0 & 0\\ 0 & \frac{-16}{45\pi} & 0\\ 0 & 0 & \frac{16}{45\pi}\end{bmatrix}, \tag{4.153}$$

respectively, where α_d is the angle of the rotor disk with respect to the free stream velocity. The mass flow parameter for the steady lift case is

$$v_P=\frac{\mu^2+(\lambda_f+\lambda_i)(\lambda_f+2\lambda_i)}{\sqrt{\mu^2+(\lambda_f+\lambda_i)^2}}\,. \tag{4.154}$$

If the helicopter is in axial flight, the induced inflow ratio may be approximated by momentum theory [34, pg. 52] as

$$\lambda_i=\frac{\lambda_c}{2}+\sqrt{(\frac{\lambda_c}{2})^2+\frac{C_T}{2}}\,, \tag{4.155}$$

where λ_c is the vertical climb velocity. Note that in hover, $\lambda_c=0$, and

$$\lambda_i=\sqrt{\frac{C_T}{2}}\,. \tag{4.156}$$

If the helicopter is flying at some angle of incidence, then the induced inflow velocity is governed by the equations

$$\lambda_{\mathrm{i}} = \frac{C_T}{2\sqrt{\mu^2 + \lambda^2}} \,, \tag{4.157}$$

and

$$\lambda = \mu \tan \alpha_{\mathrm{d}} + \lambda_{\mathrm{i}} \,, \tag{4.158}$$

which may be solved iteratively. If an initial inflow is assumed, so that

$$\lambda = \mu \tan \alpha_{\mathrm{d}} + \frac{C_T}{2\sqrt{\mu^2 + \frac{C_T}{2}}} \,, \tag{4.159}$$

the solution will converge after several iterations [34, pg. 61]. Pitt and Peters have shown that in axial flight, the inflow gains are identical to those obtained from simple momentum theory, and are independent of the radial lift distribution. Furthermore, the three degree of freedom dynamic inflow model is usually adequate for rotary wing dynamics.

4.8 State Space Model

The matrices governing the dynamics of the helicopter rotor and the resultant forces of interest were derived in Sections 4.4, 4.5, and 4.6. These matrices have been labeled in Appendix B for convenience. In addition, defining the following vectors will simplify the notation of the state space model:

$$\underline{\beta} = \begin{Bmatrix} \beta_0 \\ \beta_{\mathrm{c}} \\ \beta_{\mathrm{s}} \end{Bmatrix} , \quad \underline{\theta}_{\mathrm{r}} = \begin{Bmatrix} \theta_{\mathrm{r},0} \\ \theta_{\mathrm{r,c}} \\ \theta_{\mathrm{r,s}} \end{Bmatrix} , \quad \underline{\theta}_{k} = \begin{Bmatrix} \theta_{k,0} \\ \theta_{k,\mathrm{c}} \\ \theta_{k,\mathrm{s}} \end{Bmatrix} ,$$

$$\underline{\lambda} = \begin{Bmatrix} \lambda_0 \\ \lambda_{\mathrm{c}} \\ \lambda_{\mathrm{s}} \end{Bmatrix} , \quad \underline{\eta} = \begin{Bmatrix} \eta_0 \\ \eta_{\mathrm{c}} \\ \eta_{\mathrm{s}} \end{Bmatrix} , \quad \underline{C} = \begin{Bmatrix} C_T \\ C_M \\ C_L \end{Bmatrix} . \tag{4.160}$$

The equations of motion derived in the previous Sections may be rewritten using the new notation, and are easily manipulated. The flapping dynamics become

$$\Delta_3\ddot{\underline{\beta}} + \Delta_2\dot{\underline{\beta}} + \Delta_1\underline{\beta} = \Lambda_1\underline{\beta} + \Lambda_2\dot{\underline{\beta}} + \Lambda_3\underline{\boldsymbol{\theta}}_r + \Lambda_{4k}\underline{\boldsymbol{\theta}}_k + \Lambda_5\underline{\lambda} + \Lambda_6\underline{\eta}\,, \tag{4.161}$$

or equivalently,

$$\begin{aligned}\ddot{\underline{\beta}} = {} & \Delta_3^{-1}(\Lambda_1 - \Delta_1)\underline{\beta} + \Delta_3^{-1}(\Lambda_2 - \Delta_2)\dot{\underline{\beta}} + \Delta_3^{-1}\Lambda_3\underline{\boldsymbol{\theta}}_r + \Delta_3^{-1}\Lambda_{4k}\underline{\boldsymbol{\theta}}_k \\ & + \Delta_3^{-1}\Lambda_5\underline{\lambda} + \Delta_3^{-1}\Lambda_6\underline{\eta}\,.\end{aligned} \tag{4.162}$$

The torsion equation is

$$\begin{aligned}\Delta_{6k}\ddot{\underline{\boldsymbol{\theta}}}_k + \Delta_{5k}\dot{\underline{\boldsymbol{\theta}}}_k + \Delta_{4k}\underline{\boldsymbol{\theta}}_k = {} & \Phi_{1k}\underline{\boldsymbol{\theta}}_r + \Phi_{2k}\underline{\boldsymbol{\theta}}_k + \Psi_{1k}\underline{\boldsymbol{\theta}}_r + \Psi_{2k}\dot{\underline{\boldsymbol{\theta}}}_r + \Psi_{3k}\ddot{\underline{\boldsymbol{\theta}}}_r \\ & + \Lambda_{7k}\underline{\boldsymbol{\theta}}_k + \Lambda_{8k}\dot{\underline{\boldsymbol{\theta}}}_k + \Lambda_{9k}\underline{\eta}\,,\end{aligned} \tag{4.163}$$

or equivalently,

$$\begin{aligned}\ddot{\underline{\boldsymbol{\theta}}}_k = {} & \Delta_{6k}^{-1}(\Phi_{1k} + \Psi_{1k})\underline{\boldsymbol{\theta}}_r + \Delta_{6k}^{-1}\Psi_{2k}\dot{\underline{\boldsymbol{\theta}}}_r + \Delta_{6k}^{-1}\Psi_{3k}\ddot{\underline{\boldsymbol{\theta}}}_r + \Delta_{6k}^{-1}(\Phi_{2k} + \Lambda_{7k} - \Delta_{4k})\underline{\boldsymbol{\theta}}_k \\ & + \Delta_{6k}^{-1}(\Lambda_{8k} - \Delta_{5k})\dot{\underline{\boldsymbol{\theta}}}_k + \Delta_{6k}^{-1}\Lambda_{9k}\underline{\eta}\,.\end{aligned} \tag{4.164}$$

The inflow dynamics are

$$M\dot{\underline{\lambda}} + L^{-1}\underline{\lambda} = \underline{C}\,, \tag{4.165}$$

or equivalently,

$$\dot{\underline{\lambda}} = -M^{-1}L^{-1}\underline{\lambda} + M^{-1}\underline{C}\,. \tag{4.166}$$

Finally, the hub reactions are

$$\left\{\begin{matrix} C_T \\ C_M \\ C_L \end{matrix}\right\} = \Gamma_1\underline{\beta} + \Gamma_2\dot{\underline{\beta}} + \Gamma_3\ddot{\underline{\beta}} + \Gamma_4\underline{\boldsymbol{\theta}}_r + \Gamma_{5k}\underline{\boldsymbol{\theta}}_k + \Gamma_6\underline{\lambda} + \Gamma_7\underline{\eta}\,. \tag{4.167}$$

Equation (4.162) can be substituted for $\ddot{\underline{\beta}}$ in the hub reaction expression to give

$$\begin{aligned}\left\{\begin{matrix} C_T \\ C_M \\ C_L \end{matrix}\right\} = & \left(\Gamma_1 + \Gamma_3\Delta_3^{-1}(\Lambda_1 - \Delta_1)\right)\underline{\beta} \ + \left(\Gamma_2 + \Gamma_3\Delta_3^{-1}(\Lambda_2 - \Delta_2)\right)\dot{\underline{\beta}} \\ & + \left(\Gamma_4 + \Gamma_3\Delta_3^{-1}\Lambda_3\right)\underline{\theta_r} \ + \left(\Gamma_{5k} + \Gamma_3\Delta_3^{-1}\Lambda_{4k}\right)\underline{\theta_k} \ + \left(\Gamma_6 + \Gamma_3\Delta_3^{-1}\Lambda_5\right)\underline{\lambda} \\ & + \left(\Gamma_7 + \Gamma_3\Delta_3^{-1}\Lambda_6\right)\underline{\eta}\,. \end{aligned} \tag{4.168}$$

The governing equations of motion for the rotor disk may now be written in state space matrix form. The rotor degrees of freedom are the state variables, while the root pitch actuation and servoflap actuation are control inputs, and the hub reactions serve as inputs to the inflow dynamics. The state space equations for the dynamics of the rotor disk modes and the corresponding hub loads appear in Tables 4.1 and 4.2. The state vector $\underline{x}$ and the control vector $\underline{u}$ are defined as

$$\underline{x} = \left\{\begin{matrix} \underline{\beta} \\ \dot{\underline{\beta}} \\ \underline{\theta_r} \\ \dot{\underline{\theta_r}} \\ \underline{\theta_k} \\ \dot{\underline{\theta_k}} \\ \underline{\lambda} \end{matrix}\right\}, \qquad \underline{u} = \left\{\begin{matrix} \ddot{\underline{\theta_r}} \\ \underline{\eta} \\ \underline{C} \end{matrix}\right\}, \tag{4.169}$$

so that the state space equations representing the dynamics of the rotor disk have the familiar form

$$\begin{aligned} \dot{\underline{x}} &= A\underline{x} + B\underline{u} \\ \underline{y} &= C\underline{x} + D\underline{u}\,. \end{aligned} \tag{4.170}$$

The aerodynamic rotor loads serve as inputs to the inflow model, and the aerodynamic loop can be closed by selecting a G and F matrix, so that

$$\underline{u} = G\underline{y} + F\underline{\tilde{u}}\,, \tag{4.171}$$

where $\underline{\tilde{u}}$ includes only the pitch and servoflap controls. This may be accomplished by

Table 4.1: State space equation for the dynamics of the rotor disk modes, $\underline{\dot{x}} = A\underline{x} + B\underline{u}$.

$$\left\{\begin{matrix} \underline{\dot{\beta}} \\ \underline{\ddot{\beta}} \\ \underline{\dot{\theta}}_{\mathrm{r}} \\ \underline{\ddot{\theta}}_{\mathrm{r}} \\ \underline{\dot{\theta}}_{k} \\ \underline{\ddot{\theta}}_{k} \\ \underline{\dot{\lambda}} \end{matrix}\right\} = \begin{bmatrix} 0 & I & 0 & 0 & 0 & 0 & 0 \\ \Delta_3^{-1}(\Lambda_1 - \Delta_1) & \Delta_3^{-1}(\Lambda_2 - \Delta_2) & \Delta_3^{-1}\Lambda_3 & 0 & \Delta_3^{-1}\Lambda_{4k} & 0 & \Delta_3^{-1}\Lambda_5 \\ 0 & 0 & 0 & I & 0 & 0 & 0 \\ 0 & 0 & 0 & 0 & 0 & 0 & 0 \\ 0 & 0 & 0 & 0 & 0 & I & 0 \\ 0 & 0 & \Delta_{6k}^{-1}(\Phi_{1k} + \Psi_{1k}) & \Delta_{6k}^{-1}\Psi_{2k} & \Delta_{6k}^{-1}(\Phi_{2k} + \Lambda_{7k} - \Delta_{4k}) & \Delta_{6k}^{-1}(\Lambda_{8k} - \Delta_{5k}) & 0 \\ 0 & 0 & 0 & 0 & 0 & 0 & -M^{-1}L^{-1} \end{bmatrix} \left\{\begin{matrix} \underline{\beta} \\ \underline{\dot{\beta}} \\ \underline{\theta}_{\mathrm{r}} \\ \underline{\dot{\theta}}_{\mathrm{r}} \\ \underline{\theta}_{k} \\ \underline{\dot{\theta}}_{k} \\ \underline{\lambda} \end{matrix}\right\}$$

$$+ \begin{bmatrix} 0 & 0 & 0 \\ 0 & \Delta_3^{-1}\Lambda_6 & 0 \\ 0 & 0 & 0 \\ I & 0 & 0 \\ 0 & 0 & 0 \\ \Delta_{6k}^{-1}\Psi_{3k} & \Delta_{6k}^{-1}\Lambda_{9k} & 0 \\ 0 & 0 & M^{-1} \end{bmatrix} \left\{\begin{matrix} \underline{\ddot{\theta}}_{\mathrm{r}} \\ \underline{\eta} \\ \underline{C} \end{matrix}\right\}$$

Table 4.2: State space equation for the hub loads, $\underline{y} = C\underline{x} + D\underline{u}$.

$$\left\{ \begin{matrix} C_T \\ C_M \\ C_L \end{matrix} \right\} = \left[(\Gamma_1 + \Gamma_3\Delta_3^{-1}(\Lambda_1 - \Delta_1)) \;\; (\Gamma_2 + \Gamma_3\Delta_3^{-1}(\Lambda_2 - \Delta_2)) \;\; (\Gamma_4 + \Gamma_3\Delta_3^{-1}\Lambda_3) \;\; 0 \;\; (\Gamma_{5k} + \Gamma_3\Delta_3^{-1}\Lambda_{4k}) \;\; 0 \;\; (\Gamma_6 + \Gamma_3\Delta_3^{-1}\Lambda_5) \right] \left\{ \begin{matrix} \underline{\beta} \\ \underline{\dot{\beta}} \\ \underline{\theta}_r \\ \underline{\dot{\theta}}_r \\ \underline{\theta}_k \\ \underline{\dot{\theta}}_k \\ \underline{\lambda} \end{matrix} \right\}$$

$$+ \left[0 \;\; (\Gamma_7 + \Gamma_3\Delta_3^{-1}\Lambda_6) \;\; 0 \right] \left\{ \begin{matrix} \underline{\ddot{\theta}}_r \\ \underline{\eta} \\ \underline{C} \end{matrix} \right\}$$

choosing

$$G = \begin{bmatrix} 0 \\ 0 \\ I \end{bmatrix} , \qquad \text{and} \qquad F = \begin{bmatrix} I & 0 \\ 0 & I \\ 0 & 0 \end{bmatrix} . \tag{4.172}$$

Closing the aerodynamic loop gives

$$\begin{aligned} \dot{\underline{x}} &= (A + BGC)\underline{x} + (BGDF + BF)\tilde{\underline{u}} \\ \underline{y} &= C\underline{x} + (DF)\tilde{\underline{u}} , \end{aligned} \tag{4.173}$$

where the new control vector is

$$\tilde{\underline{u}} = \begin{Bmatrix} \ddot{\underline{\theta}}_{\mathrm{r}} \\ \underline{\eta} \end{Bmatrix} . \tag{4.174}$$

If new state space matrices are defined, so that

$$\tilde{A} = (A + BGC) , \tag{4.175}$$

$$\tilde{B} = (BGDF + BF) , \tag{4.176}$$

$$\tilde{C} = C , \tag{4.177}$$

$$\tilde{D} = DF , \tag{4.178}$$

then the equations simplify to

$$\begin{aligned} \dot{\underline{x}} &= \tilde{A}\underline{x} + \tilde{B}\tilde{\underline{u}} \\ \underline{y} &= \tilde{C}\underline{x} + \tilde{D}\tilde{\underline{u}} . \end{aligned} \tag{4.179}$$

Therefore, the dynamics of the rotor disk modes can be expressed in state space matrix form, where multiblade coordinates are used for the state variables, control inputs, and hub load outputs. The dynamics include both structural and aerodynamic effects. The inputs to the model are the root pitch accelerations $\ddot{\theta}_{\mathrm{r,0}}$, $\ddot{\theta}_{\mathrm{r,c}}$, $\ddot{\theta}_{\mathrm{r,s}}$ and the collective and cyclic servoflap inputs η_0, η_c, and η_s . The outputs of the model are the thrust, pitch and roll coefficients, C_T, C_M and C_L respectively.

The collective and cyclic root pitch controls $\theta_{r,0}$, $\theta_{r,c}$ and $\theta_{r,s}$ may be twice differentiated in order to obtain the pitch accelerations. In addition, the state output matrix $\tilde{C}$ and control output matrix $\tilde{D}$ may be suitably modified to obtain other outputs from the state space model. Finally, closed-loop control techniques that are applicable to linear systems may be investigated.

In the next Chapter, the state space model will be exercised in order to determine the effect of root pitch control and servoflap actuation on higher harmonic loads, and a comparison of servoflap deflections and root pitch amplitudes that are required for higher harmonic control will be made. The servoflap amplitudes required for higher harmonic control should indicate the feasibility of piezoelectric actuation for that purpose.

Chapter 5

State Space Rotor Model Results

In order to validate the state space model derived in the previous chapter, initial results were compared with those of the C-60 aeroelastic rotor analysis program obtained from Boeing Helicopters. The dynamic response of the blades and rotor thrust were compared for a generic rotor with typical nondimensional parameters taken from Johnson [34]. A final analysis was performed for the H-34 research rotor to determine the effectiveness of servoflap actuation as well as root pitch actuation for conventional collective control and higher harmonic control. The analysis includes the effect of blade torsional stiffness, advance ratio, and spanwise servoflap size and placement. The state space rotor model was coded in Matlab [42], and run on a DEC-3100 workstation.

5.1 C-60 Aeroelastic Rotor Analysis Program

The C-60 aeroelastic rotor analysis program was originally formulated in the 1960's by the Boeing Helicopter Company. It has been continuously developed since then to reflect improvements in computer hardware and helicopter theory. The C-60 program can be used to calculate rotor trim, rotor performance, blade loads and motions, control system loads, fixed and rotating hub loads, and fuselage vibrations. Airloads are calculated in the time domain with azimuthal increments as small as 1 deg, while the dynamic response is obtained using a Fourier series representation with the transfer matrix method. The solution is limited to steady flight condition and constant rotation rate. Nonlinearities and weak couplings are taken into account through an iterative manner.

The blade is modelled as a lumped mass system with up to 50 discrete masses, with aerodynamic loads which may act on up to 40 of the masses. The aerodynamic loads are calculated via a modified lifting line theory with airfoil tables that account for the static two-dimensional effects of airfoil section geometry. The aerodynamic tables are corrected to account for three dimensional flow, unsteady aerodynamics, tab deflections, Reynolds number, Mach relief and stall. The flow field can include uniform or nonuniform downwash with discrete blade-vortex interactions.

The original C-60 program was modified by Boeing to include the effect of a trailing edge servoflap, for this research effort. This was accomplished by including aerodynamic tables for the increments in lift, drag and moment due to the servoflap. In all other respects, the C-60 model was simplified in order to validate the state space rotor model. The aerodynamics were simplified to incorporate a constant lift curve slope, and no downwash. Elastic bending was eliminated to provide only rigid flapping in the out of plane direction, but elastic torsion was included. The center of mass, aerodynamic center, and elastic axis were specified to coincide, and no pitch/flap coupling was included.

5.2 Validation of the State Space Rotor Model

Using the C-60 aeroelastic rotor analysis program, the state space rotor model was validated for a generic rotor with typical rotor parameters taken from Johnson [34]. The *generic rotor* was a 4-bladed semi-articulated rotor model, with rigid blade flapping (no flapwise bending) and no lag motion. The normalized flap hinge offset was $\bar{e} = 0.05$. The first two torsion modes were included in the generic rotor model, as well as a rigid pitch mode. The modal frequency for the first torsion was $\bar{\omega}_1 = 4.50$, placing the second torsion at $\bar{\omega}_2 = 13.50$. Both root pitch actuation and servoflap actuation were incorporated into the model. The servoflap was centered about the

75% spanwise location, and was sized to 20% of the blade span, and 20% of the blade chord. Linear aerodynamics were assumed, with a constant lift curve slope $C_{l_\alpha} = a$, a constant servoflap lift increment $C_{l_\eta} = n$, and a constant moment increment $C_{m_\eta} = p$ about the 1/4 chord. Typical aerodynamic values were taken for a NACA-0012 airfoil section. Since the state space model and C-60 program do not incorporate the same inflow model, the inflow was assumed to be zero for the purpose of comparison.

The discrete mass model of the C-60 rotor program was tailored to have constant spanwise properties (i.e., identical properties for each of the discrete masses), and approximately the same characteristics as the state space model. Nineteen discrete masses and a flapping hinge, each spanning 5% of the total blade span, were assumed. A comparison of the state space model properties and the C-60 properties appear in Table 5.1.

Note that the C-60 model has 19 elastic torsion modes, because it has 19 discrete masses; however, the state space model includes only the first two elastic torsion modes. The differences in dynamic blade response should be rather small, since the N/rev response will generally be dominated by the first mode. Torsionally soft blades may require an additional mode in order to obtain an accurate structural response, but the blade loading is insensitive to small differences in blade twist that accompany the inclusion of additional torsion modes. Although the first torsional frequency of the two models is the same, the inertias vary slightly due to discretization. Since the emphasis of higher harmonic control is at the N/rev frequency, the inclusion of two torsion modes is sufficient.

Since the C-60 program uses the transfer matrix method, the rotor response can only be obtained for frequencies at multiples of the blade passage frequency, including steady state. Furthermore, C-60 retains only 10 harmonics, so the frequency response magnitudes can only be obtained for three points, namely 0/rev, 4/rev and 8/rev. The state space model can generate continuous transfer functions over all frequencies and thereby provide more information about the rotor dynamics.

Initially, the dynamic response of the blades and rotor thrust for the two models were compared for a case that only included elastic twist. Since structural or aero-

Table 5.1: Parameter comparison of the state space model and C-60 program for the generic rotor.

Properties	State Space Model	C-60 Model
Rotor Type	semi-articulated; flapping, no lagging	semi-articulated; flapping, no lagging
Flapping	rigid flapping, no bending	rigid flapping, no bending
Blade Model	continuous; constant properties	discrete mass; 19 identical masses
Torsion	2 elastic modes	19 elastic modes
Nondimensional Parameters		
N	4	4
$\bar{c}$	0.0800	0.0800
$\bar{e}$	0.0500	0.0500
$\bar{r}_1$	0.650	0.650
$\bar{r}_2$	0.850	0.850
a	5.73	5.73
n	3.84	3.84
p	−0.688	−0.688
I^*_β	0.857	0.857
K_β	0.00	0.00
I^*_θ	0.000674	0.000640
$I^*_{\theta_1}$	0.000320	0.000321
$I^*_{\theta_2}$	0.000320	0.000325
$\bar{\omega}_1$	4.50	4.50
$\bar{\omega}_2$	13.50	13.47
γ	8.00	8.00
σ	0.102	0.102
C_T/σ	0.100	0.100

dynamic damping on the torsional modes normally introduces phase that obscures the results, the two models were compared for cases without damping. The flapping degree of freedom was constrained, and a uniform (zero) inflow was prescribed. Table 5.2 is a comparison of blade twist and rotor thrust for the state space model and the C-60 program. Very good agreement was observed between the two models, which can be seen in the table.

Differences in the dynamic responses shown in Table 5.2 occur at 4 and 8/rev in general. Some discrepancy is likely at 4/rev, because the 4/rev frequency is very close to the first torsional resonance. The undamped resonance near 4/rev also accounts for the large blade tip deflection at this frequency. Normally, the response will be much smaller due to aerodynamic damping. Some discrepancy between the dynamic response of the two models is also likely at 8/rev, because higher torsion modes begin to influence the response.

A case that included only flapping motion was also run in order to check the flapping response. For the case with only flapping motion, the blade was allowed to flap freely, while the elastic torsion motion was constrained. Once again, the inflow was prescribed to be zero. Table 5.3 is a comparison of the flapping angle and rotor thrust response for the state space model and the C-60 program. Excellent agreement was also observed for this case. In fact, the results appear identical to three significant digits as shown in the table.

The generic rotor and the results of the constrained model that are shown in Tables 5.2 and 5.3, were only used to compare the blade structural response and rotor thrust response for the state space model and C-60 program. Since the blade motions have been constrained, and neither aerodynamic damping nor dynamic inflow has been included, the results shown in Tables 5.2 and 5.3 only apply to these very restricted cases.

Since the state space model includes the assumption that the twist and flap motion of the blades are uncoupled, independent verification of these dynamics should be adequate in order to validate the model. The motions, however, will be coupled by gyroscopic effects and aerodynamic forces in forward flight. Time did not permit a

Table 5.2: Comparison of blade twist and rotor thrust for the state space model and C-60 program for the generic rotor (elastic torsion only).

		State Space Model		C-60 Model	
Actuation Method	Frequency $\times\Omega$	Tip Pitch $\theta_{t,0}$ $\left[\frac{\text{deg}}{\text{deg}}\right]$	Thrust $\Delta C_T/\sigma$ $\left[\frac{1}{\text{deg}}\right]$	Tip Pitch $\theta_{t,0}$ $\left[\frac{\text{deg}}{\text{deg}}\right]$	Thrust $\Delta C_T/\sigma$ $\left[\frac{1}{\text{deg}}\right]$
Root Pitch $\theta_{r,0}$	0	0.94	0.0158	0.94	0.0157
	4	4.60	0.0693	4.60	0.0691
	8	−1.10	−0.0117	−0.80	−0.0117
Servoflap η_0	0	−0.61	−0.0049	−0.59	−0.0048
	4	−2.40	−0.0308	−2.47	−0.0322
	8	0.25	0.0078	0.22	0.0080

Table 5.3: Comparison of flapping angle and rotor thrust for the state space model and C-60 program for the generic rotor (flapping motion only).

		State Space Model		C-60 Model	
Actuation Method	Frequency $\times\Omega$	Flapping β_0 $\left[\frac{\text{deg}}{\text{deg}}\right]$	Thrust $\Delta C_T/\sigma$ $\left[\frac{1}{\text{deg}}\right]$	Flapping β_0 $\left[\frac{\text{deg}}{\text{deg}}\right]$	Thrust $\Delta C_T/\sigma$ $\left[\frac{1}{\text{deg}}\right]$
Root Pitch $\theta_{r,0}$	0	1.01	0.0167	1.01	0.0167
	4	0.07	0.0030	0.07	0.0030
	8	0.02	0.0021	0.02	0.0021
Servoflap η_0	0	0.23	0.0038	0.23	0.0038
	4	0.02	0.0007	0.02	0.0007
	8	0.00	0.0005	0.00	0.0005

full comparison of the coupled dynamics of the rotor for the state space model and the C-60 model, due to the enormous amount of computation time and hardware memory required to run the C-60 program. Nevertheless, independent analysis of the state space model for coupled dynamics gave predictable results, and we have no reason to doubt the validity of the model. The complete state space rotor model including flapping and twist dynamics will be exercised for the H-34 research rotor in the next section.

5.3 Results for the H-34 Research Rotor

The H-34 rotor is a fairly generic 4-bladed rotor model that has been used extensively by NASA and independent rotorcraft manufacturers for wind tunnel rotor research. It has been the subject of many experimental rotorcraft research projects [45, 59, 70, 38] and is well known. Due to its simplicity and familiarity, the H-34 was also used as the prototype for this investigation.

The H-34 rotor blades have a rectangular planform, but do not have constant mass or inertia properties. In order to obtain similar dynamic characteristics, the nondimensional flapping inertia I_β^*, the first torsional inertia $I_{\theta_1}^*$, and the first torsion frequency $\overline{\omega}_1$ were chosen to match those of the discrete mass model provided by Boeing. A comparison of the state space model parameters and the C-60 model parameters for the baseline H-34 rotor appear in Table 5.3.

Although the flapping inertia, first torsional inertia, and first torsion frequency are well matched, there are discrepancies in the torsion frequencies and pitch inertias of the blade for other modes. The discrepancies result from the variation in spanwise mass, inertia, and stiffness of the blade, as well as the discretization in general. Although some differences exist, the state space model should provide an adequate approximation to the blade response, because the state space parameters were chosen to match the dynamics of the flapping mode and first torsion mode of the rotor blades, and the first torsion mode dominates the twist response below the N/rev frequency.

The effectiveness of a trailing edge flap can be significantly reduced by the airfoil's boundary layer, especially for flaps with small flap-to-chord ratios, and for small flap displacements η. In addition, the flap effectiveness can also be influenced by the local angle of attack of the airfoil α. For this reason, the aerodynamic coefficients c_{l_α}, c_{l_η}, and c_{m_η}, were obtained from the 2-dimensional panel code XFOIL [13], which includes the effects of viscosity. The coefficients were obtained for a NACA-0012 airfoil with a 20% flap-to-chord ratio. The 75% radial location was used to obtain a characteristic design point speed, yielding a Reynolds number of 4.08×10^6.

Due to three-dimensional flow effects, blade loading must drop to zero over a finite

Table 5.4: Parameter comparison of the continuous and discrete mass models for the baseline H-34 rotor.

Properties	Continuous Model	Discrete Mass Model
Rotor Type	semi-articulated; flapping, no lagging	semi-articulated; flapping, no lagging
Airfoil Shape	NACA-0012	NACA-0012
Blade Model	continuous; constant properties	discrete mass; 25 masses
Flapping	rigid flapping, no bending	rigid flapping, no bending
Torsion	2 elastic modes	25 elastic modes
Dimensional Parameters		
Rotor Radius, R	28.0 ft	28.0 ft
Rotor Speed, Ω	222 RPM	222 RPM
Gross Weight, W	11,500 lbs	11,500 lbs
Air Density, ρ	0.00220 slug/ft^3	0.00220 slug/ft^3
Nondimensional Parameters		
N	4	4
$\overline{c}$	0.0488	0.0488
$\overline{e}$	0.0357	0.0357
$\overline{r}_1$	0.70	0.70
$\overline{r}_2$	0.90	0.90
a	6.30	6.30
n	3.15	3.15
p	−0.517	−0.517
I_β^*	0.893	0.893
K_β	0.00	0.00
I_θ^*	0.000278	0.000378
$I_{\theta_1}^*$	0.000134	0.000134
$I_{\theta_2}^*$	0.000134	0.000329
$\overline{\omega}_1$	7.65	7.65
$\overline{\omega}_2$	22.94	22.99
γ	8.11	8.11
σ	0.0621	0.0621
C_T	0.00502	0.00502
C_T/σ	0.0808	0.0808

distance near the blade tips, resulting in so-called *tip loss* [34, pg. 59]. One way to approximate the tip loss is to assume that the blade elements outboard of the radial station $\overline{r} = B$ have profile drag but produce no lift. A simple approximation proposed by Wheatley [72] suggests

$$B = 1 - \frac{\overline{c}}{2}\,, \tag{5.1}$$

or that the outer half-chord length of the blade span produces no lift. Tip loss values are typically in the range $B = 0.96$ to 0.98, and Wheatley's approximation gives $B = 0.9756$ for the H-34 rotor. Tip loss can affect rotor thrust by as much as a factor of B^4, and for the H-34 rotor $B^4 = 0.9059$. This implies that tip loss may reduce H-34 rotor thrust by as much as 10%.

Rotor blade tip speeds can approach Mach 1, so that compressibility effects are of particular importance. The compressibility of air can influence both rotor performance and blade motions. It increases the lift curve slope with Mach number, and sharply increases drag and pitching moment above a critical Mach number. The only practical means of accounting for the compressibility effects in detail is to use airfoil data that has been tabulated as a function of Mach number. Since the state space model used in this investigation approximates linear aerodynamics with constant lift curve and moment slopes, compressibility effects were not taken into account in this analysis for simplicity.

Furthermore, a detailed analysis of various flap/chord ratios is beyond the scope of this research, because it would entail tabulated lift and moment coefficients for several flap/chord ratios as a function of Mach number, local angle of attack and Reynolds number. Such an analysis may be more suitable for the C-60 aeroelastic rotor analysis program, because it already contains this information in a tabulated form. In the state space model the effect of the servoflap is specified by constant lift and moment coefficients. Any geometries or aerodynamics that can be approximately described by these constants can be included in the state space model. In this investigation the coefficients were estimated using XFOIL for a flap/chord ratio of 20%, with viscosity effects included. A 20% flap/chord ratio reflects a reasonable servoflap size, and piezoelectric actuation of a servoflap this size should be achievable considering the impedance matching arguments provided by Spangler and Hall [66].

Servoflap effectiveness should improve as the flap is placed closer to the blade tip, since sectional lift increases with radius. In this investigation however, the 90% span location was considered as an upper limit on servoflap placement, because tip loss, Mach effects, and mechanical complexity may limit the proximity of the servoflap to the blade tip in practice. Initially a 20% flap/span ratio was used, and the servoflap was placed from the 70% to 90% blade radius.

The simple dynamic inflow model of Pitt and Peters [53] was used in this investigation. Dynamic inflow will tend to reduce the steady thrust developed by the rotor, because the lift developed by the rotor blades induces a net inflow through the rotor disk. The inflow tends to decrease the apparent angle of attack of the blades, and therefore decreases lift. Since the air itself has inertia, the inflow takes time to respond to the change in rotor thrust. Therefore, dynamic inflow has less effect on rotor thrust for high frequency cycling of blade lift. In Figure 5-1, rotor thrust response due to collective pitch actuation is plotted for several advance ratios. The twist and flapping motion of the blades has been constrained, so that the only dynamics are due to inflow. The thrust response is plotted versus nondimensional frequency $\overline{\omega} = \omega/\Omega$, and the 4/rev frequency has been indicated by a vertical line.

Figure 5-1 shows that dynamic inflow reduces the steady thrust response for the rotor in hover as well as in forward flight. In hover, the steady thrust response is reduced by 30%, while in forward flight the response may be reduced by as much as 70% due to inflow dynamics. Interestingly, a minimum in steady thrust occurs for an advance ratio of $\mu \approx 0.11$. The steady thrust response continuously decreases with advance ratio from $\mu = 0.0$ to 0.11, and then increases. The effect results from the interaction of blade lift and induced flow, and the coupling of collective and lateral cyclic disk modes in forward flight. Although the effect of inflow is small at 4/rev, the inflow dynamics should be included in the state space model in order to get accurate steady thrust responses. The inflow dynamics also add phase in the system, but the effect is minor. At the 4/rev frequency the phase lead amounts to only 3 deg.

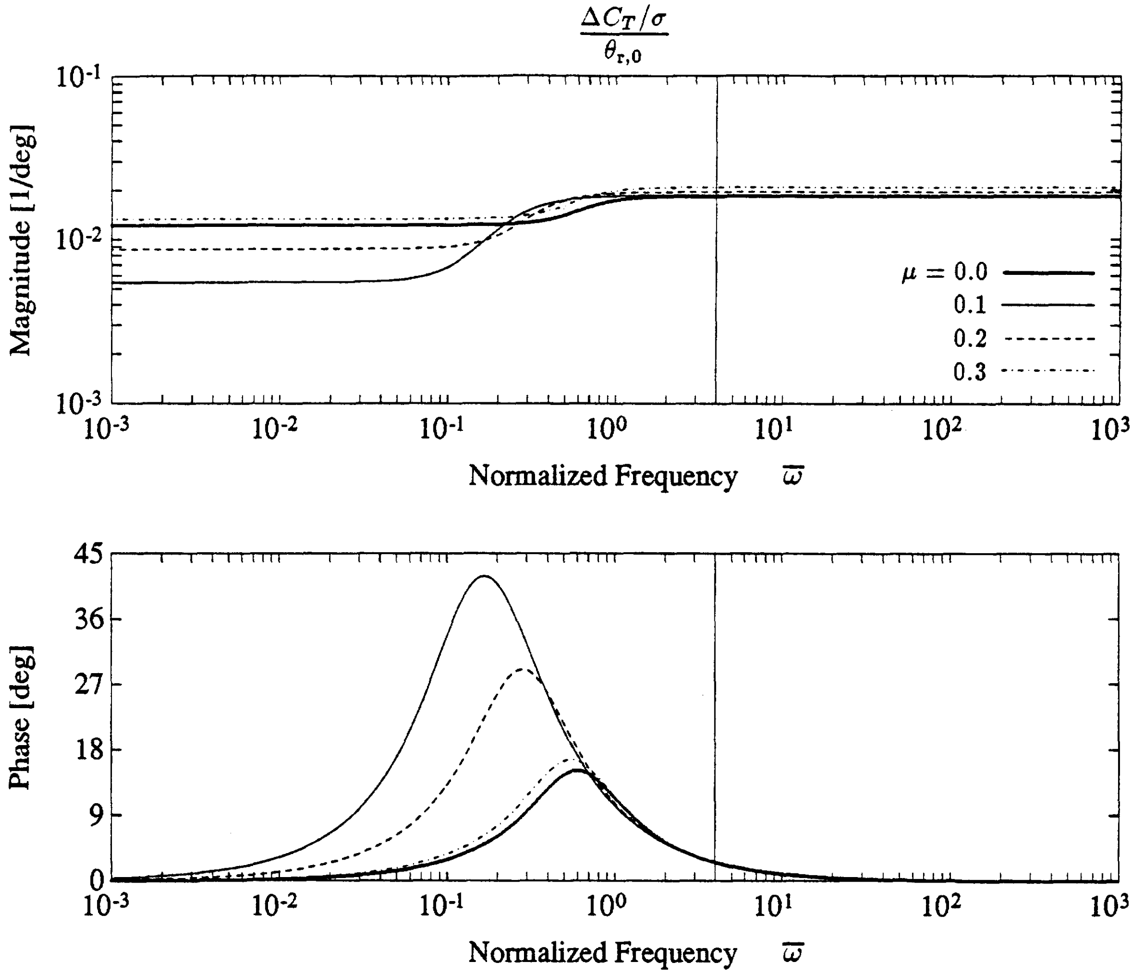

Figure 5-1: Effect of inflow dynamics on thrust response due to collective pitch, for the H-34 rotor in edgewise forward flight for several advance ratios.

A well-designed rotor should have baseline vibration acceleration levels below 0.25 g, at the blade passage frequency. In this study we will assume that 0.25 g is adequate for higher harmonic vibration control, and we will use this number as a goal for servoflap actuation. A good measure of the vibration control authority is the incremental blade loading $\Delta C_T/\sigma$ provided by the controls. Since the total C_T/σ for a hovering rotor corresponds to 1.0 g, the ratio of $\Delta C_T/\sigma$ to C_T/σ needs to be about 0.25, in order to get 0.25 g of vibration control authority.

The effect of aerodynamic controls on the pitch and roll moments, $\Delta C_M/\sigma$ and $\Delta C_L/\sigma$, can also influence the amount of higher harmonic vibration control authority, through inplane hub forces and moments. However, the requirements are less general, and are highly dependent on the particular rotor configuration and the amount of inherent inplane vibration that the design exhibits. Therefore, only the incremental blade loading $\Delta C_T/\sigma$ will be used to measure the effectiveness of servoflap designs for higher harmonic vibration reduction in this study.

Results of the state space model for the baseline H-34 rotor in hover appear in Table 5.5. The table includes the magnitude response for the coning angle (β_0), the collective tip pitch response ($\theta_{\mathrm{t},0}$), the increment in blade loading ($\Delta C_T/\sigma$), and the thrust increment in g's (ΔT), for collective root pitch actuation ($\theta_{\mathrm{r},0}$) and servoflap actuation (η_0). The rotor dynamics include the flapping mode, two elastic torsion modes, and the Pitt and Peters inflow model. The frequency for the first torsion mode is $\overline{\omega}_1 = 7.65$, while the second is at $\overline{\omega}_2 = 22.95$. The servoflap is located from $\overline{r}_1 = 0.70$ to $\overline{r}_2 = 0.90$.

The H-34 rotor has a blade loading in hover of $C_T/\sigma = 0.0808$. Since this corresponds to 1.0 g, the lift increment in the last column of Table 5.5 was computed by dividing $\Delta C_T/\sigma$ by C_T/σ, yielding the thrust increment ΔT in units of g/deg. Although 10 deg of collective pitch can provide a thrust of 1.5 g, collective control is not possible with servoflap actuation for the baseline H-34 rotor.

If acceleration levels on the order of 0.25 g are required for higher harmonic vibration control, then the actuation method must provide a thrust increment of at least $\Delta C_T/\sigma = 0.0202$. Higher harmonic vibration control can be achieved with collective root pitch amplitudes of 4.0 deg; however, HHC through servoflap actuation does not seem possible for the baseline H-34 rotor. If a maximum servoflap deflection of 10 deg is assumed, then only 0.06 g is achievable for servoflap HHC. This result is not surprising, because the baseline H-34 rotor blades are very stiff in torsion. The first torsion frequency of the H-34 rotor blades are 7.65Ω, whereas first torsional frequencies of most rotor blades are between 3Ω and 6Ω.

Since even the torsionally stiff baseline H-34 rotor blade operates in aileron reversal, softening the blade should improve the servoflap authority. This was accomplished by lowering the first torsional frequency of the H-34 blade from 7.65Ω to 4.50Ω, a typical value for moderately stiff blades. This subsequently put the second torsion

Table 5.5: Flapping angle, tip pitch, blade loading, and thrust responses for the baseline H-34 rotor with torsionally stiff blades ($\overline{\omega}_1 = 7.65$).

Actuation Method	Frequency $\times\,\Omega$	$\mid \beta_0 \mid$ $\left[\frac{\text{deg}}{\text{deg}}\right]$	$\mid \theta_{\text{t},0} \mid$ $\left[\frac{\text{deg}}{\text{deg}}\right]$	$\mid \Delta C_T/\sigma \mid$ $\left[\frac{1}{\text{deg}}\right]$	$\mid \Delta T \mid$ $\left[\frac{\text{g}}{\text{deg}}\right]$
Root Pitch $\theta_{\text{r},0}$	0	0.71	0.98	0.0121	0.150
	4	0.10	1.40	0.0050	0.062
	8	0.05	3.16	0.0094	0.116
Servoflap η_0	0	0.02	0.26	0.0004	0.004
	4	0.01	0.34	0.0005	0.006
	8	0.01	0.58	0.0020	0.025

Table 5.6: Flapping angle, tip pitch, blade loading, and thrust responses for the baseline H-34 rotor with moderately stiff blades ($\overline{\omega}_1 = 4.50$).

Actuation Method	Frequency $\times\,\Omega$	$\mid \beta_0 \mid$ $\left[\frac{\text{deg}}{\text{deg}}\right]$	$\mid \theta_{\text{t},0} \mid$ $\left[\frac{\text{deg}}{\text{deg}}\right]$	$\mid \Delta C_T/\sigma \mid$ $\left[\frac{1}{\text{deg}}\right]$	$\mid \Delta T \mid$ $\left[\frac{\text{g}}{\text{deg}}\right]$
Root Pitch $\theta_{\text{r},0}$	0	0.69	0.94	0.0117	0.144
	4	0.13	2.00	0.0073	0.091
	8	0.01	1.00	0.0035	0.043
Servoflap η_0	0	0.33	0.74	0.0053	0.065
	4	0.07	1.12	0.0041	0.051
	8	0.01	0.25	0.0014	0.017

Table 5.7: Flapping angle, tip pitch, blade loading, and thrust responses for the baseline H-34 rotor with torsionally soft blades ($\overline{\omega}_1 = 2.50$).

Actuation Method	Frequency $\times\,\Omega$	$\mid \beta_0 \mid$ $\left[\frac{\text{deg}}{\text{deg}}\right]$	$\mid \theta_{\text{t},0} \mid$ $\left[\frac{\text{deg}}{\text{deg}}\right]$	$\mid \Delta C_T/\sigma \mid$ $\left[\frac{1}{\text{deg}}\right]$	$\mid \Delta T \mid$ $\left[\frac{\text{g}}{\text{deg}}\right]$
Root Pitch $\theta_{\text{r},0}$	0	0.61	0.83	0.0104	0.129
	4	0.07	1.00	0.0036	0.044
	8	0.00	0.79	0.0041	0.050
Servoflap η_0	0	1.29	2.20	0.0201	0.249
	4	0.07	0.91	0.0041	0.051
	8	0.01	0.63	0.0030	0.038

frequency at 13.50Ω.

Table 5.6 lists results for the H-34 rotor with moderately stiff blades ($\overline{\omega}_1 = 4.50$). Softening the blade reduced the steady thrust provided by the collective pitch by only about 3%, while it increased the collective servoflap authority by an order of magnitude. A collective pitch input of 10 deg can still provide 1.44 g of steady thrust, while a collective servoflap input of 10 deg can provide up to 0.65 g. Although the servoflap alone cannot provide collective control, it can certainly be used to augment the primary collective and overcome any loss in thrust incurred by softening the blade.

The H-34 rotor with moderately stiff blades can achieve higher harmonic vibration control with root pitch actuation or servoflap actuation. A collective root pitch input of 2.8 deg is capable of providing 0.25 g for higher harmonic vibration suppression, while a servoflap input of 4.9 deg can achieve the same level. A maximum servoflap deflection of 10 deg can provide up to 0.51 g for HHC.

The Kaman Controllable Twist Rotor (CTR) mentioned in Section 1.3.3 was also based on the H-34 rotor design. Although a conventional pitch horn and swashplate were used to provide primary control, the blade was made very soft in torsion so that the servoflap could be actuated collectively and cyclically to control the blade torsional response. The blade first torsion frequency was placed between 2Ω and 3Ω in order to insure adequate twisting response to servoflap deflection [59].

Results for the H-34 rotor with torsionally soft blades similar to the Kaman CTR rotor blades are presented in Table 5.7. The first torsion frequency was placed at $\overline{\omega}_1 = 2.50$, resulting in a second torsion frequency at $\overline{\omega}_2 = 7.50$. Collective control can now be achieved by either root pitch or servoflap actuation. A collective root pitch input of 10 deg can provide 1.29 g of steady thrust, with a reduction of 14% from the rotor with torsionally stiff blades. A collective servoflap input of 10 deg is no longer realistic, because it would result in a tip pitch of over 22.0 deg. A more realistic servoflap input of 6 deg produces only 13.2 deg of tip twist, and provides nearly 1.5 g of steady thrust. Although collective root pitch authority has been reduced by about 14%, a combination of root pitch actuation and servoflap actuation can still provide more than 2 g of vertical thrust.

With torsionally soft blades, the H-34 rotor will require 5.6 deg of collective root pitch for 0.25 g of higher harmonic vibration control. Servoflap actuation will require a 4.9 deg deflection in order to obtain 0.25 g for HHC. Although softening the H-34 rotor blade from $\overline{\omega}_1 = 2.50$ to 4.50 dramatically increases the steady thrust provided by the servoflap, it does not improve the servoflap's authority to provide higher harmonic control. This may be understood by examining the frequency response plots obtained from the state space model.

The frequency response from collective root pitch input to thrust has been plotted in Figure 5-2 for the various blade torsional stiffnesses. Once again, the thrust response has been plotted versus the normalized frequency $\overline{\omega}$, and the 4/rev frequency has been marked by a vertical line. Resonant peaks can be seen in the thrust response corresponding to the flapping mode and the first two torsion modes. For example, the torsionally stiff blade has peaks near $\overline{\omega} = 1.0$ due to the flapping mode, $\overline{\omega} = 7.65$ due to the first torsion mode, and $\overline{\omega} = 22.95$ due to the second torsion mode. As the torsion frequency decreases the damping ratio increases, so that the magnitude of the torsion peaks tend to decrease with frequency as observed in Figure 5-2. Note that the torsionally soft blade has a first torsion frequency at $\overline{\omega} = 2.50$, but the resonance is almost critically damped by aerodynamics and the thrust response is completely dominated by the flapping mode.

Figure 5-2 also shows that the static thrust response is slightly decreased by softening the blade. As the rotor blade is softened, the total blade pitch will decrease due to the propeller moment produced by centrifugal forces. Although blade pitch will be most reduced outboard, where the majority of lift is developed, the effect is small and may be overcome by augmenting the primary collective control with the servoflap. Softening the blade from $\overline{\omega}_1 = 7.65$ to 2.50 results in only a 14% decrease in the steady thrust provided by the conventional collective.

Higher harmonic vibration control that employs collective pitch cycling may be best achieved by the rotor with moderately stiff blades. At the blade passage frequency the thrust response for the moderately stiff blades is higher than for the stiff or soft blades, as observed in Figure 5-2. Although the pitch motion of the blade is

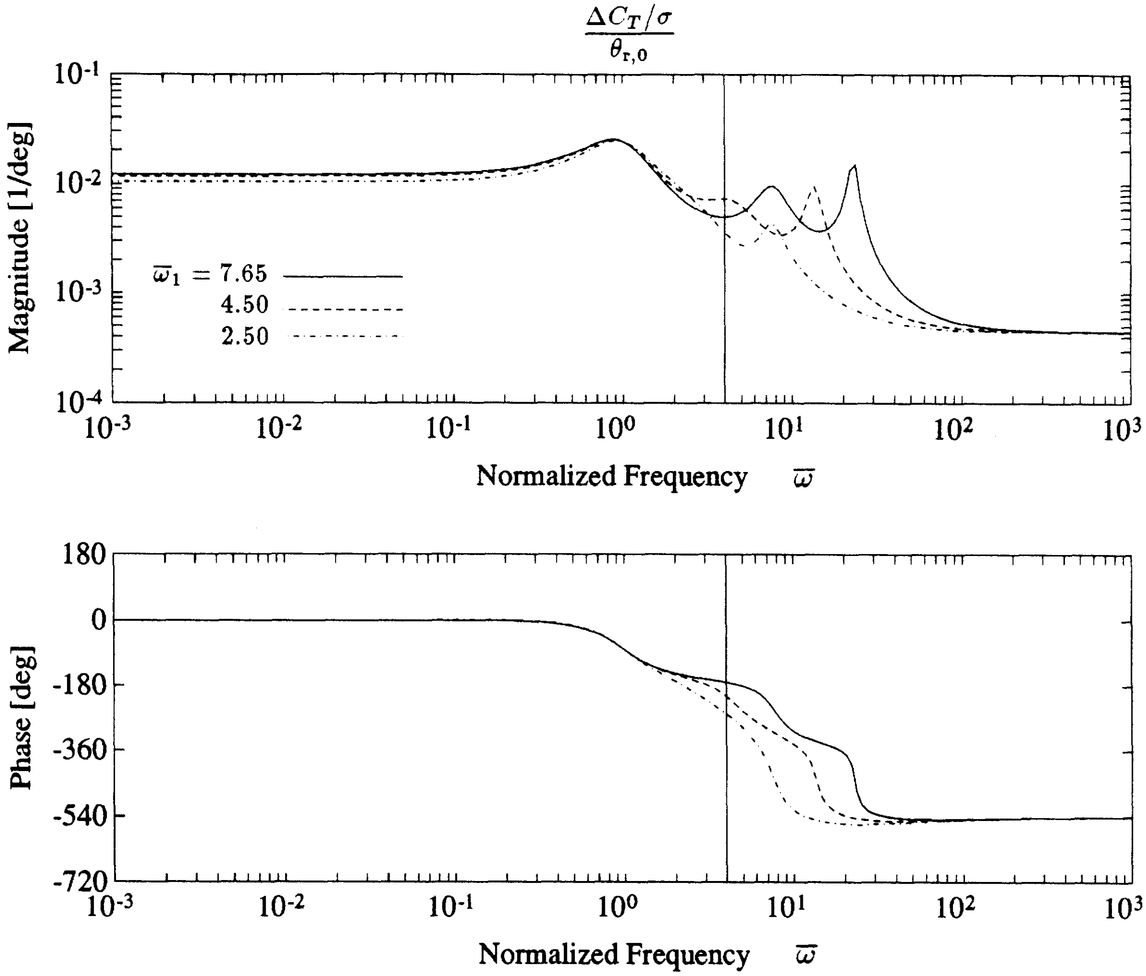

Figure 5-2: The effect of blade torsional stiffness on the thrust response of the hovering H-34 rotor due to collective pitch actuation.

well damped by aerodynamics, the proximity of the first torsion mode to the 4/rev frequency provides a significant benefit. In such cases were resonance occurs near the N/rev frequency, the degree of aerodynamic damping on the mode can have a significant impact on the magnitude of the thrust response for HHC.

The frequency response from collective servoflap input to thrust has been plotted in Figure 5-3 for the various torsional stiffnesses. Once again the thrust response has been plotted versus normalized frequency $\bar{\omega}$, and the 4/rev frequency has been marked by a vertical line. Peaks occur in the thrust response near the frequencies of the flapping mode, and first two torsion modes.

Figure 5-3 shows that for each of the blade stiffnesses the thrust response produced by a static servoflap deflection is 180 deg out of phase. Therefore, even the rotor with

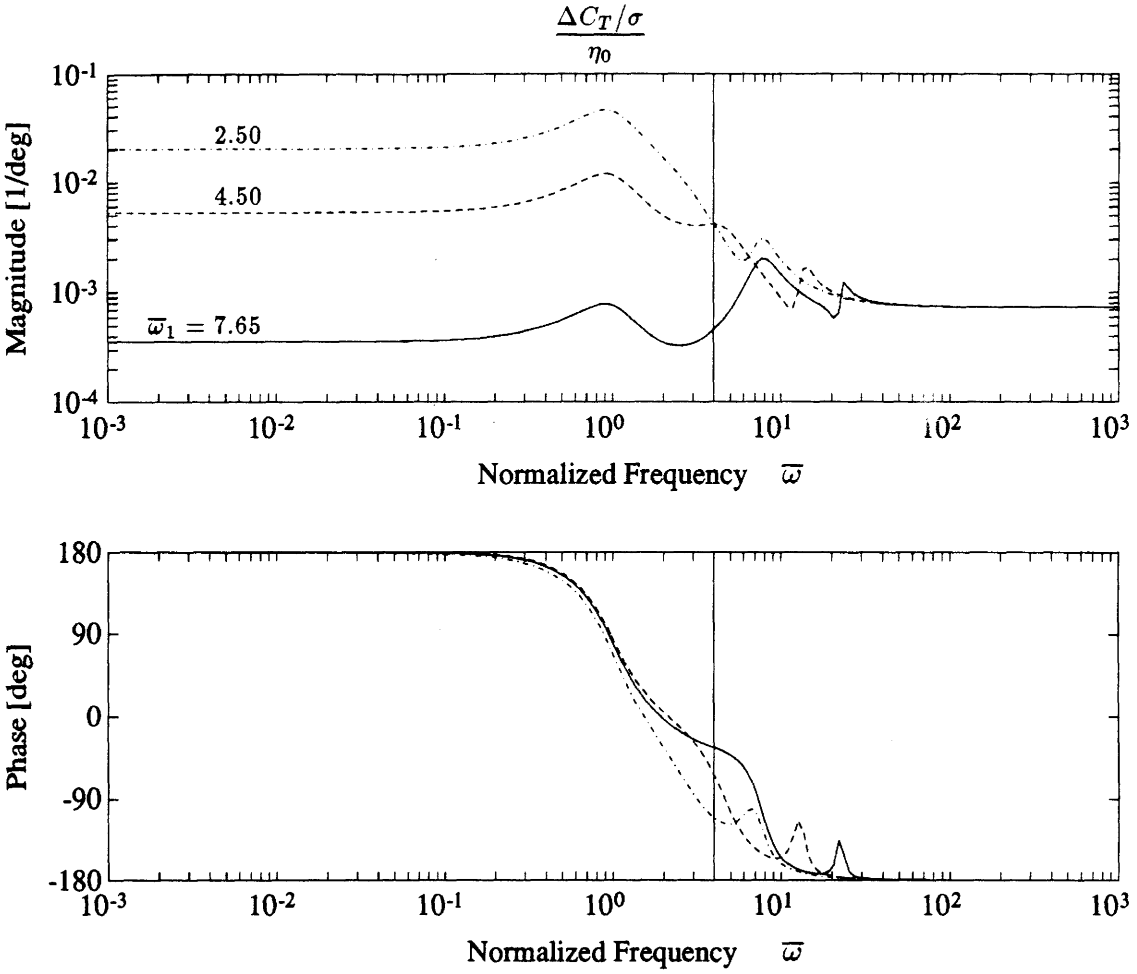

Figure 5-3: The effect of blade torsional stiffness on the thrust response of the hovering H-34 rotor due to collective servoflap actuation.

torsionally stiff blades ($\bar{\omega}_1 = 7.65$) operates in aileron reversal. In fact, the boundary for aileron reversal is $\bar{\omega}_1 \approx 8.2$. The servoflap will operate in aileron reversal for blades softer than $\bar{\omega}_1 = 8.2$, while it will operate conventionally for blades stiffer than $\bar{\omega}_1 = 8.2$. Naturally, this boundary is dependent on blade stiffness, rotor speed, servoflap size and placement, and the lift and moment coefficients.

Figure 5-3 shows that the thrust response for a static servoflap input dramatically increases as the blade torsional stiffness decreases. Since the rotor with torsionally stiff blades operates near the aileron reversal boundary, very little lift is produced by deflecting the servoflap. However, as the blade is softened the moment provided by the servoflap produces more blade twist, thereby increasing thrust. Static servoflap actuation of the rotor with torsionally soft blades ($\bar{\omega}_1 = 2.50$) produces thrust nearly an order of magnitude higher than the thrust produced by the rotor with moderately stiff blades, and thrust two orders of magnitude higher than that for the rotor with torsionally stiff blades.

The ability of the servoflap to produce higher harmonic vibration control is also increased as the blade torsion frequency is lowered. This can be observed by examining the magnitude of the thrust responses at the 4/rev frequency in Figure 5-3. As the first torsional frequency of the blade is lowered from $\overline{\omega}_1 = 7.65$ to 4.50, the magnitude of the thrust response increases by nearly 7.2 times. Interestingly however, as the blade torsion frequency is continually decreased from $\overline{\omega}_1 = 4.50$ to 2.0, the magnitude of the thrust response at 4/rev remains almost constant. Therefore, little benefit is obtained for servoflap higher harmonic control by softening the blade lower than $\overline{\omega}_1 \approx 4.50$.

At the blade passage frequency, 4/rev, servoflap actuation has adequate phase characteristics for all blade stiffnesses. The phase ranges from 0 deg for stiff blades, to -90 deg for soft blades. Conventional root actuation, however, can have poor phase characteristics at the 4/rev frequency for torsionally stiff blades, but the phase improves as the blade is softened. The phase for conventional root actuation ranges from -180 deg for stiff blades, to -270 deg for soft blades at the 4/rev frequency.

The rotor with moderately stiff blades ($\overline{\omega}_1 = 4.50$) will be used for the remainder of this investigation, since it is typical for conventional helicopters, and little benefit is gained by lowering the stiffness below 4.50 for servoflap higher harmonic control. Table 5.8 shows the effect of various spanwise servoflap sizes and locations on rotor thrust for the rotor with moderately stiff blades. The flap size and the inboard and outboard servoflap radial locations have been nondimensionalized by the rotor radius. The inboard and outboard locations are given by $\overline{r}_1$ and $\overline{r}_2$ respectively. The flap size is given by $\overline{r}_{\mathbf{flap}}$, which is the spanwise length of the flap divided by the rotor radius, or equivalently $\overline{r}_2 - \overline{r}_1$. The increment in blade loading $\Delta C_T/\sigma$ due to a servoflap deflection is given at steady state (0/rev), and at the blade passage frequency (4/rev). In addition, thrust is expressed in g's per degree of servoflap deflection.

A 20% servoflap was placed at several outboard radial locations. Not surprisingly,

Table 5.8: The effect of spanwise servoflap size and placement on the thrust response of the H-34 rotor in hover, for collective servoflap actuation.

Servoflap			Static Response 0/rev		HHC Response 4/rev	
			Loading	Thrust	Loading	Thrust
$\bar{r}_{\text{flap}}$	$\bar{r}_1$	$\bar{r}_2$	$\left\lvert\frac{\Delta C_T}{\sigma}\right\rvert$ $\left[\frac{1}{\text{deg}}\right]$	$\lvert \Delta T \rvert$ $\left[\frac{\text{g}}{\text{deg}}\right]$	$\left\lvert\frac{\Delta C_T}{\sigma}\right\rvert$ $\left[\frac{1}{\text{deg}}\right]$	$\lvert \Delta T \rvert$ $\left[\frac{\text{g}}{\text{deg}}\right]$
0.20	0.55	0.75	0.0028	0.035	0.0026	0.032
”	0.60	0.80	0.0036	0.044	0.0031	0.038
”	0.65	0.85	0.0044	0.054	0.0036	0.044
”	0.70	0.90	0.0053	0.065	0.0041	0.051
0.10	0.80	0.90	0.0031	0.038	0.0023	0.029
0.15	0.75	0.90	0.0043	0.053	0.0033	0.040
0.20	0.70	0.90	0.0053	0.065	0.0041	0.051
0.25	0.65	0.90	0.0061	0.075	0.0048	0.060
0.30	0.60	0.90	0.0067	0.083	0.0054	0.066
0.40	0.50	0.90	0.0075	0.092	0.0062	0.077
0.50	0.40	0.90	0.0078	0.097	0.0067	0.083
0.60	0.30	0.90	0.0079	0.098	0.0070	0.087

blade loading increases with the servoflap's radial location. As mentioned earlier, it might not be feasible to put the outboard servoflap location past about $\bar{r}_2 = 0.9$, so the baseline H-34 rotor has a 20% servoflap located from $\bar{r}_1 = 0.70$ to $\bar{r}_2 = 0.90$. This servoflap configuration can provide 0.25 g at 4/rev with a servoflap deflection of $\eta_0 = 4.9$ deg, for the rotor with moderately stiff blades.

Since it is apparent that the servoflap should be placed as far outboard as practically feasible, the maximum outboard location $\bar{r}_2 = 0.90$ was held constant while several servoflap sizes were investigated. Certainly increasing the servoflap size will improve the thrust response; however, the presence of a servoflap inboard of $\bar{r} = 0.50$ was found to add very little to the incremental blade loading $\Delta C_T/\sigma$, as indicated by the table. This is not surprising, because the sectional blade lift is proportional to the square of the radius. Although a 20% servoflap located from $\overline{r}_1 = 0.70$ to $\overline{r}_2 = 0.90$ should be adequate for HHC, a 40% spanwise flap can improve the thrust response by almost 50%; however, increasing the servoflap span any larger will add little to the thrust.

The effect of advance ratio on the thrust response of the H-34 rotor with moderately stiff blades was examined for root pitch actuation and servoflap actuation. A rotor disk angle of $\alpha_d = 0$ was prescribed, which corresponds to the rotor in edgewise forward flight. Responses for the baseline H-34 rotor were examined for advance ratios from 0.0 to 0.3.

The effect of advance ratio on the thrust response due to collective pitch is summarized in Figure 5-4 and Table 5.9. The data suggests that advance ratio has very little effect on the thrust response due to higher harmonic pitch cycling at 4/rev. In fact, the thrust response at 4/rev decreases by less than 10% as the advance ratio is increased from 0.0 to 0.3; however, the steady response at 0/rev can decrease by more than 55% with advance ratio.

In the low frequency range the variation in thrust response due to advance ratio is primarily governed by the inflow dynamics. In the absence of inflow, the steady thrust response due to collective pitch will increase slightly with advance ratio; however, with the Pitt and Peters' dynamic inflow model [53] the steady thrust response exhibits a minimum for $\mu \approx 0.11$. Although the thrust response at 4/rev reduces only slightly with advance ratio, the steady response may vary significantly.

The effect of advance ratio on the thrust response due to servoflap actuation is summarized in Figure 5-5 and Table 5.10. This data suggests that advance ratio also has very little effect on the thrust response due servoflap actuation at 4/rev. The thrust response increases by only 6% as the advance ratio is increased from 0.0 to 0.3.

Once again, the steady thrust response exhibits a minimum at $\mu \approx 0.11$. This is not surprising, because the same inflow mechanism that produces this effect for pitch actuation produces the effect for servoflap actuation. The steady thrust response for servoflap actuation may increase or decrease by as much as 50% with advance ratio.

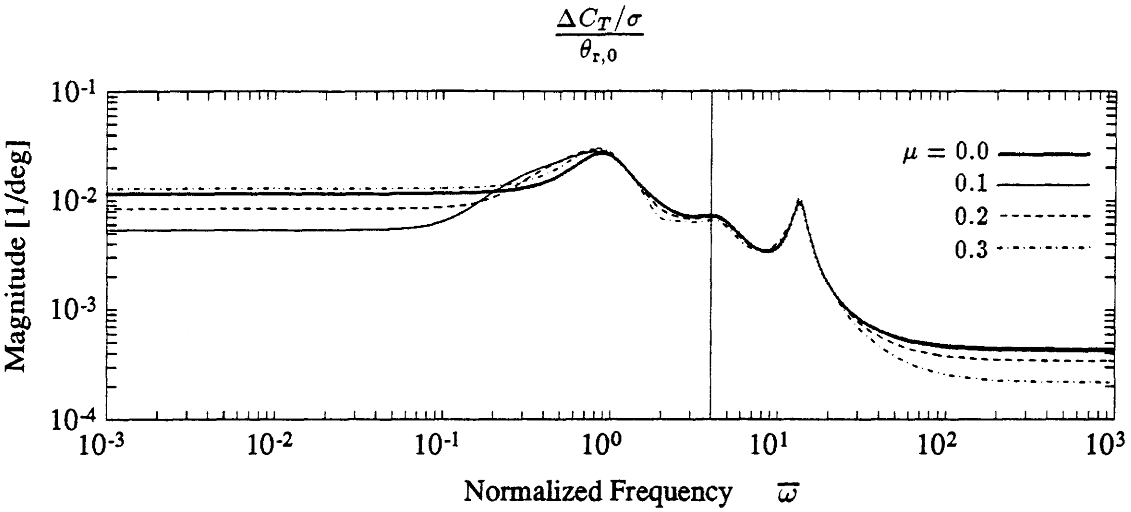

Figure 5-4: The effect of advance ratio on thrust response due to collective pitch actuation for the H-34 rotor in edgewise forward flight.

Advance Ratio μ	Static Response 0/rev Loading $\lvert\Delta C_T/\sigma\rvert$ $\left[\frac{1}{\text{deg}}\right]$	Static Response 0/rev Thrust $\lvert\Delta T\rvert$ $\left[\frac{\text{g}}{\text{deg}}\right]$	HHC Response 4/rev Loading $\lvert\Delta C_T/\sigma\rvert$ $\left[\frac{1}{\text{deg}}\right]$	HHC Response 4/rev Thrust $\lvert\Delta T\rvert$ $\left[\frac{\text{g}}{\text{deg}}\right]$
0.00	0.0117	0.144	0.0073	0.091
0.05	0.0089	0.110	0.0073	0.090
0.10	0.0053	0.066	0.0072	0.090
0.15	0.0062	0.077	0.0071	0.088
0.20	0.0085	0.105	0.0070	0.086
0.25	0.0107	0.133	0.0068	0.084
0.30	0.0128	0.159	0.0066	0.081

Table 5.9: The effect of advance ratio on thrust response due to collective pitch actuation for the H-34 rotor in edgewise forward flight.

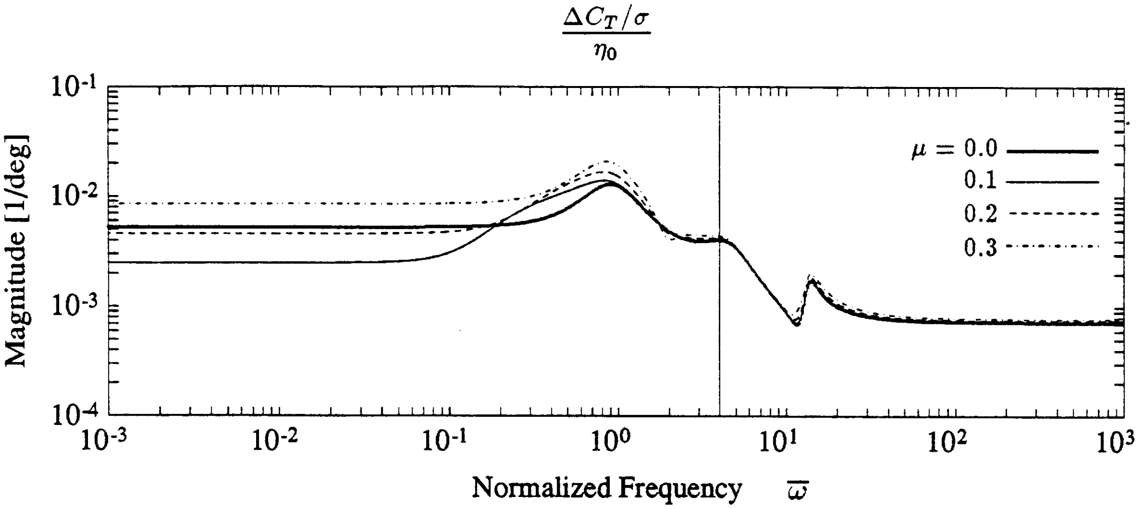

Figure 5-5: The effect of advance ratio on thrust response due to collective servoflap actuation for the H-34 rotor in edgewise forward flight.

Advance	Static Response 0/rev		HHC Response 4/rev	
Ratio	Loading	Thrust	Loading	Thrust
μ	$\lvert\Delta C_T/\sigma\rvert$ $\left[\frac{1}{\text{deg}}\right]$	$\lvert\Delta T\rvert$ $\left[\frac{\text{g}}{\text{deg}}\right]$	$\lvert\Delta C_T/\sigma\rvert$ $\left[\frac{1}{\text{deg}}\right]$	$\lvert\Delta T\rvert$ $\left[\frac{\text{g}}{\text{deg}}\right]$
0.00	0.0053	0.065	0.0041	0.051
0.05	0.0041	0.050	0.0041	0.051
0.10	0.0025	0.031	0.0041	0.051
0.15	0.0031	0.038	0.0041	0.051
0.20	0.0046	0.057	0.0042	0.052
0.25	0.0064	0.080	0.0043	0.053
0.30	0.0085	0.105	0.0044	0.054

Table 5.10: The effect of advance ratio on thrust response due to collective servoflap actuation for the H-34 rotor in edgewise forward flight.

Note that the thrust response at 4/rev increases slightly with advance ratio, while the steady response may vary significantly.

The phase for the rotor thrust responses $(\Delta C_T/\sigma)/\theta_{\mathrm{r},0}$, and $(\Delta C_T/\sigma)/\eta_0$ is fairly insensitive to advance ratio, and therefore was not plotted. The magnitudes for both the $(\Delta C_T/\sigma)/\theta_{\mathrm{r},0}$ and $(\Delta C_T/\sigma)/\eta_0$ responses increase at the 1/rev frequency. This is expected since collective and cyclic airloads and blade motions are coupled in forward flight.

In this chapter the state space model has been validated using the C-60 aeroelastic rotor analysis program obtained from Boeing Helicopters. The state space model has been exercised for the H-34 research rotor, and parametric analyses have been performed for various blade stiffnesses, servoflap sizes and locations, and advance ratios. Results from the state space model show that servoflap actuation can provide thrust amplitudes that are in the range necessary for higher harmonic vibration control.

Chapter 6

Conclusions

6.1 Review of the State Space Model Results

The state space model has been validated for a generic rotor model by comparing blade responses and rotor thrust responses with the results of the C-60 aeroelastic rotor analysis program. The twist dynamics of the rotor blade were adequately represented by including only two torsion modes in the state space model. The responses matched well for independent verification of blade dynamics for twist and flapping motion. Although the blade dynamics are coupled by aerodynamic effects, there is no reason to doubt the validity of the model for coupled dynamics in forward flight.

The Pitt and Peters' inflow model was found to reduce the steady thrust response due to collective pitch by 30% for the H-34 rotor in hover, while a 70% reduction may be observed in forward flight. The steady thrust exhibits a minimum for an advance ratio of $\mu \approx 0.11$, due to the inflow dynamics. Although the inflow dynamics effect the thrust response only slightly at the blade passage frequency, dynamic inflow should be included in the state space model in order to get accurate steady thrust responses.

As expected, softening the rotor blade in torsion reduces the steady thrust due to collective pitch, while it increases the steady thrust due to servoflap actuation. The soft blade is more responsive to moments that twist the blade. The propeller moment tends to adversely twist the blade for collective pitch, while the servoflap favorably twists the blade in aileron reversal. A blade with the first torsion frequency near the blade passage frequency was found to give the best higher harmonic response for collective pitch actuation. Even though the blade pitch motion is well damped by aerodynamics, the proximity of the torsion resonance to the N/rev frequency can be beneficial. Improvements in servoflap higher harmonic control were also observed by softening the rotor blade; however, softening the blade below $\overline{\omega}_1 = 4.50$ was found to contribute very little to the thrust response at N/rev, and in some cases reduced the response.

The thrust response of the rotor increases with the size of the servoflap and its radial location. Inboard of the 50% span location the servoflap adds little to the thrust response of the rotor. A servoflap located from $\overline{r}_1 = 0.70$ to $\overline{r}_2 = 0.90$ should be adequate for higher harmonic rotor control; however, a servoflap located from $\overline{r}_1 = 0.50$ to $\overline{r}_2 = 0.90$ can increase the thrust response by as much as 50%. The exact servoflap size will depend on the particular rotor design.

A 20% servoflap located from $\overline{r}_1 = 0.70$ to $\overline{r}_2 = 0.90$, can provide adequate higher harmonic control authority for a rotor with moderately stiff blades ($\overline{\omega}_1 = 4.50$). A servoflap deflection of 4.9 deg can achieve 0.25 g of higher harmonic vibration control, while a collective pitch of 2.8 deg can achieve the same level. A maximum servoflap deflection of 10 deg may provide up to 0.51 g for HHC. The thrust response can be increased by increasing the span of the servoflap. Even with tip loss as high as 10%, servoflap higher harmonic control should be possible. Although servoflap actuation cannot provide enough steady thrust for collective control of the rotor with moderately stiff blades, it may be used to augment primary collective pitch. If the blades are softened to $\overline{\omega}_1 = 2.50$, collective control can be achieved with the servoflap.

The rotor thrust response was found to be fairly insensitive to advance ratio at the blade passage frequency (N/rev). The thrust response from collective pitch decreases by less than 10% at the 4/rev frequency, while the response due to servoflap input can actually increase by 6%. The steady thrust response, however, varies significantly with advance ratio and exhibits a minimum at $\mu \approx 0.11$, due to inflow dynamics. The steady thrust response due to collective pitch and servoflap actuation can vary by as much as 50% with advance ratio. Although this affects steady rotor thrust, it does not restrict servoflap actuation for higher harmonic control.

The results of the state space model indicate that servoflap deflections of 4.9 deg are required for higher harmonic control of the H-34 rotor. Spangler and Hall [66] have successfully demonstrated servoflap deflections on the order of 10 deg for a wind tunnel test article, and have shown through energy arguments that similar results should be achievable in the full scale. Given the results of Spangler and Hall, the state space model shows that piezoelectric servoflap actuation is potentially feasible for higher harmonic rotor control.

6.2 Recommendations for Future Research

The state space model derived in this thesis has been found to be a powerful tool in determining transfer functions from root pitch and servoflap inputs to hub loads. It can be used to predict hub loads for collective, cyclic, and multicyclic control for a variety of actuation methods. It is ideal for rotor design and for performing parametric analyses, because it provides continuous transfer functions, rather than responses at a few discrete frequencies. It might be used most effectively in conjunction with the C-60 aeroelastic rotor program. The state space model can provide a first cut design solution very quickly, with the detailed analysis of a particular design solved by the C-60 program.

The state space model can be enhanced in order to evaluate more complicated rotor designs. Presently, the model assumes that the blades have constant mass and inertia properties. This assumption simplifies the model, because the solutions to the blade structural dynamics are expressed in terms of natural modes rather than assumed modes. Since the natural modes are orthogonal functions, there is no coupling between the modes and the equations of motion simplify. Separate aerodynamic and structural blade integrals could be included, however, so that the blade can have lumped structural and aerodynamic properties rather than continuous ones. Root cutout and tip loss could be incorporated, as well as radially varying aerodynamic properties. The mode shapes and modal frequencies can be computed from a lumped mass model, and the aerodynamic and structural integrals can be integrated numerically using these mode shapes. The modes will be correlated, so that the modal dynamics couple, and the state space matrices are no longer be sparse, but the model derivation remains the same.

Other features may also be included. Bending modes, and additional torsion modes may be added. An independent aerodynamic center, elastic axis, and center of gravity can be specified, and a δ_3 pitch/flap coupling term could be included. Since the current model specifies the servoflap actuation in terms of the increment in lift and moment slope only, perhaps the actual dynamics of the flap mechanism and actuator can be included in the model as well. Work is underway at M.I.T. to enhance the state space model.

Although the servoflap deflections obtained by Spangler and Hall for the scaled test article should be achievable in the full scale, demonstration is required. Eventually, piezoelectric actuation should be demonstrated on a full scale test article to prove the concept, and to investigate the practical engineering implications of dealing with these advanced materials on such a large scale. Concurrent research is being performed at M.I.T. to further demonstrate this method on a scale model.

In summary, the state space model derived in this study has been validated using existing software, and has been shown to be a valuable tool for rotor design and parametric analyses. The state space model provides continuous transfer functions from control inputs to hub loads, and therefore presents more intuitive information than simulations employing the transfer matrix method. The results of the state space model indicate that servoflap deflections required for higher harmonic control are in the range of those provided by piezoelectric actuation.

Appendix A

Rotor Blade Integrals

A convenient notation is defined to express common rotor blade integrals that are required in Chapter 4. The section radial location is nondimensionalized by the rotor radius R, so that the flapping hinge offset is located at $\overline{r} = \overline{e}$, while the blade tip is at $\overline{r} = 1$. The servoflap spans $\overline{r} = \overline{r}_1$ to $\overline{r}_2$. The function $\xi_{\theta_k}(\overline{r})$ corresponds to the torsional mode shape of the kth mode. The function $\xi_\beta(\overline{r})$ corresponds to the flapping mode shape in general. In this investigation only rigid flapping was assumed, so that $\xi_\beta(\overline{r}) = (\overline{r} - \overline{e})$. The prime on $\xi'_\beta(\overline{r})$ indicates differential with respect to $\overline{r}$. The rotor blade integrals are as follows:

$$
\begin{aligned}
A^n &= \int_{\overline{r}_1}^{\overline{r}_2} \overline{r}^n d\overline{r} \\
B^n &= \int_{\overline{r}_1}^{\overline{r}_2} (\overline{r} - \overline{e})\overline{r}^n d\overline{r} \\
C_k^n &= \int_{\overline{r}_1}^{\overline{r}_2} \xi_{\theta_k}(\overline{r})\overline{r}^n d\overline{r} \\
D^n &= \int_{\overline{e}}^{1} \overline{r}^n d\overline{r} \\
E^n &= \int_{\overline{e}}^{1} \xi_\beta(\overline{r})\overline{r}^n d\overline{r} \\
F^n &= \int_{\overline{e}}^{1} \xi'_\beta(\overline{r})\overline{r}^n d\overline{r} \\
G_k^n &= \int_{\overline{e}}^{1} \xi_{\theta_k}(\overline{r})\overline{r}^n d\overline{r} \\
H_k^n &= \int_{\overline{e}}^{1} \xi_{\theta_k}^2(\overline{r})\overline{r}^n d\overline{r}
\end{aligned}
$$

$$
\begin{aligned}
J^n &= \int_{\overline{e}}^{1} (\overline{r} - \overline{e})\overline{r}^n d\overline{r} \\
K^n &= \int_{\overline{e}}^{1} (\overline{r} - \overline{e})\xi_\beta(\overline{r})\overline{r}^n d\overline{r} \\
L^n &= \int_{\overline{e}}^{1} (\overline{r} - \overline{e})\xi_\beta^{'}(\overline{r})\overline{r}^n d\overline{r} \\
M_k^n &= \int_{\overline{e}}^{1} (\overline{r} - \overline{e})\xi_{\theta_k}(\overline{r})\overline{r}^n d\overline{r}
\end{aligned}
$$

Appendix B

Matrices for Rotor Dynamics

The matrices that comprise the governing equations of motion of the helicopter rotor and the resultant forces of interest were derived in Chapter 4. The matrices governing the dynamics of a helicopter rotor were derived in Section 4.4. The aerodynamic matrices were derived in Section 4.5, and the hub reactions were derived in Section 4.6. The matrices are labelled here for convenience.

Blade Dynamics:

$$\Delta_1 = I_\beta^* \begin{bmatrix} \overline{\nu}_\beta^2 & & \\ & (\overline{\nu}_\beta^2 - 1) & \\ & & (\overline{\nu}_\beta^2 - 1) \end{bmatrix}, \quad \Delta_2 = I_\beta^* \begin{bmatrix} 0 & 0 & 0 \\ 0 & 0 & 2 \\ 0 & -2 & 0 \end{bmatrix}, \quad \Delta_3 = I_\beta^* \begin{bmatrix} 1 & & \\ & 1 & \\ & & 1 \end{bmatrix},$$

$$\Delta_{4k} = I_{\theta_k}^* \begin{bmatrix} \overline{\omega}_k^2 & & \\ & (\overline{\omega}_k^2 - 1) & \\ & & (\overline{\omega}_k^2 - 1) \end{bmatrix}, \quad \Delta_{5k} = I_{\theta_k}^* \begin{bmatrix} 0 & 0 & 0 \\ 0 & 0 & 2 \\ 0 & -2 & 0 \end{bmatrix}, \quad \Delta_{6k} = I_{\theta_k}^* \begin{bmatrix} 1 & & \\ & 1 & \\ & & 1 \end{bmatrix}.$$

Propeller Moment:

$$\Phi_{1k} = -I_\theta^* G_k^0 \begin{bmatrix} 1 & & \\ & 1 & \\ & & 1 \end{bmatrix}, \quad \Phi_{2k} = -I_\theta^* H_k^0 \begin{bmatrix} 1 & & \\ & 1 & \\ & & 1 \end{bmatrix}.$$

Root Pitch Actuation:

$$\Psi_{1k} = I_\theta^* G_k^0 \begin{bmatrix} 0 & & \\ & 1 & \\ & & 1 \end{bmatrix} , \quad \Psi_{2k} = I_\theta^* G_k^0 \begin{bmatrix} 0 & 0 & 0 \\ 0 & 0 & -2 \\ 0 & 2 & 0 \end{bmatrix} , \quad \Psi_{3k} = -I_\theta^* G_k^0 \begin{bmatrix} 1 & & \\ & 1 & \\ & & 1 \end{bmatrix} . \; .$$

Aerodynamic Forces:

$$\Lambda_1 = \gamma \begin{bmatrix} 0 & (\frac{1}{4}\mu K^0 - \frac{1}{4}\mu L^1) & 0 \\ (-\frac{1}{2}\mu L^1) & 0 & (-\frac{1}{2}K^1 - \frac{1}{8}\mu^2 L^0) \\ 0 & (\frac{1}{2}K^1 - \frac{1}{8}\mu^2 L^0) & 0 \end{bmatrix} ,$$

$$\Lambda_2 = \gamma \begin{bmatrix} (-\frac{1}{2}K^1) & 0 & (-\frac{1}{4}\mu K^0) \\ 0 & (-\frac{1}{2}K^1) & 0 \\ (-\frac{1}{2}\mu K^0) & 0 & (-\frac{1}{2}K^1) \end{bmatrix} ,$$

$$\Lambda_3 = \gamma \begin{bmatrix} (\frac{1}{4}\mu^2 J^0 + \frac{1}{2}J^2) & 0 & (\frac{1}{2}\mu J^1) \\ 0 & (\frac{1}{8}\mu^2 J^0 + \frac{1}{2}J^2) & 0 \\ (\mu J^1) & 0 & (\frac{3}{8}\mu^2 J^0 + \frac{1}{2}J^2) \end{bmatrix} ,$$

$$\Lambda_{4k} = \gamma \begin{bmatrix} (\frac{1}{4}\mu^2 M_k^0 + \frac{1}{2}M_k^2) & 0 & (\frac{1}{2}\mu M_k^1) \\ 0 & (\frac{1}{8}\mu^2 M_k^0 + \frac{1}{2}M_k^2) & 0 \\ (\mu M_k^1) & 0 & (\frac{3}{8}\mu^2 M_k^0 + \frac{1}{2}M_k^2) \end{bmatrix} ,$$

$$\Lambda_5 = \gamma \begin{bmatrix} (-\frac{1}{2}J^1) & 0 & (-\frac{1}{4}\mu J^1) \\ 0 & (-\frac{1}{2}J^2) & 0 \\ (-\frac{1}{2}\mu J^0) & 0 & (-\frac{1}{2}J^2) \end{bmatrix} ,$$

$$\Lambda_6 = \gamma \begin{bmatrix} (\frac{1}{4}\overline{n}\mu^2 B^0 + \frac{1}{2}\overline{n}B^2) & 0 & (\frac{1}{2}\overline{n}\mu B^1) \\ 0 & (\frac{1}{8}\overline{n}\mu^2 B^0 + \frac{1}{2}\overline{n}B^2) & 0 \\ (\overline{n}\mu B^1) & 0 & (\frac{3}{8}\overline{n}\mu^2 B^0 + \frac{1}{2}\overline{n}B^2) \end{bmatrix} ,$$

$$\Lambda_{7k} = \gamma \begin{bmatrix} 0 & (\frac{1}{32}\mu\overline{c}^2 H_k^0) & 0 \\ 0 & 0 & (-\frac{1}{16}\overline{c}^2 H_k^1) \\ 0 & (\frac{1}{16}\overline{c}^2 H_k^1) & 0 \end{bmatrix},$$

$$\Lambda_{8k} = \gamma \begin{bmatrix} (-\frac{1}{16}\overline{c}^2 H_k^1) & 0 & (-\frac{1}{32}\mu\overline{c}^2 H_k^0) \\ 0 & (-\frac{1}{16}\overline{c}^2 H_k^1) & 0 \\ (-\frac{1}{16}\mu\overline{c}^2 H_k^0) & 0 & (-\frac{1}{16}\overline{c}^2 H_k^1) \end{bmatrix},$$

$$\Lambda_{9k} = \gamma \begin{bmatrix} (\frac{1}{4}\overline{p}\mu^2\overline{c}C_k^0 + \frac{1}{2}\overline{pc}C_k^2) & 0 & (\frac{1}{2}\overline{p}\mu\overline{c}C_k^1) \\ 0 & (\frac{1}{8}\overline{p}\mu^2\overline{c}C_k^0 + \frac{1}{2}\overline{pc}C_k^2) & 0 \\ (\overline{p}\mu\overline{c}C_k^1) & 0 & (\frac{3}{8}\overline{p}\mu^2\overline{c}C_k^0 + \frac{1}{2}\overline{pc}C_k^2) \end{bmatrix}.$$

Hub Reactions:

$$\Gamma_1 = \sigma a \begin{bmatrix} 0 & (\frac{1}{4}\mu E^0 - \frac{1}{4}\mu F^1) & 0 \\ (\frac{1}{4}\overline{e}\mu F^1) & (-\frac{1}{2\gamma}\overline{\omega}_\beta^2 I_\beta^* - \frac{1}{2}\overline{e}\frac{J^0}{\gamma D^2}) & (\frac{1}{4}\overline{e}E^1 + \frac{1}{16}\overline{e}\mu^2 F^0 \\ 0 & (\frac{1}{4}\overline{e}E^1 - \frac{1}{16}\overline{e}\mu^2 F^0) & (\frac{1}{2\gamma}\overline{\omega}_\beta^2 I_\beta^* + \frac{1}{2}\overline{e}\frac{J^0}{\gamma D^2}) \end{bmatrix},$$

$$\Gamma_2 = \sigma a \begin{bmatrix} (-\frac{1}{2}E^1) & 0 & (-\frac{1}{4}\mu E^0) \\ 0 & (\frac{1}{4}\overline{e}E^1) & (\overline{e}\frac{J^0}{\gamma D^2}) \\ (-\frac{1}{4}\overline{e}\mu E^0) & (\overline{e}\frac{J^0}{\gamma D^2}) & (-\frac{1}{4}\overline{e}E^1) \end{bmatrix},$$

$$\Gamma_3 = \sigma a \begin{bmatrix} (-\frac{J^0}{\gamma D^2}) & 0 & 0 \\ 0 & (\frac{1}{2}\overline{e}\frac{J^0}{\gamma D^2}) & 0 \\ 0 & 0 & (-\frac{1}{2}\overline{e}\frac{J^0}{\gamma D^2}) \end{bmatrix},$$

$$\Gamma_4 = \sigma a \begin{bmatrix} (\frac{1}{4}\mu^2 D^0 + \frac{1}{2}D^2) & 0 & (\frac{1}{2}\mu D^1) \\ 0 & (-\frac{1}{16}\overline{e}\mu^2 D^0 - \frac{1}{4}\overline{e}D^2) & 0 \\ (\frac{1}{2}\overline{e}\mu D^1) & 0 & (\frac{3}{16}\overline{e}\mu^2 D^0 + \frac{1}{4}\overline{e}D^2) \end{bmatrix},$$

$$\Gamma_{5k} = \sigma a \begin{bmatrix} (\frac{1}{4}\mu^2 G_k^0 + \frac{1}{2}G_k^2) & 0 & (\frac{1}{2}\mu G_k^1) \\ 0 & (-\frac{1}{16}\overline{e}\mu^2 G_k^0 - \frac{1}{4}\overline{e}G_k^2) & 0 \\ (\frac{1}{2}\overline{e}\mu G_k^1) & 0 & (\frac{3}{16}\overline{e}\mu^2 G_k^0 + \frac{1}{4}\overline{e}G_k^2) \end{bmatrix},$$

$$\Gamma_6 = \sigma a \begin{bmatrix} (-\frac{1}{2}D^1) & 0 & (-\frac{1}{4}\mu D^1) \\ 0 & (\frac{1}{4}\overline{e}D^2) & 0 \\ (-\frac{1}{4}\overline{e}\mu D^0) & 0 & (-\frac{1}{4}\overline{e}D^2) \end{bmatrix},$$

$$\Gamma_7 = \sigma a \begin{bmatrix} (\frac{1}{4}\overline{n}\mu^2 A^0 + \frac{1}{2}\overline{n}A^2) & 0 & (\frac{1}{2}\overline{n}\mu A^1) \\ 0 & (-\frac{1}{16}\overline{en}\mu^2 A^0 - \frac{1}{4}\overline{en}A^2) & 0 \\ (\frac{1}{2}\overline{en}\mu A^1) & 0 & (\frac{3}{16}\overline{en}\mu^2 A^0 + \frac{1}{4}\overline{en}A^2) \end{bmatrix}.$$

References

[1] Abramson, J., and Rogers, E.O., "Optimization Theory Applied to Higher Harmonic Control of Circulation Controlled Rotors," 37th Annual Forum of the American Helicopter Society, New Orleans, LA, 1981.

[2] Amer, K.B., and Neff, J.R., "Vertical-Plane Pendulum Absorbers for Minimizing Helicopter Vibratory Loads," AHS/NASA-Ames Specialists' Meeting on Rotorcraft Dynamics, NASA SP-352, February 1974.

[3] Anderson, E.H., and Crawley, E.F., "Piezoceramic Actuation of One- and Two-Dimensional Structures," Massachusetts Institute of Technology Space Systems Laboratory Report SSL #5-89, Cambridge, MA, May 1989.

[4] Barrett, R., "Intelligent Rotor Blade Actuation through Directionally Attached Piezoelectric Crystals," 46th Annual Forum of the American Helicopter Society, Washington D.C., 1990.

[5] Bielawa, R.L., "Analytical Investigation of Helicopter Rotor Blade Appended Aeroelastic Devices," United Technologies NASA CR 166525, February 1984.

[6] Blisplinghoff, R.L., Ashley, H., and Halfman, R.L. *Aeroelasticity,* Addison-Wesley, Cambridge, MA, 1955.

[7] Braun D., "Development of Anti-Resonance Force Isolators for Helicopter Vibration Reduction," 6th European Rotorcraft and powered Lift Aircraft Forum, Bristol, Paper No. 18, 1980.

[8] Braun D., "Ground and Flight Tests of a Passive Rotor Isolation System for Helicopter Vibration Reduction," *Vertica*, Vol 8, No. 1, pp. 1–14, 1984.

[9] Carpenter, P.J., and Paulnock, S., *Hovering and Low-Speed Performance and Control Characteristics of an Aerodynamic-Servocontrolled Helicopter Rotor System as Determined on the Langley Helicopter Tower,* NACA TN-2086, May 1950.

[10] Crawley, E.F., and Lazarus, K.B., "Induced Strain Actuation of Isotropic and Anisotropic Plates," 30th Structures, Structural Dynamics and Materials Conference, Mobile, Alabama, April 1989.

[11] Cross, L.E., "Electrostrictive Behavior of Lead Magnesium Niobate-based Dielectrics," *Ferroelectrics,* Vol. 27, 1980.

[12] Desjardins, R.A., and Sankewitsch, V., "Integrated Floor/Fuel Isolation System for the Model 234 Commercial Chinook," 5th European Rotorcraft and Powered Lift Aircraft Forum, Amsterdam, Paper No. 39, 1979.

[13] Drela, M., "XFOIL: An Analysis and Design System for Low Reynolds Number Airfoils," in *Low Reynolds Number Aerodynamics,* Springer-Verlag Lecture Notes in Engineering, No. 54, 1989.

[14] DuVal, R.W., Gregory, C.Z., and Gupta, N.K., "Design and Evaluation of a State-Feedback Vibration Controller," *Journal of the American Helicopter Society,* Vol. 29, No. 3, pg. 30, 1984.

[15] Fay, J., *The Helicopter (History, Piloting and How It Flies),* Hippocrene Books, New York, NY, 1987.

[16] Flannelly, W.G., "The Dynamic Anti-Resonant Vibration Isolator," 22nd Annual Forum of the American Helicopter Society, Washington D.C., pp. 152–160, 1966.

[17] Anonymous, "Flying Qualities of Piloted V/STOL Aircraft," U.S. Military Specification MIL-F-83300.

[18] Gabel, R., and Reichert, G., "Pendulum Absorbers Reduce Transition Vibration," 31st Annual Forum of the American Helicopter Society, Washington D.C., 1975.

[19] Anonymous, "Guide for the Evaluation of Human Exposure to Whole-Body Vibration," International Standards Organization ISO-2631.

[20] Gupta, B.P., Logan, A.H., and Wood, E.R., "Higher Harmonic Control for Rotary Wing Aircraft," AIAA/AHS/ASEE Aircraft Design Systems and Operations Meeting, San Diego, CA, 1984.

[21] Gupta, B.P., Wood, E.R., "Low Vibration Design of AAH for Mission Proficiency Requirements," American Helicopter Society National Specialists' Meeting on Helicopter Vibration, Nov 2–4, 1981.

[22] Gupta, N.K., "Frequency-Shaped Cost Functionals: Extension of Linear-Quadratic-Gaussian Design Methods," *Journal of Guidance and Control,* Vol. 3, No. 6, pg. 529, December 1980.

[23] Gupta, N.K., and DuVal, R.W., "A New Approach for Active Control of Rotorcraft Vibration," *Journal of Guidance and Control,* Vol. 5, No. 2, pg. 143, April 1982.

[24] Hall, S.R., and Wereley, N.M., "Linear Control Issues in the Higher Harmonic Control of Helicopter Vibrations," 45th Annual Forum of the American Helicopter Society, Boston, MA, May 1989.

[25] Halwes, D.R., "LIVE-Liquid Inertia Vibration Eliminator," 36th Annual Forum of the American Helicopter Society, Paper No. 80-22, 1980.

[26] Ham, N.D., "Helicopter Individual-Blade-Control and its Applications," 39th Annual Forum of the American Helicopter Society, pg. 613, 1983.

[27] Ham, N.D., "Helicopter Individual-Blade-Control Research at MIT 1977–1985," *Vertica*, Vol. 11, pg. 109, 1987.

[28] Hammond, C.E., Hollenbaugh, D.D., Clevenson, S.A., and Leatherwood, J.D., "An Evaluation of Helicopter Noise and Vibration Ride Quality Criteria," American Helicopter Society National Specialists' Meeting on Helicopter Vibration, Nov 2–4, 1981.

[29] Hardenberg, P.W., and Niebanck, C., "Helicopter Airframe Variable Tune Vibration Absorber," AIAA/AHS Systems, Design and Operations Conference, San Diego, CA, Oct. 31–Nov. 2, 1984.

[30] Anonymous, "Helicopter Flying and Ground Handling Qualities: General Requirements For," U.S. Military Specification MIL-H-8501A.

[31] Hooper, W.E., "The Vibratory Airloading of Helicopter Rotors," Ninth European Rotorcraft and Powered Lift Aircraft Forum, Stresa, Italy, 1983.

[32] Anonymous, "Human Engineering Design Criteria for Military Systmes, Equipment and Facilities," U.S. Military Standard MIL-STD-1472D.

[33] Jang, J., and Chopra, I., "Ground and Air Resonance of an Advanced Bearingless Rotor in Hover," AIAA Dynamics Specialist Conference, Monterey, CA, April 1987.

[34] Johnson, W., *Helicopter Theory,* Princeton University Press, Princeton, NJ, 1980.

[35] Kirkpatrick, D.G., and Barnes, D.R., "Development and Evolution of the Circulation Control Rotor," 36th Annual Forum of the American Helicopter Society, 1980.

[36] Lazarus, K.B., *Multivariable High-Authority Control of Plate-like Active Lifting Surfaces,* Doctoral Thesis, Department of Aeronautics and Astronautics, Massachusetts Institute of Technology, Cambridge, MA, June 1992.

[37] Lehmann, G., "The Effect of Higher Harmonic Control (HHC) On a Four-Bladed Hingeless Model Rotor," Tenth European Rotorcraft Forum, Hague, The Netherlands, 1984.

[38] Lemnios, A.Z., and Dunn, F.K., "Theoretical Study of a Multicyclic Control of a Controllable Twist Rotor," U.S. Army Air Mobility Research and Development Laboratory, Moffett Field, CA, Kaman NASA CR-151959, 1978.

[39] Lins, W.F., "Human Vibration Response Measurement," U.S. Army Tank Automotive Command Technical Report No. 11511, June 1972.

[40] Loewy, R.G., "Helicopter Vibrations: A Technological Perspective," *Journal of the American Helicopter Society,* Vol. 29, No. 4, 1984.

[41] Maciejowski, J.M., *Multivariable Feedback Design,* Addison-Wesley, New York, NY, 1989.

[42] Anonymous, MATLAB *User's Guide,* The MathWorks, Natick, MA, January 1991.

[43] McCloud, J.L. III, "The Promise of Multicyclic Control," *Vertica,* Vol. 4, No. 1, 1980.

[44] McCloud III, J.L., and Kretz, M., "Multicyclic Jet-Flap Control for Alleviation of Helicopter Blade Stresses and Fuselage Vibration," AHS/NASA-Ames Specialists' Meeting on Rotorcraft Dynamics, NASA SP-352, February 1974.

[45] McCloud, J.L. III, and Weisbirch, A.L., "Wind-Tunnel Results of a Full-Scale Multicyclic Controllable Twist Rotor," 34th Annual Forum of the American Helicopter Society, 1978.

[46] Meirovitch, L., *Analytical Methods in Vibrations,* Macmillan, New York, NY, 1967.

[47] Miao, W., Kottapalli, S.B.R., and Frye, H.M., "Flight Demonstation of Higher Harmonic Control (HHC) on the S-76," 42nd Annual Forum of the American Helicopter Society, Washington D.C., 1986.

[48] Molusis, J.A., Hammond, C.E., and Cline, J.H., "A Unified Approach to the Optimal Design of Adaptive and Gain Scheduled Controllers to Achieve Minimum

Helicopter Rotor Vibration," 37th Annual Forum of the American Helicopter Society, New Orleans, LA, 1981.

[49] Nygren, K.P., Schrage, D.P., "Fixed-Gain Versus Adaptive Higher Harmonic Control Simulation," *Journal of the American Helicopter Society*, Vol. 34, No. 3, pp. 51–58, 1989.

[50] Paul, W.F., "Development and Evaluation of the Main Rotor Bifilar Absorber," 25th Annual Forum of the American Helicopter Society, Washington D.C., 1969.

[51] Payne, P.R., "Dynamics of a Rotor Controlled by Aerodynamic Servo Flaps," *Aircraft Engineering,* Vol. 31, pp. 330–339, 1959.

[52] Peters, D.A., "Hingeless Rotor Frequency Response with Unsteady Inflow," AHS/NASA-Ames Specialists' Meeting on Rotorcraft Dynamics, NASA SP-352, February 1974.

[53] Pitt, D.M., Peters, D.A., "Theoretical Prediction of Dynamic-Inflow Derivatives," *Vertica*, Vol. 5, pg. 21, 1981.

[54] Piziali, R.A., and Trenka, A.R., "A Theoretical Study of the Application of Jet-Flap Circulation Control for Reduction of Vibratory Forces," Kaman NASA CR-137515, 1974.

[55] Polychroniadis, M., and Achache, M., "Higher Harmonic Control: Flight Tests of an Experimental System On SA-349 Research Gazelle," 42nd Annual Forum of the American Helicopter Society, Washington D.C., 1986.

[56] Reader, K.R., Dixon, W.J. Jr., "Evaluation of a Ten-Foot Diameter X-Wing Rotor," 40th Annual Forum of the American Helicopter Society, Arlington, VA, 1984.

[57] Reichert, G., "Helicopter Vibration Control: A Survey," *Vertica,* Vol. 5, No. 1, 1981.

[58] Rita, A.D., McGarvey, J.H., Jones, R., "Helicopter Rotor Isolation Evaluation Utilizing the Dynamic Antiresonant Vibration Isolator," 32nd Annual Forum of the American Helicopter Society, Paper No. 1030, 1976.

[59] Robinson, D.W., Nettles, W.E., Howes, H.E., "Design Variables for a Controllable Twist Rotor," 31st Annual Forum of the American Helicopter Society, May 1975.

[60] Sarigul-Klijn, M.M., Kolar, R., Wood, E.R., and Straub, F.K., "On Chaos Methods Applied to Higher Harmonic Control," Proceedings of the 46th Annual Forum of the American Helicopter Society, Washington D.C., 1990.

[61] Schrage, D.P., and Peskar, R.E., "Helicopter Vibration Requirements," 33rd Annual Forum of the American Helicopter Society, 1977.

[62] Shaw, J., *A Feasibility Study of Helicopter Vibration Reduction by Self-Optimizing Higher Harmonic Blade Pitch Control,* Master's Thesis, Department of Aeronautics and Astronautics, Massachusetts Institute of Technoloby, Cambridge, MA, 1967.

[63] Shaw, J., Albion, N., Hanker, E.J., and Teal, R.S., "Higher Harmonic Control: Wind Tunnel Demonstration of Fully Effective Vibratory Hub Force Suppression," 41st Annual Forum of the American Helicopter Society, Fort Worth, TX, 1985.

[64] Shipman, D.P., White, J.A., and Cronkhite, J.D., "Fuselage Nodalization," 28th Annual Forum of the American Helicopter Society, Paper No. 611, 1972.

[65] Spangler, R.L., and Hall, S.R., "Piezoelectric Actuators for Helicopter Rotor Control," Massachusetts Institute of Technology Space Systems Laboratory Report SSL #1-89, Cambridge, MA, January 1989.

[66] Spangler, R.L., and Hall, S.R., "Piezoelectric Actuators for Helicopter Rotor Control," 31st Structures, Structural Dynamics and Materials Conference, Long Beach, CA, April 1990.

[67] Taylor, R.B., and Teare, P.A., "Helicopter Vibration Reduction with Pendulum Absorbers," 30th Annual Forum of the American Helicopter Society, May 1974.

[68] Uchino, K., "Electrostrictive Actuators: Materials and Applications," *American Ceramic Society Bulletin,* Vol. 65, No. 4, April 1986.

[69] Walsh, D.M. "Flight Tests of an Open Loop Higher Harmonic Control System on an S-76A Helicopter," 42nd Annual Forum and of the American Helicopter Society, Washington D.C., 1986.

[70] Wei, F., and Weisbirch, A.L., "Multicyclic Controllable Twist Rotor Data Analysis," Kaman NASA CR-152251, 1979.

[71] Welsh, W.A., and Blackwell, R.H. Jr., "Higher Harmonic and Trim Control of the X-Wing Circulation Control Wind Tunnel Model Rotor," 45th Annual Forum of the American Helicopter Society, Boston, MA, 1989.

[72] Wheatley, J.B., "An Aerodynamic Analysis of the Autogiro Rotor with a Comparison between Calculated and Experimental Results," NACA Report 487, 1934.

[73] Wilkerson, J.B., Reader, K.R., and Linck, D.W., "The Application of Circulation Control Aerodynamics to a Helicopter Rotor Model," 29th Annual Forum of the American Helicopter Society, 1973.

[74] Wilson, W.F. moderator, "Control of 1/Rev Vibration," AHS/NASA-Ames Specialists Meeting on Rotorcraft Dynamics, Session V: Application of Dynamics Technology To Helicopter Design, NASA SP-352, February 1974.

[75] Wood, E.R., Powers, R.W., Cline, J.H., and Hammond, C.E., "On Developing and Flight Testing a Higher Harmonic Control System," 39th Annual Forum of the American Helicopter Society, St. Louis, MO, 1983.

[76] Anonymous, "X-Wing Full Scale Wind Tunnel Test Final Report," Lockheed Report SP-5190, October 1980.